



**Politecnico
di Torino**

Politecnico di Torino

Corso di Laurea Magistrale in Ingegneria Meccatronica

A.a. 2020/2021

Sessione di Laurea ottobre 2021

Field-oriented current control for a permanent-magnet brushless motor used in regenerative shock absorbers

Relatore:

Prof. Nicola Amati

Correlatori:

Prof. Renato Galluzzi

Dr. Salvatore Circosta

Candidato:

Bruno Lavè

ABSTRACT

In the recent years, mechatronic devices with energy harvesting features are becoming key elements in the automotive industry. These technologies lead to emission reduction, comfort and handling improvements. The aim is to push the related industry towards the electrification of powertrain and chassis, making it, as far as possible, environmentally friendly. The present work focuses its attention on regenerative shock absorbers: systems able to set damping or active forces to the vehicle suspension, allowing the efficient management of comfort-handling trade-offs, while also enabling energy recovery from road irregularities. The addressed regenerative dampers arise from a long-term project, whose goal is to provide the design of a regenerative damper for automotive suspensions. The contribution of this thesis aims at the development of the motor control system and the ECU programming. The project implements a standard field-oriented control algorithm (FOC) with quadrature current control. Starting from this basis, many features and refinements have been added: the central aspects are the introduction of the flux weakening control, the regenerative phase management and the implementation on a Texas Instruments development kit. The method utilized to achieve the goals follows a V-shaped development flow. The work started from the analysis of the requirements and functional specification of the system and its power components. Successively, a high-level and low-level design of the algorithm have been done in the MATLAB/Simulink environment: this phase dealt with accurate modelling of every stage of the motor control and numerical validation through simulation. Then, the study evolved into the integration and prototype testing of the power stage on a test bench. During the experimental campaign the power electronic components have been set to work properly. A benchmarking analysis of the possible battery pack solutions has been done, while the 3-phase inverter and the connected DSP have been tested under several working conditions to validate them and their robustness. Finally, the functionality of the motor control system design has been verified, by investigating different operating points of the electric machine.

Contents

List of figures	3
List of tables	8
Symbols	9
1. Introduction	13
1.1. Automotive suspension systems	13
1.2. Rotary regenerative dampers for automotive suspensions	16
1.2.1. <i>Hydraulic shock absorber</i>	17
1.2.2. <i>Electro-mechanical shock absorber</i>	19
1.2.3. <i>Power stage and control</i>	21
1.3. Thesis overview	22
1.3.1. <i>Experimental method</i>	23
1.3.2. <i>Control strategy</i>	24
1.3.3. <i>Thesis outline</i>	25
2. Current control method	26
2.1. (Sensored) field-oriented control of 3-phase PMSM	26
2.1.1. <i>MTPA-Maximum torque per ampere</i>	28
2.1.2. <i>MTPV-Flux weakening control</i>	36
2.2. Space vector modulation	42
2.2.1. <i>Vectorial analysis of the 3-phase inverter</i>	43
2.2.2. <i>Pulse-width modulation</i>	45
2.3. Rotor flux position	49
2.3.1. <i>Sensorless estimators</i>	49
2.3.2. <i>Analog Hall sensor</i>	51
3. Design and simulation	54
3.1. Control algorithm overview	54
3.2. RRSA and EHA	56
3.2.1. <i>Functional specifications</i>	56

3.2.2.	<i>Control algorithm design</i>	57
3.2.3.	<i>Simulation</i>	63
3.3.	Flux map based motor model	72
3.3.1.	<i>Calibration settings calculation</i>	73
3.3.2.	<i>Test</i>	76
4.	Experimental campaign	79
4.1.	Power stage	79
4.1.1.	<i>3-phase inverter</i>	79
4.1.2.	<i>Battery pack</i>	99
4.2.	ECU programming	101
4.2.1.	<i>Texas instruments development kit</i>	102
4.2.2.	<i>Implementation</i>	103
4.3.	Results	112
4.3.1.	<i>Open-loop</i>	112
4.3.2.	<i>Flux observer</i>	116
4.3.3.	<i>Sliding mode observer</i>	123
4.3.4.	<i>Hall sensor</i>	126
Conclusion	131
A	Numerical models	134
A.1.	Clarke and Park transforms	134
A.2.	Dynamic modelling of AC synchronous machines	137
Bibliography	139
Acknowledgments	141

List of figures

Figure 1. 1: Active suspension control algorithm	14
Figure 1. 2: Force-speed maps of the regenerative shock absorber	16
Figure 1. 3: Layout of a hydraulic regenerative shock absorber.....	17
Figure 1. 4: Electro-hydrostatic motor prototype	18
Figure 1. 5: Linkage solution (thick solid lines)	19
Figure 1. 6: Rotary regenerative damper working principle diagram.....	19
Figure 1. 7: Rotary regenerative motor prototype	20
Figure 1. 8: Block diagram of the control strategy	22
Figure 1. 9: V-shaped development flow	23
Figure 1. 10: Motor control strategy	24
Figure 2. 1: 3-Phase synchronous motor with one PM pair pole rotor.....	26
Figure 2. 2: Interaction between the rotating stator flux and the rotor flux	28
Figure 2. 1: 3-Phase synchronous motor with one PM pair pole rotor.....	26
Figure 2. 2: Interaction between the rotating stator flux and the rotor flux	28
Figure 2. 3: Basic FOC control scheme for AC motor	29
Figure 2. 4: Current, voltage and rotor flux space vectors in (a,b,c), (α,β), and (d,q) frames	31
Figure 2. 5: Torque control schematic.....	31
Figure 2. 6: Mechanical characteristic of the torque.....	33
Figure 2. 7: CVC scheme	34
Figure 2. 8: CVC transfer functions.....	35
Figure 2. 9: CVC Bode diagram	35
Figure 2. 10: Torque-speed characteristic.....	37
Figure 2. 11: Field-weakening characteristics	38
Figure 2. 12: FWC first case	40
Figure 2. 13: FWC second case	40
Figure 2. 14: FWC third case.....	41
Figure 2. 15: Flux-weakening controller	42
Figure 2. 16: Space vector modulation workflow	42
Figure 2. 17: Equivalence between the 3-ph system and vectorial representation.....	43
Figure 2. 18: Output voltage waveforms and state switching functions	44
Figure 2. 19: Voltage vectors of a 3-phase inverter.....	45
Figure 2. 20: Reference function for SVM.....	46
Figure 2. 21: SVM duty cycles with $m=1$	47

Figure 2. 22: SVM duty cycles with $m=1.15$	47
Figure 2. 23: SVM limit.....	48
Figure 2. 24: SVM third harmonic influence	48
Figure 2. 25: SMO attraction function	50
Figure 2. 26: Hall sensor output characteristic	52
Figure 3. 1: Control algorithm overview	55
Figure 3. 2: SPM motor radial view	56
Figure 3. 3: MTPA control reference	58
Figure 3. 4: Sensorless estimators	58
Figure 3. 5: DC component removal.....	59
Figure 3. 6: Phase current feedback.....	59
Figure 3. 7: Current controller block scheme	60
Figure 3. 8: Flux-weakening controller.....	60
Figure 3. 9: Current limitation.....	61
Figure 3. 10: PI current regulator.....	61
Figure 3. 11: Bode diagram.....	62
Figure 3. 12: Step response.....	62
Figure 3. 13: Voltage saturation	63
Figure 3. 14: Space vector modulation	63
Figure 3. 15: Duty cycles conversion.....	63
Figure 3. 16: 3-phase inverter.....	64
Figure 3. 17: Motor model.....	64
Figure 3. 18: Algorithm processing delays	65
Figure 3. 19: Test 1, torque-speed-position	66
Figure 3. 20: Test 1, current space vector	66
Figure 3. 21: Rotor mechanical and electrical angle	67
Figure 3. 22: Test 1, voltages and currents.....	67
Figure 3. 23: Test 1, voltage and current highlight.....	68
Figure 3. 24: Test 1, current step response	68
Figure 3. 25: Test 1, FWC.....	68
Figure 3. 26: Test 1, duty cycles	69
Figure 3. 27: Test 1, duty cycles highlight	69
Figure 3. 28: Test 2, torque-speed-position	70
Figure 3. 29: Test 2, current space vector	70
Figure 3. 30: Test 3, torque-speed-position	71
Figure 3. 31: Test 3, voltages and currents.....	71

Figure 3. 32: SMO test, torque-speed-position.....	72
Figure 3. 33: d-axis flux map	73
Figure 3. 34: q-axis flux map	73
Figure 3. 35: Torque-current characteristic.....	74
Figure 3. 36: Flux map based motor model.....	76
Figure 3. 37: Test flux, current space vector.....	76
Figure 3. 38: Test flux, torque-speed-position.....	77
Figure 3. 39: Test flux, voltages and currents	77
Figure 4. 1: Inverter block diagram.....	80
Figure 4. 2: DRV8353RS-first side	80
Figure 4. 3: DRV8353RS-second side	81
Figure 4. 4: Single supply configuration	82
Figure 4. 5: Dual supply configuration	82
Figure 4. 6: SPI	84
Figure 4. 7: SPI input data	84
Figure 4. 8: SPI output data.....	84
Figure 4. 9: SPI slave timing diagram	84
Figure 4. 10: TDRIVE state machine.....	86
Figure 4. 11: DRV8353RS switching.....	86
Figure 4. 12: Current-shunt amplifier.....	87
Figure 4. 13: DRV8353RS thermal test bench.....	88
Figure 4. 14: LDO thermal test.....	88
Figure 4. 15: DRV8353RS thermal test, 15 A _{DC}	89
Figure 4. 16: DRV8353RS thermal test, 15 A _{DC}	90
Figure 4. 17: DRV8353RS thermal test, 15 A _{DC}	91
Figure 4. 18: DRV8353RS thermal test, 15 A _{DC} dynamics	92
Figure 4. 19: DRV8353RS thermal test, 30 A 50% duty-cycles	93
Figure 4. 20: DRV8353RS, modified version	94
Figure 4. 21: DRV8323RS overview.....	95
Figure 4. 22: DRV8323RS thermal test, 15 A _{DC}	96
Figure 4. 23: DRV8323RS thermal test, 30 A 50% duty-cycles	97
Figure 4. 24: DRV8323RS, shunt resistor change	97
Figure 4. 25: DRV8323RS, heat sinks	98
Figure 4. 26: Lithium iron-phosphate battery.....	99
Figure 4. 27: Battery structure	100
Figure 4. 28: Battery data	101

Figure 4. 29: TI development kit.....	102
Figure 4. 30: Launchpad overview	102
Figure 4. 31: Test bench.....	104
Figure 4. 32: Power supply	104
Figure 4. 33: Launchpad connections.....	105
Figure 4. 34: Host-target communication	105
Figure 4. 35: Speed loop	107
Figure 4. 36: Position generator	107
Figure 4. 37: Speed measurement	108
Figure 4. 38: Hall sensor logic	108
Figure 4. 39: Current measurement	109
Figure 4. 40: Duty-cycles scaling.....	110
Figure 4. 41: PWM interface blocks.....	110
Figure 4. 42: Task scheduling	111
Figure 4. 43: Host model	112
Figure 4. 44: Open-loop test.....	113
Figure 4. 45: Open-loop test, zoom.....	113
Figure 4. 46: Open-loop test, current reference step	114
Figure 4. 47: Open-loop test, current reference step negative to positive	115
Figure 4. 48: Open-loop test, electrical variables.....	115
Figure 4. 49: Flux observer test.....	116
Figure 4. 50: Flux observer test, zoom	117
Figure 4. 51: Flux observer test, speed step change	118
Figure 4. 52: Flux observer test, electrical variables	119
Figure 4. 53: Flux observer test, FWC positive change	120
Figure 4. 54: Flux observer test, FWC negative change.....	121
Figure 4. 55: Flux observer test, FWC negative to positive change.....	122
Figure 4. 56: SMO test	123
Figure 4. 57: SMO test, zoom	124
Figure 4. 58: SMO test, FWC positive change.....	125
Figure 4. 59: SMO test, FWC negative change.....	126
Figure 4. 60: Hall sensor test	128
Figure 4. 61: Hall sensor test, FWC positive change.....	129
Figure 4. 62: SMO test, FWC negative to positive change.....	130
Figure A. 1: Stator current space vector	134
Figure A. 2: Stator current space vector in the stationary frame	134

Figure A. 3: Time-response of the individual (a,b,c) and (α,β) components	135
Figure A. 4: Stator current space vector in the (α,β) and (d,q) frames	136
Figure A. 5: Time-response of the individual (d,q) and (α,β) components.....	136
Figure A. 6: SPM motor construction	137

List of tables

Table 3. 1: Electric machine parameters..... 56

Table 3. 2: Flux maps machine parameters..... 75

Table 3. 3: Flux maps control calibration..... 75

Table 4. 1: DRV8353RS thermal test, 15 A_{DC} 92

Table 4. 2: Battery pack solutions 100

Table 4. 3: FWC calibration..... 109

Symbols

CO ₂	Carbon dioxide
NVH	Noise, vibration, harshness
PM	Permanent-magnet
DC	Direct current
MOSFET	Metal-oxide-semiconductor field-effect transistor
PI	Proportional-integral compensator
ECU	Electronic control unit
AC	Alternate current
FOC	Field-oriented control
PMSM	Permanent magnet synchronous motor
MTPA	Maximum torque per ampere
DSP	Digital signal processing
BEMF	Back-electromotive force
EMI	Electromagnetic interference
SPM	Surface permanent magnet
MMF	Magneto-motive force
PWM	Pulse-width modulation
T	Electromagnetic torque
p	Pole pairs
λ	Stator phase flux linkage
i	Stator phase current
v	Stator phase voltage
R_s	Stator phase resistance
ω	Electrical angular speed
L_s	Synchronous inductance
λ_m	Permanent magnet flux linkage
δ	Load angle
CVC	Current vector control
T_s	Sampling time
k_p	Proportional gain
k_i	Integral gain
ω_c	Current control bandwidth

f_s	Sampling frequency
v_{max}	Inverter maximum voltage
v_{dc}	DC-link voltage
FWC	Flux-weakening control
IPM	Internal permanent magnet
i_{max}	Inverter maximum current
ω_b	Base speed
I_o	Machine characteristic current
MTPV	Maximum torque per voltage
SVM	Space vector modulation
θ	Rotor flux position
SMO	Sliding mode observer
ANF	Adaptive notch filter
PLL	Phase-locked loop
EHA	Electro-hydrostatic shock absorber
RRSA	Rotary regenerative shock absorber
k_t	Machine torque constant
ω_{max}	Maximum machine speed
IIR	Infinite impulse response
k_{pfw}	FWC proportional gain
k_{ifw}	FWC integral gain
TI	Texas Instruments
DRV	Driver
SGD	Smart gate driver
SPI	Serial peripheral interface
LDO	Low-dropout regulator
SDI	SPI input data
SDO	SPI output data
v_{ds}	Drain-source voltage
USB	Universal serial bus
ADC	Analog to digital converter
SOC	State of charge
LiFePO ₄	Lithium iron-phosphate
BMS	Battery management system
CAN	Controller area network

LED	Light emitting diode
GPIO	General purpose input/output
ISR	Interrupt service routine
CPU	Central processing unit

1. Introduction

Vehicle pollutant emissions have been the focus of attention in recent years and regulations are becoming more strict with the new aim for a cleaner environment. The constant need to make the automotive sector environmentally friendly, as far as possible, is pushing the related industry towards the electrification of the powertrain and chassis. In this context, mechatronic devices with energy harvesting characteristics are fundamental due to their improved efficiency and small CO₂ footprint [1]. Regenerative shock absorbers are an example of energy harvester systems, enabling the energy recovery from road irregularities. They are able to set damping or active forces to the vehicle suspension by means of an electric machine, controlled as a motor (actuator) or as a generator (damper) and in this latter case they can recover part of the energy otherwise dissipated as heat. This type of solution presents benefits in terms of fuel saved, road holding, ride comfort and pollutant emission reduction.

1.1. Automotive suspension systems

Suspension's systems are integrated in the vehicles to filter the vibrations induced by the road unevenness onto the chassis. The design and tuning of these components aim to get tire road adhesion and driving comfort; this is a real trade-off between handling and comfort, starting from noise, vibration and harshness studies (NVH), where human tolerance limits are set, in terms of vertical or fore and aft vibrations. Conventional suspension systems incorporate an elastic member (spring), a damping element (shock absorber) and kinematic linkages. The damping task is obtained by converting the vibrational power into waste heat, thus these systems are simply passive: although they are cost-effective, they can only yield a fixed response without adapting to a variety of road irregularities and vehicle dynamic conditions [2].

In the last decades semi-active and active damping technologies have been developed. Adaptive or semi-active suspensions are made of dampers with tunable value parameters according to closed loop control laws: the damping coefficient is managed by means of valve or magneto rheological elements. In the active suspensions the hydraulic elements are substituted by active components, hydraulic or electromagnetic, that directly provide the required damping forces or factor through a control algorithm [3]. For instance, in figure

1.1 the control system computes the damping factor d_u and force F_d , starting from the chassis acceleration \ddot{z}_c together with measurement of chassis (z_c) and wheel (z_w) positions.

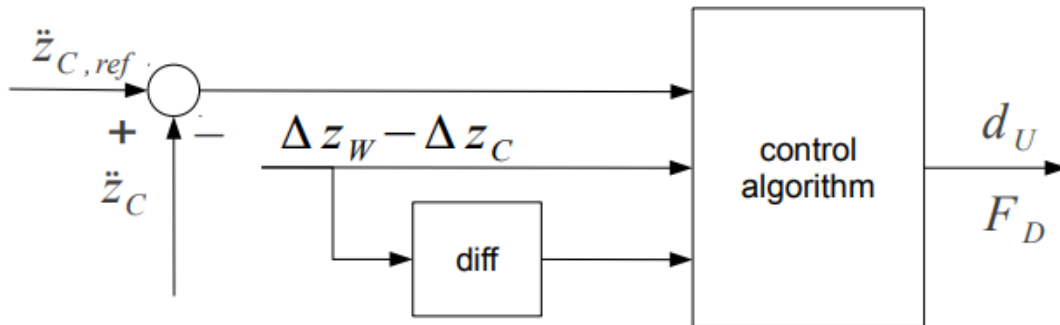


Figure 1. 1: Active suspension control algorithm [3]

Regenerative solutions are a further step forward: technologies that exploit the intrinsic reversibility of electric machines, with a suitable transmission system for the integration into the vehicle, to convert part of the otherwise dissipated power into electricity. As presented in previous studies, the average power lost by the suspension is proportional to the vehicle speed, tire stiffness and road roughness index [4]. For example, in a typical passenger car situation, travelling at a speed of **32 km/h**, the average dissipation on four corners is **133 W**; the total recovery of energy in the latter condition would lead to a CO_2 emission reduction above **6 g/km** for a D-class car [5]. This background shows the automotive industry's great interest for this topic, in fact the state of the art proposes different technologies for regenerative dampers.

At a first level analysis, looking at the nature of the suspension motion, linear electric motors seem a perfect candidate for regenerative damping. The first research, in this direction, found in literature, provides the feasibility of using a permanent-magnet linear motor with variable resistors instead of conventional shock absorbers [6]. Another solution consisted of an active electromagnetic suspension that employs a brushless tubular permanent-magnet machine to control the pitch and roll of the car [7]. Linear motors permit fast integration into the suspension layout, but their limited force density suggests the use of rotary electric motors, combined with a suitable linear to rotary conversion system [8]. This solution requires complex systems to convert the linear motion between the wheel hub and the uppers strut mount into an angular displacement. Ball screw, rack pinion and electro-hydrostatic transmissions have been investigated in the literature.

A novel concept has been introduced by Audi AG: they designed a regenerative suspension based on a rotary drive, composed of an electric machine and a gearbox [9].

This system is integrated to the suspension through a linkage, with benefits in terms of simplicity, power efficiency and envelope. Audi AG specified a total harvesting output from four corners between **100** and **150 W** on average during testing. Power transients go from **3 W** on a paved motorway to **613 W** on a rough road: this corresponds to CO₂ reductions above **3 g/km** [10]. Further improvements were made, always by Audi AG, through a similar technology with better comfort and safety: a predictive control strategy uses a camera to scan road irregularities in order to regulate the active suspension, making the cruise smoother [1]. In case of and hazardous situation identified by the vehicle, the active suspension raises the car body to improve the impact energy absorption capability. Moreover, longitudinal and lateral acceleration felt by the passengers can be lowered by accurately tilting the car body before entering a corner or during a braking [11]. This highlights the fact that these innovative technologies can be of relevant importance even for the step that the automotive industry is taking towards autonomous driving.

An electromechanical technology needs an accurate study of wear and fatigue, especially in a high-cycle task. This is not the case for hydraulic shock absorbers, which employ the electrohydrostatic actuation principle and are another option [2]. The linear to rotary conversion is performed by means of a hydraulic actuator directly interfaced to a motor-pump unit with a hydrostatic circuit. The main tribology aspects are bypassed thanks to the intrinsic lubrication of fluid-based solutions. In addition to that, being the fluid the means for power transmission, a flexible solution is offered in terms of placement within the suspension.

The present thesis' case study is intended for contributing a research project that has been developing for years. The object is the design of rotary regenerative shock absorbers, a flexible system that can be adopted in all the automotive field. In the next section, two suspensions implemented by the research group are presented. In the first one, the motor-pump unit is the core element in a hydraulic regenerative damper: hydraulic, mechanical and electric subsystems are integrated and optimized to maximize energy regeneration, preserving the native damping functionality. The other solution features a linkage and a gearbox to convert the motion. Both studies establish a novel system-level approach, that explores the role of different design aspects. It is relevant that they both integrate a suitable controlled electric machine, being the control of this component the focus of this thesis. The motor can provide a force that aids or counteracts the suspension linear motion. It respectively acts as a motor, by actively exerting mechanical power from its supply, or as a

generator, potentially performing mechanical-to-electrical power conversion, storing the kinetic energy from road irregularities into the battery [1].

1.2. Rotary regenerative dampers for automotive suspensions

The research study preceding the work of this thesis propose a system-level approach to comply with different requirements in all domains of interest [2]. Three fundamental specification sets are considered:

1. Damping requirements: the device must respect performance constraints of the reference vehicle. It means guarantying its damping functionality, considering the maximum damping specification and the road profile that the suspension faces during operation.
2. Target envelope: the prototype must ensure the packaging bounds of the suspension architecture; any interference in static and dynamic condition must be avoided.
3. Power supply requirements: the power stage of the device is connected to a battery; thus, the design should account for limitations regarding the DC voltage, charge-discharge rates and state of charge.

A correct design must respect the force-speed envelope that the regenerative damper has to span.

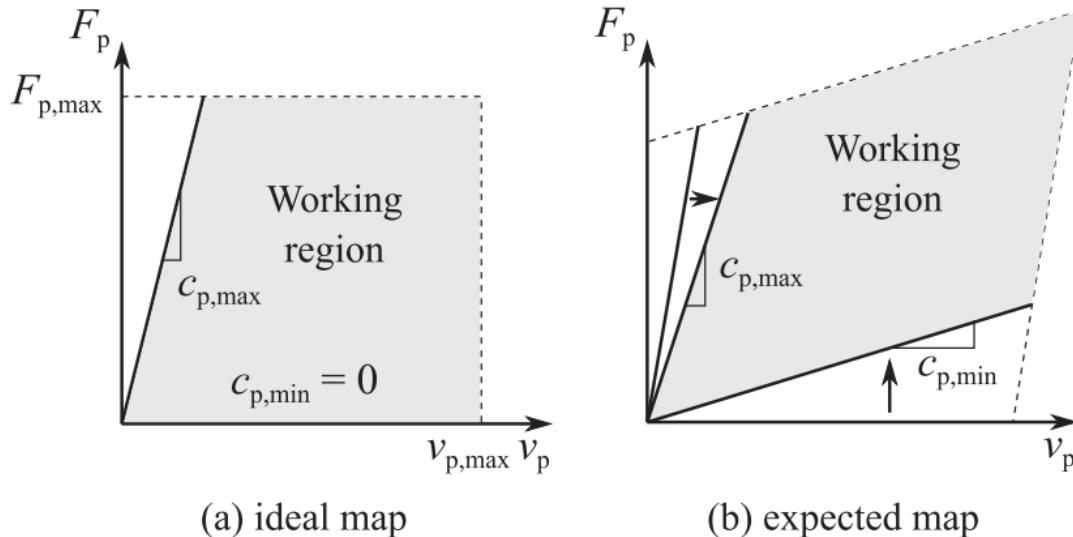


Figure 1. 2: Force-speed maps of the regenerative shock absorber [2]

The system must be able to satisfy the working region bounded by maximum force $F_{p,max}$, damping $c_{p,max}$ and speed $v_{p,max}$, as shown in figure 1.2. The damping coefficient provided by the motor is ideally expressed as

$$c_p = \frac{K_t K_e}{\tau^2 (R + R_{ext})} \quad (1.1)$$

where K_t is the torque constant of the electric motor, K_e the back electromotive force constant, R the phase resistance and R_{ext} the impedance of the power stage output [12]. This states that the power flows from motor to battery: the maximum attainable damping $c_{p,max}$ is limited by the short-circuit response, with null R_{ext} ; on contrary, the open-circuit response, $R_{ext} \rightarrow \infty$, will imply a minimum damping coefficient $c_{p,min}$. Moreover, being the linear-to-rotary conversion not perfectly efficient, the expected map differs from the ideal one (fig. 1.2). This is translated into a lower slope of any attainable damping behaviour and an additive output force that increases the output damping behaviour due to the losses. There is also a passive damping action, useful to maintain the vehicle stability, especially in case of system failure, because of the non-null $c_{p,min}$.

1.2.1. Hydraulic shock absorber

In this section, the main design features of the hydraulic shock absorber solution (fig. 1.3) are presented.

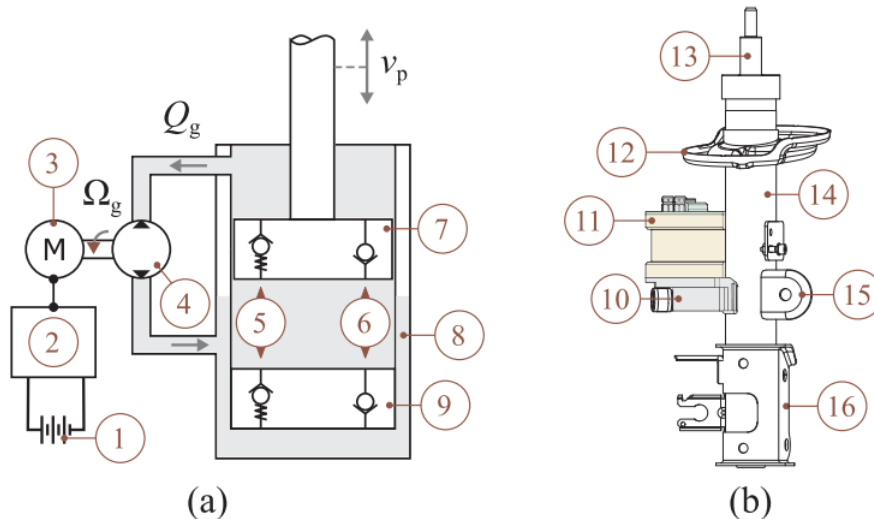


Figure 1.3: Layout of a hydraulic regenerative shock absorber. Concept scheme (a): battery (1), power stage (2), electric motor (3), hydraulic pump (4), pressure-relief valves (5), check valves (6), piston (7), gas accumulator (8), base (9). Prototype side view (b): manifold (10), motor pump unit (11), spring holder (12), rod (13), external tube (14), anti-roll bar bracket (15), wheel hub bracket (16) [2].

The system is made of a twin-tube shock absorber architecture connected to the hydraulic ports of a pump [2]. The piston oscillates inside the tube at a speed v_p in consequence of road unevenness. This motion generates an oil flow rate Q_g that drives the hydraulic pump; thus, the linear movement is converted into a rotary motion Ω_g . Since the pump is mechanically coupled to an electric machine (fig. 1.4), a control strategy of this device allows to manage the damping characteristic of the damper, also permitting the regenerative task. Moreover, the motor-pump unit is integrated onto the shock absorber tube with a manifold. This permits to obtain a compact system and minimizes the hydraulic losses. It also provides flexibility because the motor-pump group can be installed on any damper tube.



Figure 1. 4: Electro-hydrostatic motor prototype

Despite this, the power conversion from the hydraulic domain to the electrical one, till the battery, is affected by different unavoidable loss terms [2]. Firstly, the volumetric efficiency, affected by internal leakages, is given by

$$\eta_v = \frac{V_g \Omega_g}{Q_g} \quad (1.2)$$

where V_g is the fixed volumetric displacement. Then, due to hydraulic minor losses and mechanical friction, the hydro-mechanical efficiency is introduced,

$$\eta_{hm} = \frac{T_m}{V_g \Delta P_g} \quad (1.3)$$

in which T_m is the electromagnetic torque of the motor and ΔP_g the pump pressure drop. Finally, the last term is the electro-mechanical efficiency, attributed to motor and power-stage losses,

$$\eta_e = \frac{V_{dc} I_{dc}}{T_m \Omega_g} \quad (1.4)$$

being V_{dc} and I_{dc} the voltage and current of the power stage DC bus, respectively. The product of the three terms yields the total conversion efficiency of the system:

$$\eta_t = \eta_v \eta_{hm} \eta_e = \frac{V_{dc} I_{dc}}{\Delta P_g Q_g} \quad (1.5)$$

1.2.2. Electro-mechanical shock absorber

In the present section, what is presented is the second regenerative suspension system treated by the research group (fig. 1.5).

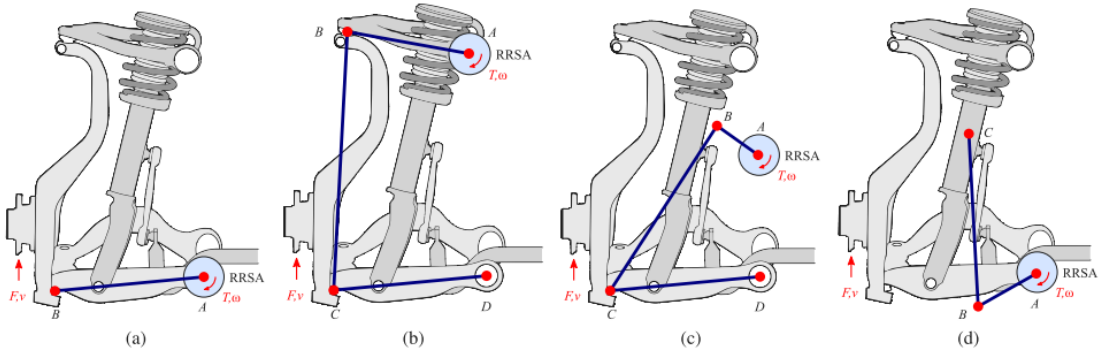


Figure 1. 5: Linkage solution (thick solid lines) [1]

To perform the motion conversion is used a linkage. As illustrated in figure 1.5 the wheel upright linear speed v is transformed into rotary motion ω with a transmission ratio $\tau_l = v/\omega$ [1]. During damping operation, the angular speed is converted into the angular speed of the electric machine, ω_m , by means of a gearbox, operating as speed multiplier with a transmission ratio $\tau_g = \omega/\omega_m$; therefore, the high-speed low-torque shaft of the gearbox is coupled to the rotor of an electric machine.

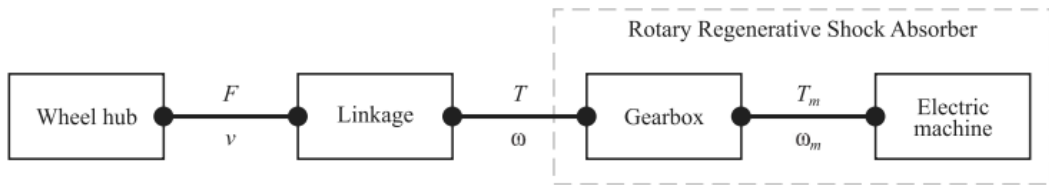


Figure 1. 6: Rotary regenerative damper working principle diagram [1]

The overall transmission ratio is defined as the ratio between the suspension linear speed and the electric machine angular speed: [1]

$$\tau_t = \tau_g \tau_l = \frac{v}{\omega_m} \quad (1.6)$$

This parameter plays an important role on the sizing of the motor. In an ideal static transmission, the electric machine torque is given by

$$T_m = \tau_t F \quad (1.7)$$

where F is the input force at the suspension. On contrary, any inertial (J_m) or dissipative contribution in the form of damping (c_m) is seen by the suspension as

$$c_{eq} = c_m / \tau_t^2 \quad (1.8)$$

$$m_{eq} = J_m / \tau_t^2 \quad (1.9)$$

So, small transmission ratio allows compact machines with low torque capability, but more friction loss effects. The equivalent inertia follows a similar trend: inertial contribution are dynamically relevant; in fact, they tend to stiffen and lock the suspension in high-frequency cycles [8]. Differently, when large transmission ratio values are used, there is a performance improvement at the cost of increasing size of the electric machine.

Working in this direction, the research group demonstrated with a prototype the feasibility of this solution. The device featured a compact design with a total addition of mass of **3.51 kg** per corner. From a performance point of view, it guaranteed a maximum damping of **11.32 kNs/m**, maximum damping-to-mass ratio of **3.23 kNs/(mkg)** and a maximum total conversion efficiency of **59.86 %**. Moreover, the prototype does not exceed the standard noise limitations [1]. These results highlight the possibility to use rotary damper technology for fully active automotive suspensions.



Figure 1. 7: Rotary regenerative motor prototype

1.2.3. *Power stage and control*

The electric machine type and its design, for both the aforementioned solutions, are based on the working conditions within different physical domains: mechanical (level of vibrations), electrical (current and voltage limitations) and thermal (temperature). In addition, the components of the power stage are chosen in parallel to the electric machine parameters and the supply requirements. Being compactness crucial in this application, a brushless permanent-magnet (PM) topology is the optimal option, that offers the highest torque-to-mass ratio among electric motors [13]. In particular, an inner rotor, radial flux, surface-mounted PM motor permits a better construction simplicity. Moreover, as regards as the battery supply, the DC bus voltage is limited to **48 V**.

A suitable control strategy is implemented considering the damping envelope and the limitations of the subsystems [2]. In literature there are examples of regenerative dampers that exploit a diode rectifier connected to a passive load or a DC-DC converter that feeds the battery [14]. This corresponds to a simple solution; however, it intrinsically excludes the possibility to work in active mode. In addition to that, a diode rectifier degrades the conversion efficiency due to its conduction losses. To ensure full-active functionality of the suspension, a power stage with three-phase full bridge is necessary: the prototypes developed by the research group employ an inverter constituted by three MOSFET phase legs. In an automotive implementation, a controlled power stage like this leads to the following benefits: [1]

- Operation on the active and regenerative quadrants.
- High conduction efficiency and null offsets due to bias voltage.
- The control loop forces the current to flow in quadrature to the machine flux, so no torque attenuation due to inductive effect.
- Possibility to reproduce the necessary damping specification by simply limiting the motor current.

The processing task is performed by a 32-bit floating-point digital signal processor, while the position feedback is read from an array of three Hall-effect latches and a PM array mounted to the end of the rotor; the DC bus and phase currents are measured by means of Hall-effect current probes [2]. The control strategy is represented in figure 1.6, it implements field-oriented control with a current loop constituted by a proportional-integral (PI) compensator and back-calculation anti-windup.

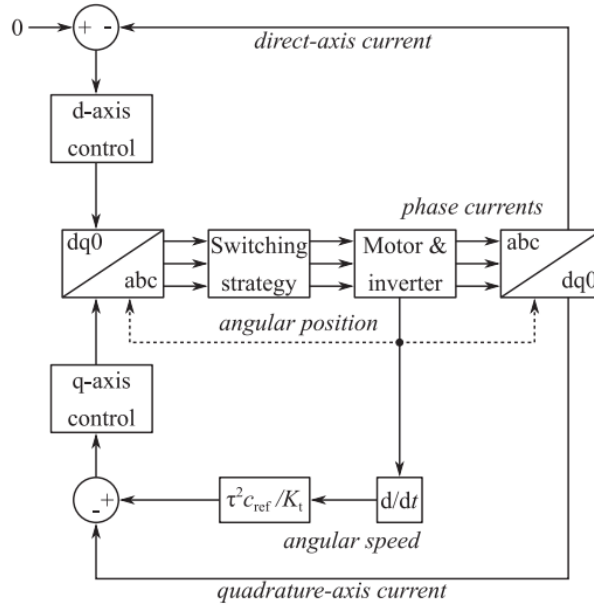


Figure 1. 8: Block diagram of the control strategy [2]

The control routine works synchronous to the phase switching frequency (40 kHz); the PI compensator tuning is done to mitigate the electromagnetic pole of the motor, setting a closed-loop bandwidth of 500 Hz. In addition to that, the direct-axis current reference is maintained always null, thus, the electric machine is controlled exclusively in the constant-torque region.

Finally, the quadrature-axis current is defined through a reference damping coefficient c_{ref} to assess the performance in the damping quadrant. As a matter of fact, the electromagnetic damping torque of the machine is proportional to the angular speed Ω_g :

$$T_m = \tau^2 c_{ref} \Omega_g \quad (1.10)$$

The present thesis work has its own foundation on what has been presented in this section: it aims at improving the current control strategy of the electric machine, providing more features through the development of a suitable control algorithm.

1.3. Thesis overview

The objective of this thesis is to design the motor control system and the ECU programming of the rotary regenerative dampers for automotive suspensions. The aim is to develop a control strategy, starting from power stage requirements at system and components level. Thus, many electrical domains have been investigated: from the battery

packs high-level definition to power electronics (3-phase inverter and microcontroller) and AC synchronous machines, together with vector control.

The main contribution of this work consists of adding features and refinements to the standard field-oriented control algorithm (FOC). The central aspects are the implementation of the flux weakening control and the regenerative phase management for the energy harvesting task. In addition to that, the substitution of the previous hardware control board is of paramount importance: a new TI development kit has been integrated in the system, leading to better debugging action.

1.3.1. Experimental method

The method utilized to achieve the goals follows a V-shaped development flow (fig. 1.9). Exactly as for software development V-model, the development process has started from the analysis of the requirements, functional specification of the system and of the power stage components. During the project definition phase, it was performed a detailed design of the control system first at high level and then at low level, going more in depth. The coding and implementation phase were made in MATLAB/Simulink environment together with the following test phases. These validation phases began from unit and system testing in simulation and ended with the integration and prototype testing of the power stage on a test bench. As demonstrated by the relationship in each step of the diagram, during the testing there have been some iteration phases, reshaping the control algorithm to better fit the system requests. Finally, important results have been verified, investigating different operating points of the electric machine, to validate the aforementioned thesis goals.

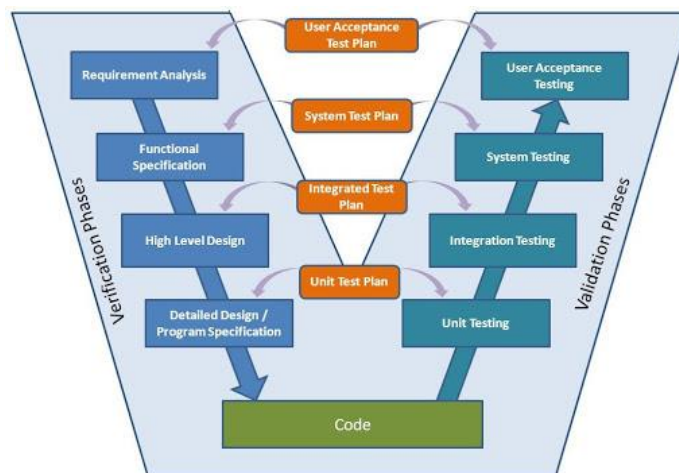


Figure 1. 9: V-shaped development flow

1.3.2. Control strategy

The control algorithm features a (sensored) field-oriented control of 3-phase surface-mounted permanent magnet synchronous motor (PMSM). The overall strategy is represented in figure 1.10. It performs the control of the stator current vector of the machine in dq synchronous coordinates, i. e. the rotor reference frame. This technique permits to obtain the desired torque at different operating conditions from the motor drive.

Firstly, the current reference generator converts the reference torque to the reference currents, following the MTPA concept. These fed the current controller, together with the feedback, coming from physical sensors or sensorless estimators. Here the closed loop PI regulators impose the current vector. In between there are the protection and auxiliary functions: field weakening control, with an outer voltage control loop, permits to reach higher velocities; current and voltage limitations are designed to respect the security of the system. Finally, the space vector pulse width modulation, chosen as switching strategy, generates the duty cycles from stator reference voltages. The voltage source inverter, then, converts them into the correspondent phase voltages physically imposed to the motor.

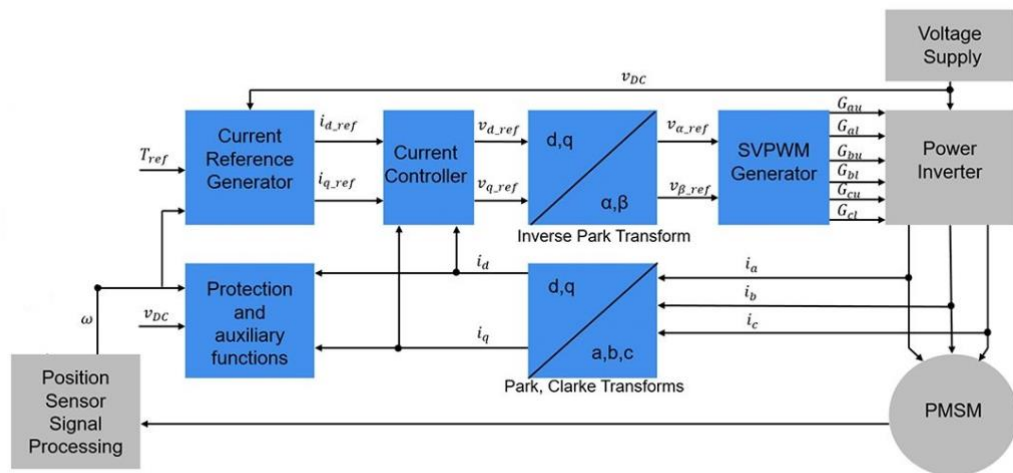


Figure 1. 10: Motor control strategy

1.3.3. *Thesis outline*

In the present work, the first step was the project definition: the functional specification analysis of the power stage has been developed, permitting to extrapolate the requirements for the motor control strategy. All the features and the tasks requested to the algorithm were defined; after that the high-level design has been implemented in parallel to the fundamental control theory and literature study. In this part, both the overall strategy and the single operations performed by the control have been highlighted, to describe in detail all the specifications.

Successively, the very programming part has been implemented in MATLAB/Simulink environment. The design of the control has travelled together with the preparation of the simulation, with an iterative process that involved simulation tests on two different motors, of which only one has been considered for the last part. After this first validation phase, the ECU implementation has been made, with the integration of the control algorithm in the power stage.

During the experimental campaign different power electronics devices, 3-phase inverter and launchpad have been treated and modified to make them work properly. A high-level analysis of the battery pack has been done. Finally, the test bench was prepared in order to obtain validation results, exploring different operating points of the motor.

2. Current control method

The following chapter presents theoretical and literature review about current control method, together with the design solutions chosen for the project work.

A digital vector control is realized by means of a DSP; for the case study, the TMS320F28379D Dual-Core microcontroller is used, permitting cost-effective design, by reducing system components and increasing performances. The discussed algorithm consists of field-oriented control of 3-phase permanent magnet synchronous motor. The FOC strategy maintains efficiency in a large range of velocities and can manage torque changes with transient phases by processing a dynamical model of the motor.

2.1. (Sensored) field-oriented control of 3-phase PMSM

This section presents the implementation of FOC for sinusoidal brushless motor. The sinusoidal voltage waveform fed to the drive is created using the space vector modulation technique; the minimum quantity of torque oscillations appears when piloting the sinusoidal BEMF motor with sinusoidal currents [15]. A brushless PMSM has a wound stator, a permanent magnet rotor structure with external or internal devices to sense rotor angular position. The sensors provide position feedback for monitoring frequency and amplitude of stator voltage reference in order to maintain rotation of the magnet assembly. The combination of an internal PM rotor and outer windings yield to the advantages of efficient heat dissipation, less rotor inertia and reduction of the motor size. In addition to that, the removal of brushes reduces noise, EMI generation and eliminates the need of brushes maintenance (see appendix A.2 for motor modelling and generalities recalls) [15].

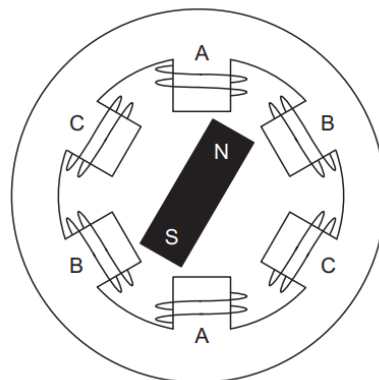


Figure 2. 1: 3-Phase synchronous motor with one PM pair pole rotor [15]

As regards as synchronous motor construction, PMs are rigidly assembled to the rotating axis to generate constant rotor flux, with constant magnitude. When energized, the stator windings create a rotating electromagnetic field, thus, to manage the rotating magnetic field stator currents control is necessary. The interaction between rotor and stator fluxes creates a torque: being the stator fixed to the frame and the rotor free to rotate, this latter will rotate generating a useful mechanical output. The angle between the rotor magnetic field and the stator field should be adequately controlled to achieve maximum torque and high electro-mechanical conversion efficiency [15]. For this reason, a good design permits to draw the minimum amount of current under the same speed and torque conditions. In synchronous motor operations the rotating stator field must rotate with the same frequency of the rotor permanent magnetic field, i.e., the rotor speed is rigidly related to the AC frequency imposed by the inverter. If this is not ensured, the rotor will face rapidly alternating positive and negative torque. The result is a bad torque production, with excessive mechanical vibration, noise and stresses on the machine components. Moreover, if the rotor inertia filters these oscillations, the rotor stops rotating at the synchronous frequency and starts responding to the average torque, which is zero, experiencing a phenomenon known as ‘pull-out’ [15]. Therefore, the angle between the rotor and stator field has to be equal to 90° to obtain the highest torque production, in the constant torque region; of course, the synchronization requires knowing the rotor position to generate the adequate stator field. This is possible by combining the different stator phases, permitting to have any direction and magnitude of the stator magnetic field.

In the present work, a surface permanent magnet (SPM) synchronous motor is under study. The torque produced by this type of machine is made by only the PM contribution: each stator current generates a torque component in association with the rotor magnetic field along the airgap, following the Lorenz law. In an SPM motor the permanent magnets are mounted on the surface of the stator; the PMs have almost the same magnetic permeability of the air, thus, the inductance computed along any direction is constant. The PM flux tends to align the rotor with the MMF generated by the stator, producing the torque (fig. 2.2). It is proportional to the external product between PM flux and stator MMF, therefore, for a given current amplitude the torque is maximized if the two vectors are orthogonal [16].

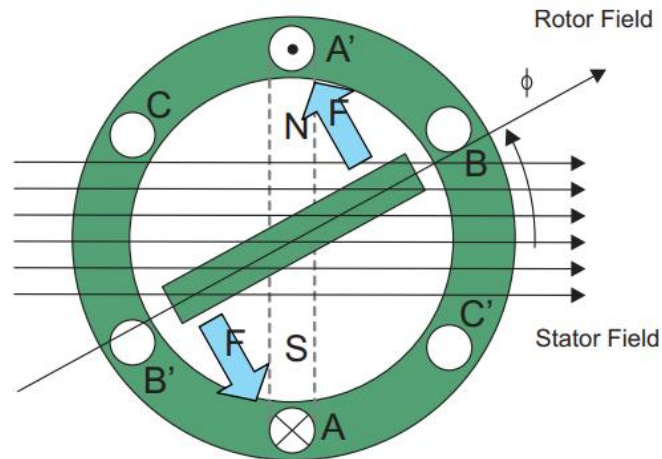


Figure 2. 2: Interaction between the rotating stator flux and the rotor flux [15]

2.1.1. *MTPA-Maximum torque per ampere*

In the following sub-section, the main standard features of the FOC algorithm are introduced. This is an advanced control strategy, applied to control the PM motor in order to achieve better dynamic performance. In AC machines the only source that can be controlled is given by the stator currents; stator phase voltage is the only source of power and magnetic field, thus, the flux and torque depend on each other [15]. The control algorithm uses mathematical transformations to decouple the torque generation and the magnetization functions in the machine; from such decoupling the rotor flux-oriented control name derives. Therefore, the goal is to separately control the torque generating and magnetizing the flux components. The processing capability provided by the DSP permits these mathematical transforms; moreover, the full algorithm can be executed at a fast rate, enabling higher dynamic performance. In addition to that, a dynamic model of the motor is used for several computations enhancing the overall quality of the control.

As previously stated, the torque produced in the synchronous motor is given by the vector cross product of the rotor and stator magnetic fields: the torque is maximum if the two fields are orthogonal, this implies to maintain the load at 90° . Being able to always ensure this condition, correctly orienting the flux, there is a reduction in the torque ripple and improvements in the dynamic response [15]. The scope is to guarantee that rotor and stator flux are in quadrature; the goal is to align the stator flux with the q axis of the rotor flux i.e., the orthogonal to the rotor flux. Hence, the stator current component in

quadrature with the rotor flux is governed to generate the reference torque, while the direct component is set to zero.

Basic FOC scheme

Figure 2.3 shows the basic scheme of current control with FOC [15]. It is visible the separation between different physical worlds:

- The microprocessor, made by control scripts.
- The electromechanical and electrical power conversion, with power electronics and motor, plus the measurements.

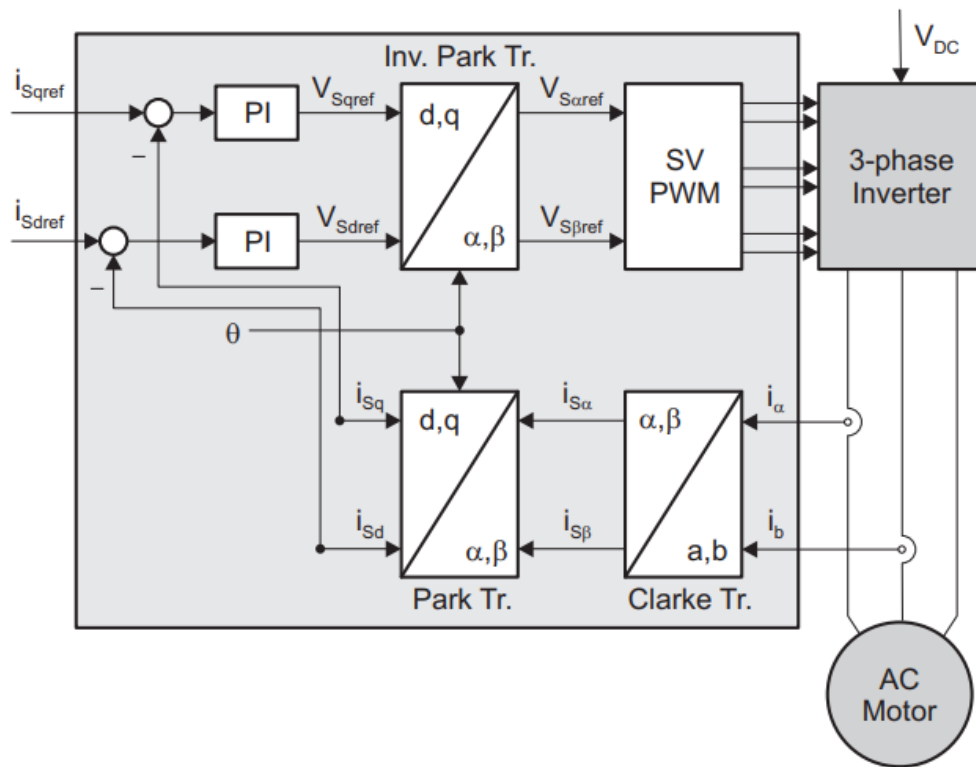


Figure 2. 3: Basic FOC control scheme for AC motor [15]

It permits to control the stator current vector in dq synchronous coordinate (rotor reference frame). This is a method to obtain the desired torque from the AC motor drive. The torque loop converts the reference torque into the adequate 3-phase reference voltages; then, the 3-phase inverter generates the correspondent phase voltages physically imposed to the motor. At the basis there are projections that suitably transform a three-phase time and speed dependent system into a time invariant system with two coordinates, that are d and q. These transformations are named Clarke and Park transformation, reported in appendix A.1. They project the machine into a structure similar to that of a DC

motor control, which handles instantaneous electrical quantities. For this reason, the control is accurate in every working condition, steady state or transient, independently from the limited bandwidth mathematical model. Thus, FOC englobes two important features:

- The simplicity in reaching constant references.
- The ease of applying direct torque control, since in the (d,q) coordinate system the torque is expressed as

$$T_m = \psi_R i_{sq} \quad (2.1)$$

where ψ_R is the rotor flux amplitude and i_{sq} is the torque component of the stator current vector; so, keeping a fixed value of the rotor flux, there is a linear relationship between torque and torque component i_{sq} [15].

The algorithm is fed by two constant input references: the torque component, in the q coordinate, and the flux component, in the d coordinate. Then, two motor phase currents are measured; these are inputs for the Clarke transformation block, which outputs the stator current in the alpha-beta plane. These other two projections are fed into the Park transformation module that provide the current in the d,q rotating reference frame. The latter represent the feedback currents, which are compared with the torque and flux references, respectively i_{sqref} and i_{sdref} . In standard FOC, implementing MTPA strategy, i_{sqref} is determined by the torque reference, while i_{sdref} is set to zero; in fact, in synchronous permanent magnet motors, the rotor flux is fixed determined by the magnets, so there is no need to generate one [15]. The PI current regulators produce the two reference voltages, in d and q axis. This type of controller is the most employed in eDrives, since typically there are plants with one dominant time constant. The reference voltages are transformed by an inverse Park module, giving the components of the stator vector voltage in the (α,β) stationary orthogonal reference frame. These are the inputs for the space vector PWM, which generates the signals to drive the inverter. This control algorithm needs the rotor flux position in order to use the Park and inverse Park transformations. The knowledge of this variable is fundamental for the overall systems functionality. An error in its computation can yield to a misalignment between rotor flux and with d axis, producing incorrect flux and torque components of the stator current. The figure 2.4 illustrates the (a,b,c), (α,β) , and (d,q) coordinate systems, with the correct position of the rotor flux, the

stator current and voltage space vector that rotates with the rotor reference frame at synchronous speed, for a generic PM motor [15].

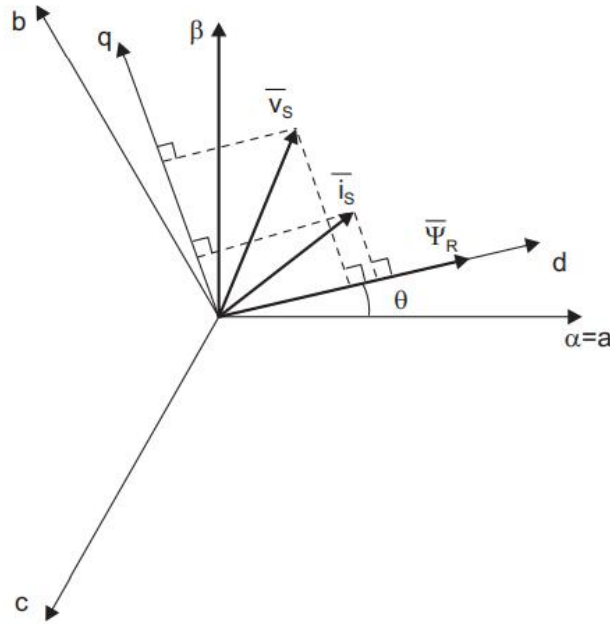


Figure 2. 4: Current, voltage and rotor flux space vectors in (a,b,c), (α,β), and (d,q) reference frames [15]

Torque control principle

The inverter acts as a current regulated voltage source: the reference voltages are managed to impose a reference stator current vector that yield the desired reference torque [16].

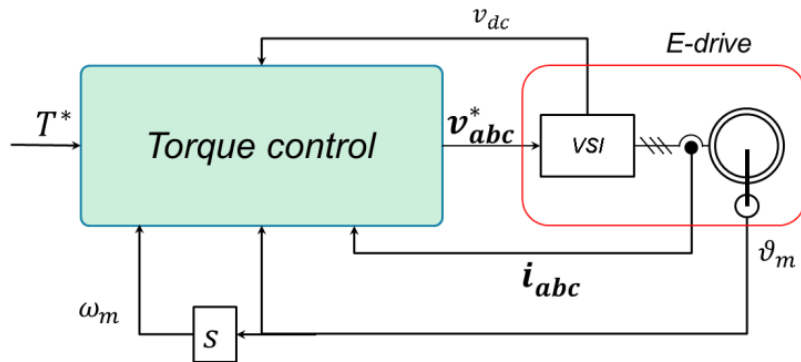


Figure 2. 5: Torque control schematic [16]

Thus, the first module that feed the controller is a torque reference generator. It translates the torque reference into the proper reference currents i_{dq}^* . The block needs the model of the electrical motor (see appendix A.2). The electromagnetic torque equation, valid for all 3-phase drives, is the following:

$$T = \frac{3}{2} \cdot p \cdot \lambda i \quad (2.2)$$

where p is the pole-pairs number, λ is the stator phase flux linkage and i is the stator phase current. In the dq reference frame the equation is:

$$T = \frac{3}{2} \cdot p \cdot (\lambda_d \cdot i_q - \lambda_q \cdot i_d) \quad (2.3)$$

Considering the SPM motor under study, the voltage equation and magnetic model are:

$$v_{dq} = R_s i_{dq} + \frac{d}{dt} \lambda_{dq} + j\omega \lambda_{dq} \quad (2.4)$$

$$\lambda_{dq} = L_s i_{dq} + \begin{bmatrix} \lambda_m \\ 0 \end{bmatrix} \quad (2.5)$$

being v the stator phase voltage, R_s the stator phase resistance, ω the electrical angular speed, L_s the synchronous inductance and λ_m the PM flux linkage [16]. Then, the torque equation becomes:

$$T = \frac{3}{2} p \lambda_m i_q \quad (2.6)$$

Finally, the torque command is translated into a reference current input:

$$\begin{cases} i_d^* = 0 \\ i_q^* = \frac{T^*}{\frac{3}{2} p \lambda_m} \end{cases} \quad (2.7)$$

The aforementioned current command gives the trajectory in the dq plane corresponding to the maximum torque for a given amplitude of the current vector (MTPA). The goal is also to minimize the machine losses in order to maximize its efficiency; in fact, the i_d^* reference is set to zero, since it does not give any contribution for torque production but would add Joule losses. This strategy is used also in case of regeneration or braking: the optimal current vector still follows the MTPA with negative torque reference, reversing the i_q^* current component.

As previously mentioned, the load angle control is fundamental for the efficient functionality of the system. It is possible to write the torque as a function of the flux linkage only, from equation 2.5 and 2.6:

$$T = \frac{\frac{3}{2} p (\lambda_q \cdot \lambda_m)}{L_s} = \frac{3}{2} \cdot \frac{p}{L_s} \cdot \lambda_m \cdot |\lambda| \cdot \sin \delta \quad (2.8)$$

where δ is the load angle i.e., the angle between stator flux and the PM flux linkage [16]. In figure 2.6 the mechanical characteristic of the torque, at steady state, for constant $|\lambda|$, in function of δ is shown.

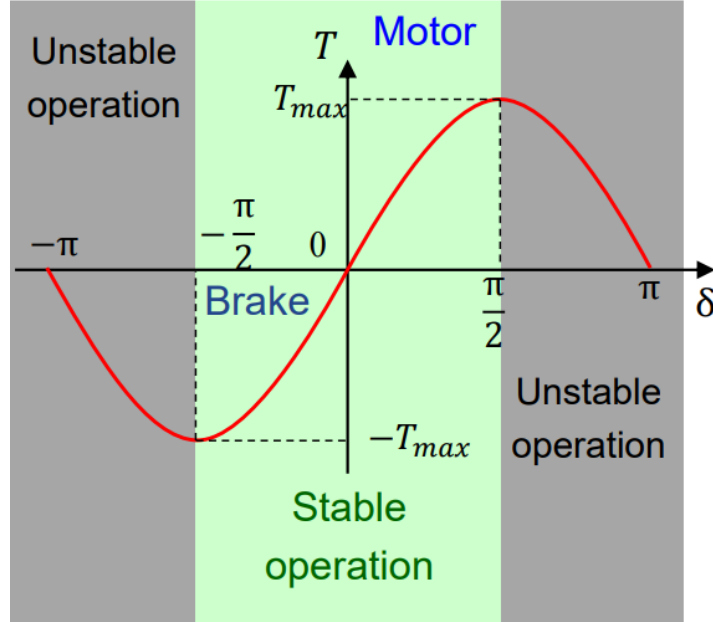


Figure 2. 6: Mechanical characteristic of the torque [16]

The torque is maximized when the load angle is 90 electrical degrees, with null λ_d :

$$T_{max} = \frac{3}{2} \cdot \frac{p}{L_s} \cdot \lambda_m \cdot |\lambda| \quad (2.9)$$

The machine remains in stable operation condition only if $\delta \in \left[-\frac{\pi}{2}, \frac{\pi}{2}\right]$, otherwise the synchronization is lost and the torque has zero mean value with huge pulsations [16].

Current vector control (CVC)

The current control loop is the basic feature for the controls of the electrical power conversion systems. The current in a power converter must be limited below the overcurrent limits of the components, otherwise the hardware protection triggers stopping the operation; in addition to that, the current is a state variable for an eDrive and, as previously said, controlling the current for an electric motor indirectly means torque control [16]. The current vector is imposed to the machine through closed loop PI regulators (fig 2.7).

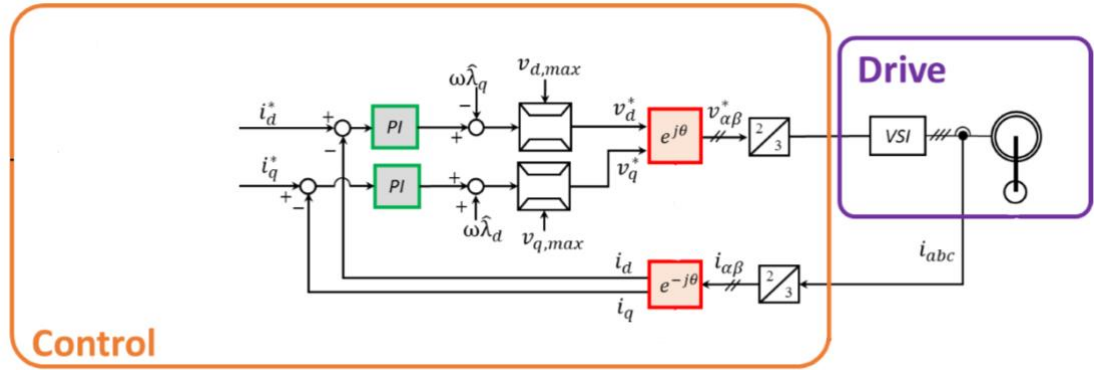


Figure 2. 7: CVC scheme [16]

For an SPM motor, CVC-FOC requires the knowledge of current measurements, rotor position, λ_m and L_s ; for the last two variables a reference value is adopted at calibration stage, neglecting magnetic saturation and temperature dependence. The current controller is designed in Laplace domain, using the transfer functions of the dynamic model of the SPM machine (eqn. 2.10) and of the power converter with digital control (eqn. 2.11):

$$H_m(s) = \frac{1}{R_s + sL_s} \quad (2.10)$$

$$H_{conv}(s) = \frac{1}{1 + s\tau_{VSI}} \quad (2.11)$$

They are both approximated as first order low-pass filters, respectively with time constant $\tau_m = L_s/R_s$ and $\tau_{VSI} = 1.5T_s$, where T_s is the sampling time. Thus, they compose a second order plant with two time constants: the slow one given by the motor (dominant pole) and the fast given by the converter delay. Moreover, ideal current feedback is assumed [16].

The PI controller, instead, has a real zero and a pole in the origin; it is composed of a proportional gain k_p and an integral gain k_i . The proportional part reacts first to an error change, while the integral part moves slowly and if the error is removed it represents the steady-state output of the controller. It is used to get zero steady-state error; the regulator transfer function is:

$$H_{pi}(s) = \frac{k_i + sk_p}{s} \quad (2.12)$$

Figure 2.8 depicts the overall closed loop control system transfer functions, while figure 2.9 represents its Bode diagram.

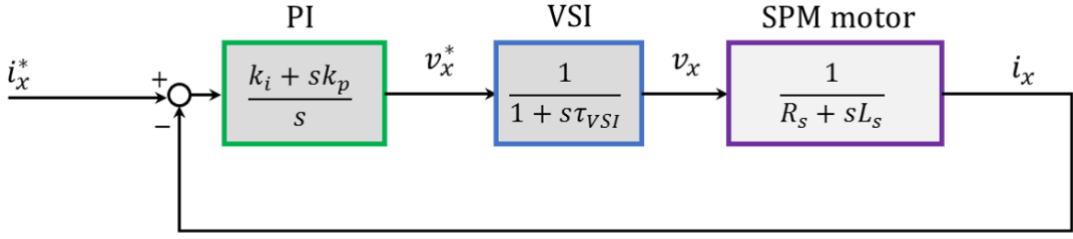


Figure 2. 8: CVC transfer functions [16]

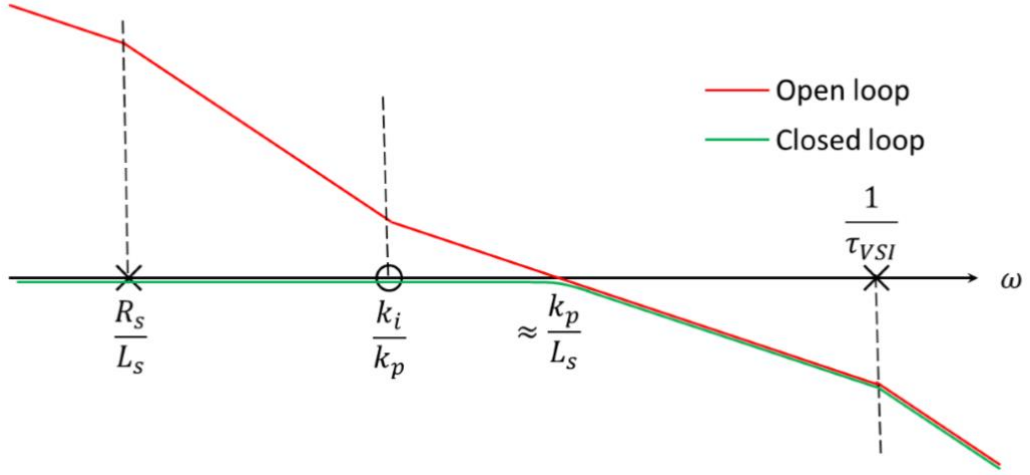


Figure 2. 9: CVC Bode diagram [16]

The regulator zero removes the dominant electrical pole; the crossover frequency ω_c (current control bandwidth) is approximated as

$$\omega_b \cong \frac{k_p}{L_s} \quad (2.13)$$

so, it is imposed by the proportional gain. In order to maintain an adequate phase margin, the maximum crossover frequency is fixed at about one tenth the sampling frequency $f_s = 1/T_s$. Therefore, the following equations give a method to calibrate the controller [16]:

$$\begin{cases} \omega_b \ll \frac{1}{\tau_{VSI}} \\ k_p = L_s \omega_b \\ k_i = k_p \frac{R_s}{L_s} \end{cases} \quad (2.14)$$

Moreover, at steady state and for medium/high speed the voltage is mainly composed by the motional term:

$$\begin{cases} v_d \approx -\omega \lambda_q \\ v_q \approx \omega \lambda_d \end{cases} \quad (2.15)$$

As in figure 2.7 the performance can be enhanced by adding the motional term as a feed-forward at the output of the controller.

At the end, the PI current controller have also limited voltage output, according to the inverter and battery source voltage limits:

$$\begin{cases} v_{d,max} = v_{max} = \frac{v_{dc}}{\sqrt{3}} \\ v_{q,max} = \sqrt{v_{max}^2 - (v_d^*)^2} \end{cases} \quad (2.16)$$

where v_{ma} is the inverter maximum voltage and v_{dc} is the DC-link voltage.

2.1.2. *MTPV-Flux weakening control*

What presented in the previous sub-section are the standard characteristics of the FOC control algorithm. In this sub-section is presented an additional feature to improve the motor control strategies: field weakening control (FWC), whose implementation is one of the thesis' goals.

A motor drive is composed by the motor with its inverter and controller. For every drive, the control variables must be limited to operate in a reliable and safe work range. In particular, the stator voltage is bounded by the inverter maximum voltage v_{max} while the stator current is limited by the inverter current capability and thermal constraints. Consequently, the rated torque is the maximum torque that can be reached with rated current; also, the torque slew rate should respect mechanical constraints, together with the motor speed [16].

Torque-speed characteristic

The torque-speed characteristic of a generic IPM machine is ideally determined by seven variables: the quantity of phases, the number of pole-pairs p , the inverter maximum voltage v_{max} , the inverter maximum current i_{max} , the d and q-axis inductances and the magnetic flux-linkage λ_m [17]. Neglecting the resistive voltage drop, the stator voltage amplitude at steady state is proportional to the rotor electrical velocity and flux amplitude:

$$v_{dq} = R_s \cdot i_{dq} + \frac{d\lambda_{dq}}{dt} + j\omega\lambda_{dq} \cong j\omega\lambda_{dq} \quad (2.17)$$

The base speed ω_b is defined as the speed at which the drive delivers rated torque with maximum voltage and current i.e., speed that can be reached with rated flux amplitude respecting the voltage limit:

$$|v_{dq}| \cong \omega |\lambda_{dq}| \rightarrow |\lambda| = \frac{v_{max}}{\omega} \quad (2.18)$$

To rotate faster than ω_b it is necessary to lower the flux amplitude (field-weakening operation). In this speed range, since the flux is decreased, the torque capability will be reduced. Instead, the operation below the base speed is named constant-torque speed range: in fact, without voltage limitation, the maximum torque capability is constant and dependent on I_{max} [16]. On contrary, above the base speed, a constant power characteristic is preferable; in this case the maximum torque decreases with the speed. However, the maximum power of the system is not constant during all the flux weakening operation: the maximum speed at which constant power is ensured is ω_p ; the constant power speed range is defined as ω_p/ω_b and it should be in the range 2 – 10 for traction applications [17]. The inverter utilisation at a certain speed is the ratio of the machine output power to the inverter kVA capability; an ideal field-weakening motor is lossless and has unity inverter utilisation from ω_b to infinite speeds. Figure 2.10 summarizes these concepts together with torque-speed characteristic.

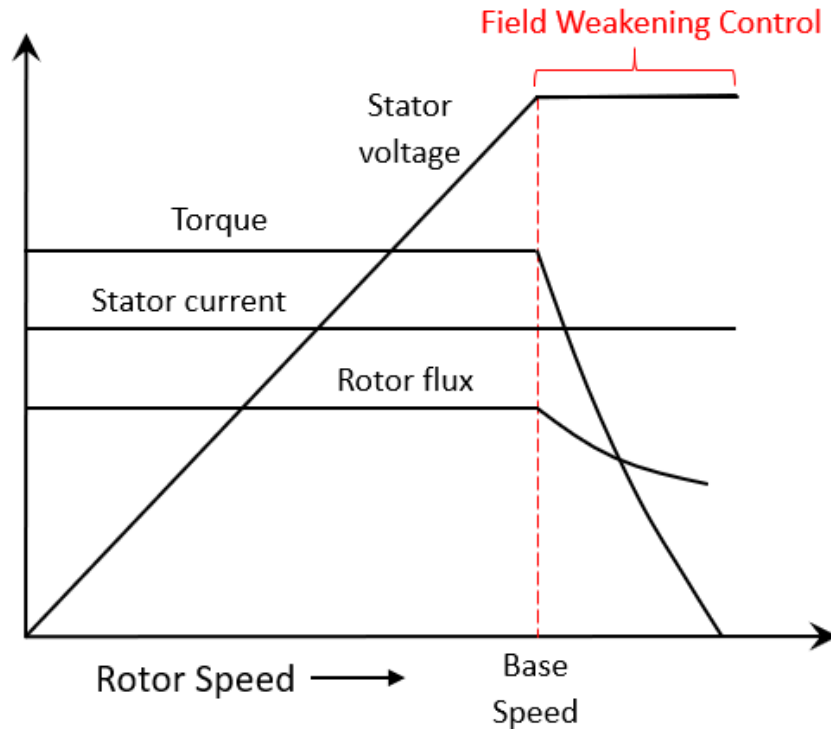


Figure 2. 10: Torque-speed characteristic

It shows that the motor's BEMF rises proportionally to the motor speed. This occurs in the constant torque region, where the standard FOC is a suitable strategy to regulate the drive. When the speed continues to increase, the applied voltage reaches the maximum value and the back EMF voltage exceeds the applied one, preventing the motor speed from increasing. In order to rise the motor speed above its base speed, field-weakening operation is used maintaining a constant output power, which is the product between torque and motor speed.

These features are strongly related to the aforementioned limitations. If the drive is fed by an inverter with same current capability but higher DC-link voltage, the maximum torque is unaffected while the base speed is increased: consequently, more power can be requested from the same motor [16]. Instead, the inverter current capability influences the maximum torque that can be obtained from the drive. In this case, the relationship between maximum torque and I_{max} is non-linear and depends on the machine typology because of the flux dependency on the current and variable phase displacement between the flux and the current.

PM and reluctance motors have a fixed excitation which inherently limit their field-weakening capability. Thus, real brushless synchronous AC drives have three operating modes (fig. 2.11).

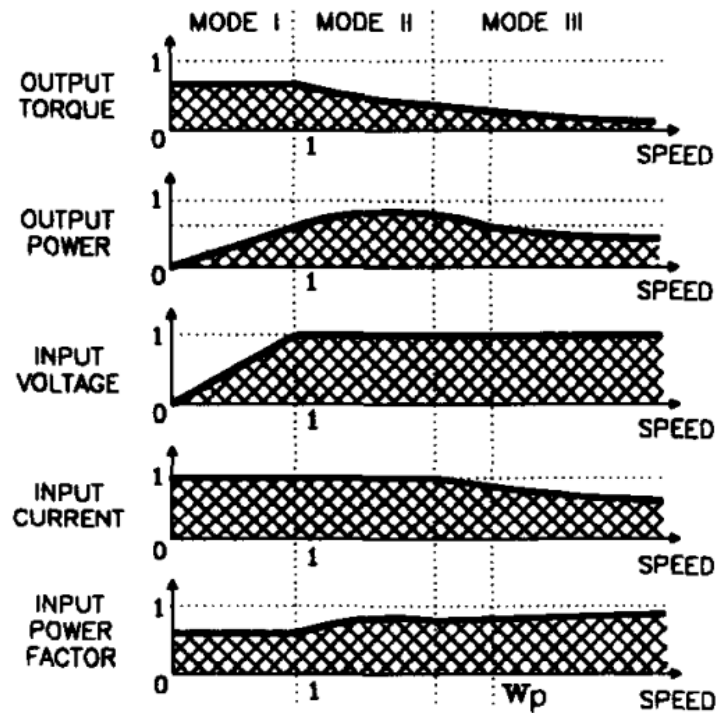


Figure 2. 11: Field-weakening characteristics [17]

- Mode 1 is the current-limited region, with constant torque capability; the speed range is from zero to ω_b .
- Mode 2 corresponds to the current and voltage-limited region.
- Mode 3 is the only voltage-limited region [17].

Circle diagram

Flux weakening is reached by forcing negative d-axis current, that goes in contrast with λ_m and reduces the total flux [16]. For synchronous motors the behaviour at field-weakening depends on the ratio between I_{max} and the machine characteristic current I_0 , which is the d-axis current that removes the machine flux, from equation 2.5:

$$I_0 = -\frac{\lambda_m}{L_d} \quad (2.19)$$

From the magnetic model of an SPM machine (eqn. 2.4-2.5), considering only the motional terms of the voltage (eqn. 2.15), the inverter current and voltage constraints in the (d,q) plane are derived:

$$i_d^2 + i_q^2 \leq i_{max}^2 \quad (2.20)$$

$$v_d^2 + v_q^2 \leq v_{max}^2 \quad (2.21)$$

The current constraint is represented as a circle in the origin with constant radius in the circle diagram; the voltage limitation is rewritten as:

$$\left(i_d + \frac{\lambda_m}{L_s}\right)^2 + i_q^2 \leq \left(\frac{V_{max}}{\omega L_s}\right)^2 \quad (2.22)$$

which is a circle centred in I_0 and speed dependent radius; the circle reduces as the speed increases [16]. The centre is also named infinite speed operating point since the working point must converge towards it at high speed [17].

The FWC rotates the stator current vector from the q-axis i.e., the MTPA locus, to the negative d-axis: since the maximum current is constant, i_q must be lowered and the current vector follows the I_{max} circle. In the following lines, the flux-weakening operation in the circle diagram for an SPM motor is presented, for three different cases. The circle diagram is a graphical representation of the motor's current and voltage limitation together with their influence on the steady-state operating points allowed.

- Case 1: $I_{max} < |I_o|$

Over the base speed, the stator current vector is rotated and the flux reduces; the working points that respect both current and voltage constraints are within the current circle. For this drive, the rotation of the current generates a small reduction of the flux, at the cost of a huge drop in the q-axis current; this provides limited flux-weakening range, with the power that drops rapidly [16].

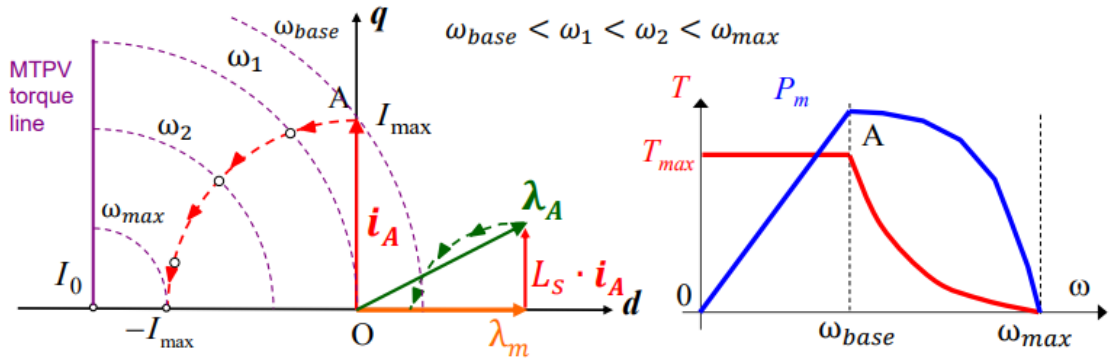


Figure 2.12: FWC first case [16]

- Case 2: $I_{max} = |I_o|$

Differently, in this case a lower rotation of the current is necessary to week the flux, entailing lower reduction in torque capability. This is the optimal motor design with constant power operation above the base speed and virtually infinite maximum speed. It is achieved increasing the inductance of the stator and decreasing λ_m : the output power at base speed decreases slightly but the field-weakening range improves a lot. This performance is obtained with:

$$\lambda_N = \sqrt{\lambda_m^2 + L_S |I_o|^2} \rightarrow \lambda_N = \lambda_m \sqrt{2} \quad (2.23)$$

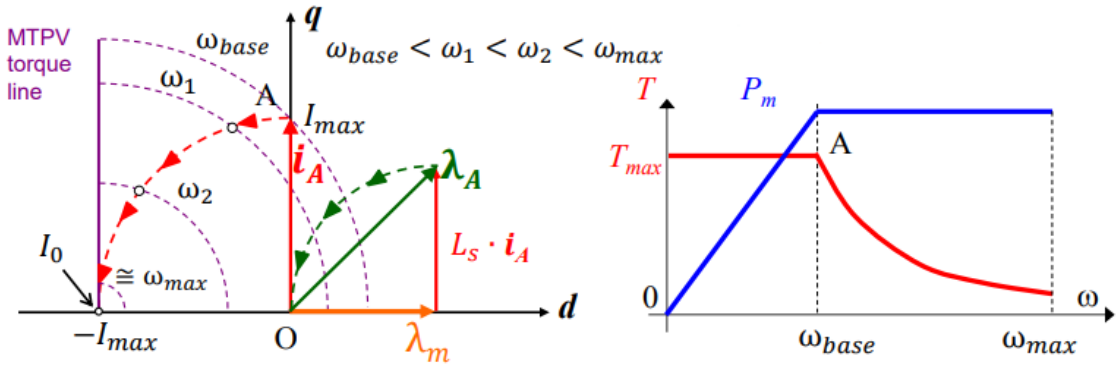


Figure 2.13: FWC second case [16]

- Case 3: $I_{max} > |I_o|$

Decreasing λ_N below the previous value, introduces this new operation. Firstly, from A to B, the behaviour is the optimal one, with constant output power. Then, when the d-axis current reaches the I_o value, in point B, the stator flux vector reaches the q-axis, corresponding to MTPV range, which is the locus of points with the highest torque for a given flux amplitude. Over this point, a further rotation is not possible since it would yield negative d-axis flux, leading to instability. Thus, the total current must be reduced, moving along the MTPV.

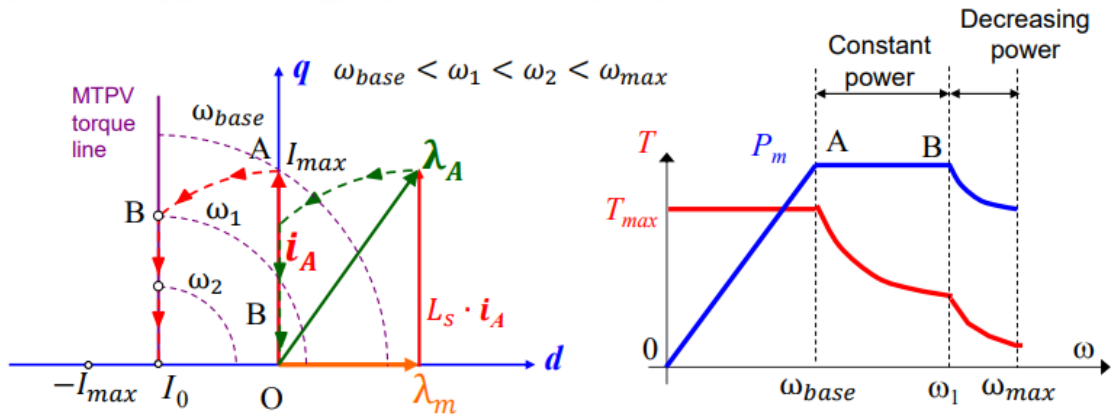


Figure 2.14: FWC third case [16]

Summarizing, in all the three cases, the trajectory starts in mode 1: the maximum torque is obtained operating at rated current with the optimal torque per ampere current angle. Successively, there is the mode 2 operation, where the voltage and current-limit loci intersect. Finally, only for the last case, the mode 3 occurs, with only voltage-limited region. In addition to that, the drives are distinguished in finite or infinite maximum speed. For finite maximum speed motors, the infinite speed operating point is positioned outside the current-limit circle; on contrary, for infinite maximum speed machines it lies within this bound, so the operating point converge on it at high speed through the MTPV operation [17].

Flux-weakening controller

One of the solutions found in literature to implement the flux-weakening control strategy for SPM drive consist in adding an outer voltage control loop (fig. 2.15) [16].

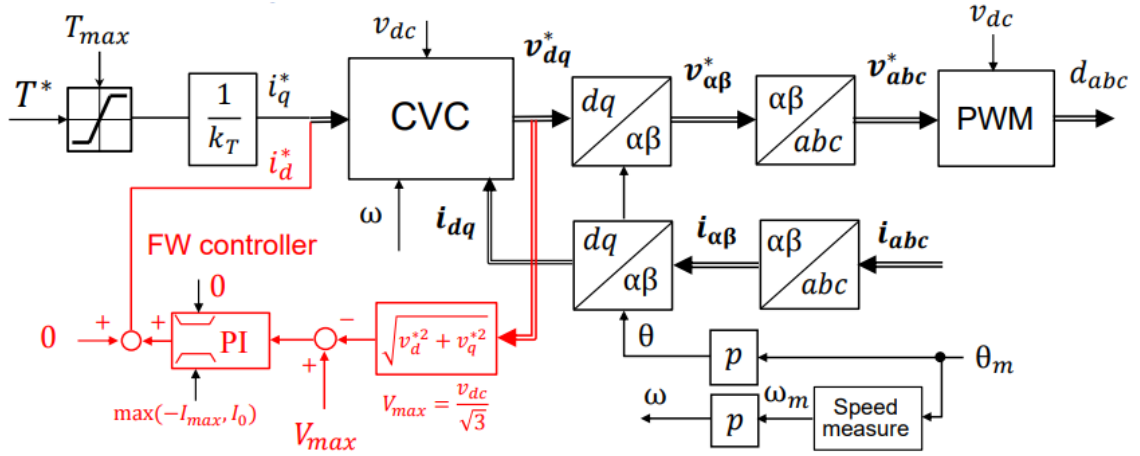


Figure 2. 15: Flux-weakening controller [16]

If the voltage request exceeds the maximum available voltage, the d-axis current is set to a negative value and the flux is weakened according to the aforementioned operations. Moreover, a suitable current saturation block, positioned before the current loop, must be properly designed.

2.2. Space vector modulation

In the following section the space vector modulation technique (SVM) is presented. It is a strategy responsible for producing pulse width modulated signals to control the switches of the inverter, which then generates the requested modulated voltage to drive the machine at the desired operating point. In particular, it operates on the reference voltage vector to provide appropriate gate signals for the inverter every PWM period, with the scope of obtaining continuously rotating space vector [18].

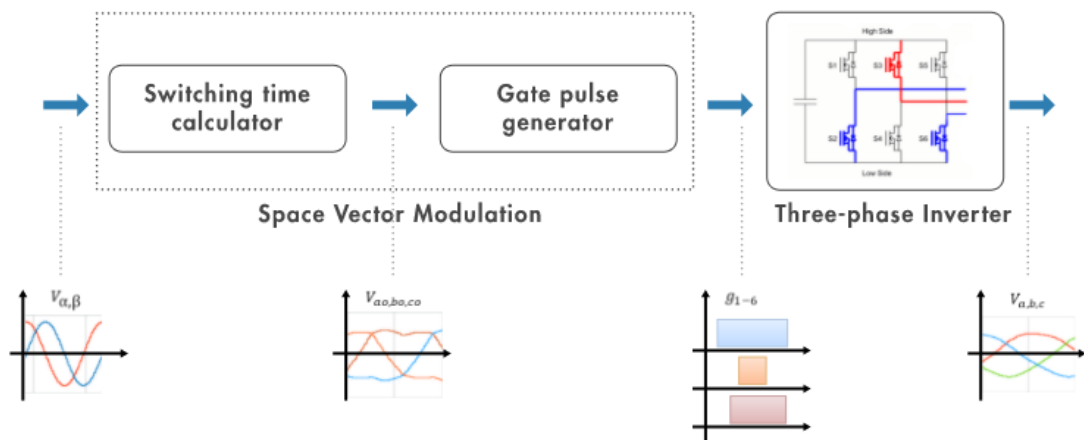


Figure 2. 16: Space vector modulation workflow [18]

For every PWM period, with voltage vector as input reference, the SVM strategy:

- Calculates on and off-gating times based on the reference voltage vector.
- Uses these to generate the double hump modulation waveforms.
- Uses again gating times to define appropriate gate pulses for the inverter switches.

The shape of the generated modulation wave with a double hump improves the utilization of the available DC bus voltage; this permits to obtain a better rated voltage output when compared with the standard modulation techniques i.e., sinusoidal pulse width modulation [18].

2.2.1. Vectorial analysis of the 3-phase inverter

Any three-phase system can be represented uniquely by a rotating vector:

$$a_s = \frac{2}{3} \cdot [a_x(t) + a \cdot a_y(t) + a^2 \cdot a_z(t)] \quad (2.24)$$

where $a = e^{j\frac{2\pi}{3}}$ and $a^2 = e^{j\frac{4\pi}{3}}$. By means of the Clarke transformation (see appendix A.1) it is possible to obtain the vectorial representation in (α, β) orthogonal 2-phase system, where can be uniquely defined a vector in the complex plane by its components:

$$a_s = A_\alpha + j \cdot A_\beta \quad (2.25)$$

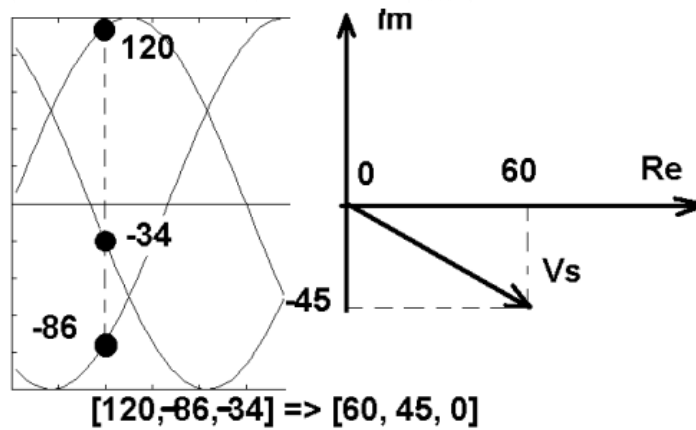


Figure 2.17: Equivalence between the 3-ph system and vectorial representation [19]

The result is a unique correspondence between a space vector in the complex plane and a three-phase system [19].

Considering the concept of SVM for motor control on a three-phase voltage source inverter with six switches, there are eight valid switching combinations, corresponding in six non-null output voltages and two null voltage vectors.

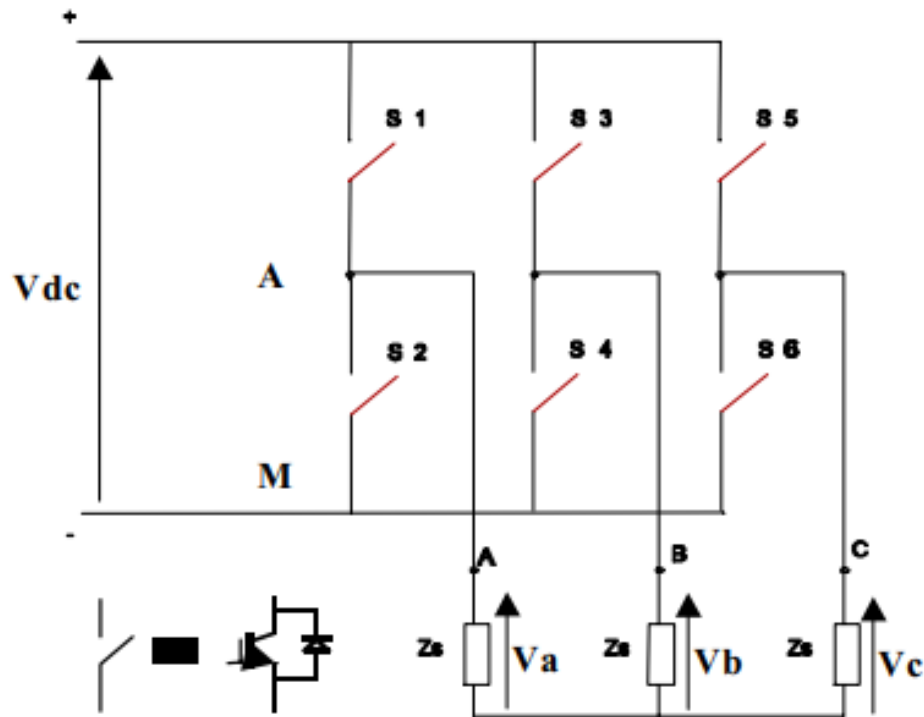


Fig.2 Three-phase voltage-source inverter

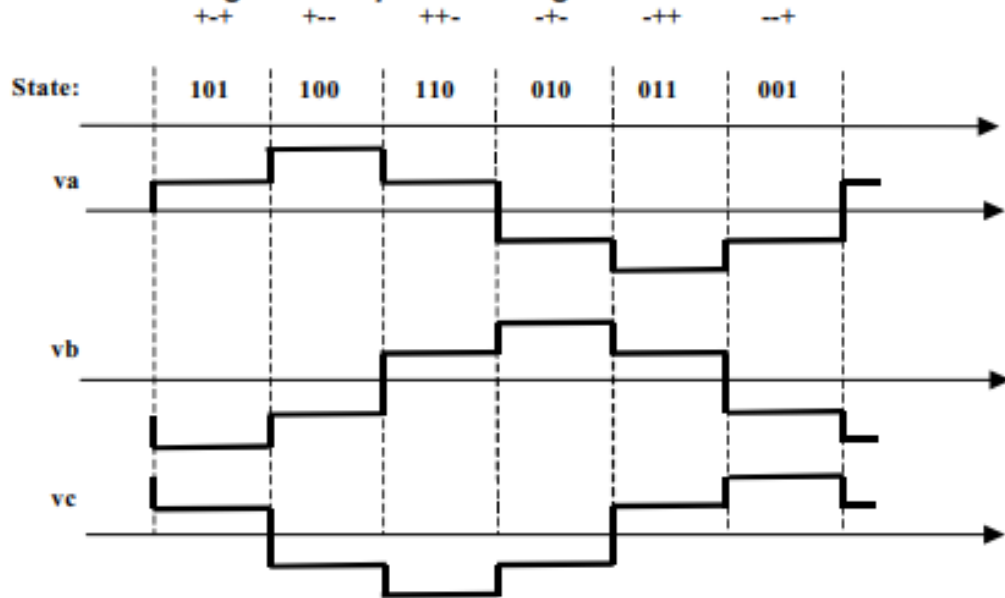


Figure 2. 18: Output voltage waveforms and state switching functions [19]

Each switching function configuration results in a specific voltage applied to drive terminals; these voltages are basic space vectors and represent their magnitude and direction in a space vector hexagon. Thus, there are 6 active switching vectors and two vectors corresponding to zero states. The amplitude of the active ones is $2v_{dc}/3$; moreover, since the output voltages are at $2\pi/3$ out of phase each other, the space vector system can occupy a number of positions with an order multiple of three [19].

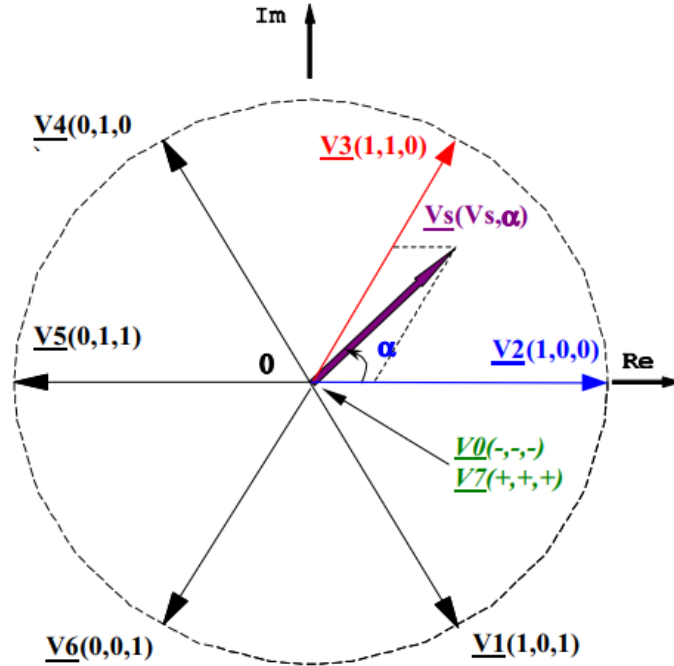


Figure 2. 19: Voltage vectors of a 3-phase inverter [19]

2.2.2. Pulse-width modulation

The control of electric power is performed by means of power converters: these transfer energy from a source in a switched operation mode, ensuring high conversion efficiency. PWM techniques are the algorithms that generates the switching functions. In general, since the voltage sweeps different discrete positions in the complex plane, its time integral leads to a polygon close to a circle. The torque ripple of the drive has a close relationship to that deviation from an ideal circular locus; this difference produced by a PWM inverter causes the torque pulsations. These latter can be lowered with a high carrier frequency, providing more zero vector states, although, the limitation of switching frequency is preferable due to less switching loss. This is a fundamental trade-off when designing a switching algorithm [19]. In addition to that, because of the complexity of the control and mathematical transformations, digital implementation is more efficient. The main performance index is the modulation index:

$$m = \frac{v}{\frac{v_{dc}}{2}} \quad (2.26)$$

Considering the three-phase inverter in figure 2.18, the ideal condition would be to have a space vector that follows a circular locus. This cannot be achieved by a switching power converter that can only reach discrete positions of the voltage space vector. Thus, each

desired position on the circular locus can be obtained by an average relationship between two neighbouring active vectors; zero state vectors are then used to fill-up the gap to a constant sampling interval. In particular, the switching states that correspond to the basic space vectors decide the direction while the null vectors are used to set the magnitude, in order to approximate a voltage vector of any magnitude, at any position, inside the space vector hexagon [18]. By controlling the switching sequence, so the ON time duration of pulses, any voltage vector with varying amplitude and direction is achievable: the goal of this technique is to provide switching sequences that correspond to the reference voltage vector for every PWM period to obtain a continuously rotating space vector.

A desired voltage space vector V_s , as in figure 2.19, is obtained through the following expression:

$$V_s \cdot T_s = V_a \cdot t_a + V_b \cdot t_b + V_0 \cdot t_0 \quad (2.27)$$

where T_s is equal to the sampling period of the given circular locus, while t_a and t_b are the time intervals allocated to the adjacent vectors V_a and V_b . In particular, the following relations determines the time intervals:

$$\left\{ \begin{array}{l} t_a = \frac{\sqrt{3}V_s}{v_{dc}} \cdot T_s \cdot \sin\left(\frac{\pi}{3} - \alpha\right) \\ t_b = \frac{\sqrt{3}V_s}{v_{dc}} \cdot T_s \cdot \sin \alpha \\ t_0 = T_s - t_a - t_b \end{array} \right. \quad (2.28)$$

In a digital implementation, these equations are carried based on a memory look-up table for the sine function [19]. Successively, it is advantageous to define a function named ‘switching reference function’ that represents the duty ratio of each inverter leg i.e., the conduction time normalized to the sampling period for a given switch: it is a mathematical function with variation between 0 and 1, centred in 0.5 (fig. 2.20).

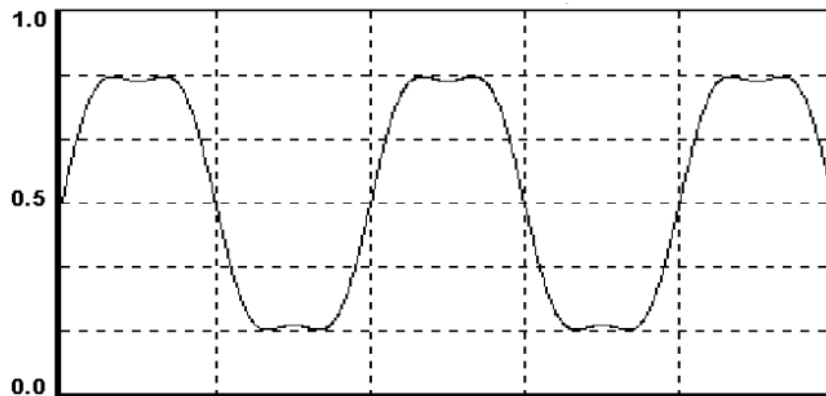


Figure 2. 20: Reference function for SVM [19]

It is derived by means of algebraic operations between the time intervals t_a , t_b and the time allocated to homopolar states within the same sampling interval. A third harmonic is present in the function but it is not inside the output phase or line voltages [19].

At the end, this strategy generates gate pulses as a result of comparing the modulation wave with a suitable carrier wave. The presence of the third harmonic yield to the possibility to extend the inverter linearity, improving the utilization of the inverter DC-link voltage. Figure 2.21 and 2.22 shows the resulting duty cycles for given reference voltages.

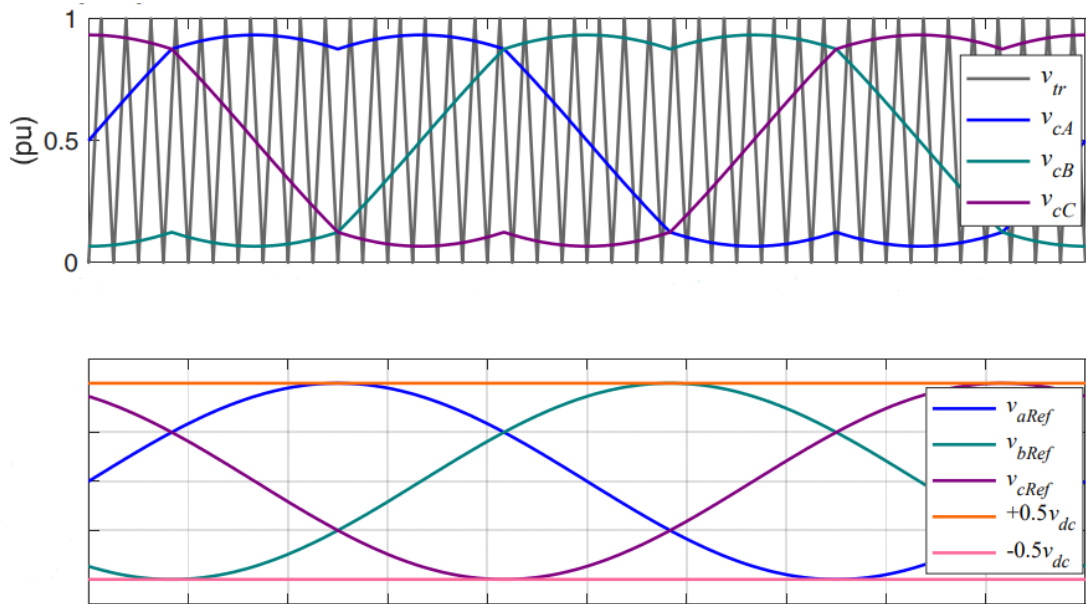


Figure 2. 21: SVM duty cycles with $m=1$ [20]

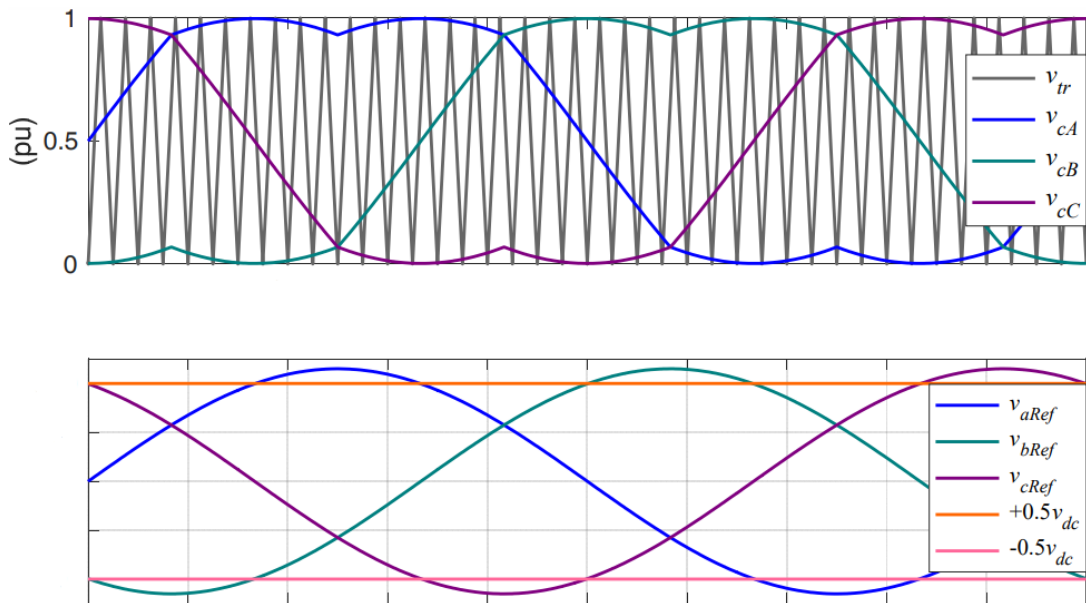


Figure 2. 22: SVM duty cycles with $m=1.15$ [20]

In the first figure, with a modulation index equal to unity, the duty cycles do not saturate, while, in the second the limit is reached, with $m = 1.15$. Therefore, the duty cycles saturate when $V_s = 1.15 \cdot v_{dc}/2$: the inverter linear region is extended by 15.4 % with respect to standard sinusoidal PWM [20]. The limit of linear modulation with SVM strategy corresponds to the circle inside the hexagon of radius $V_{dc}/\sqrt{3}$.

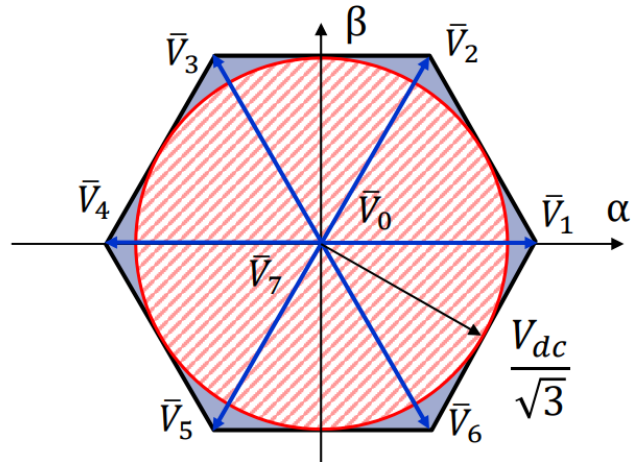


Figure 2. 23: SVM limit [20]

Finally, as previously mentioned, the injection of the third harmonic has no influence on the phase voltages of the load (fig. 2.24).

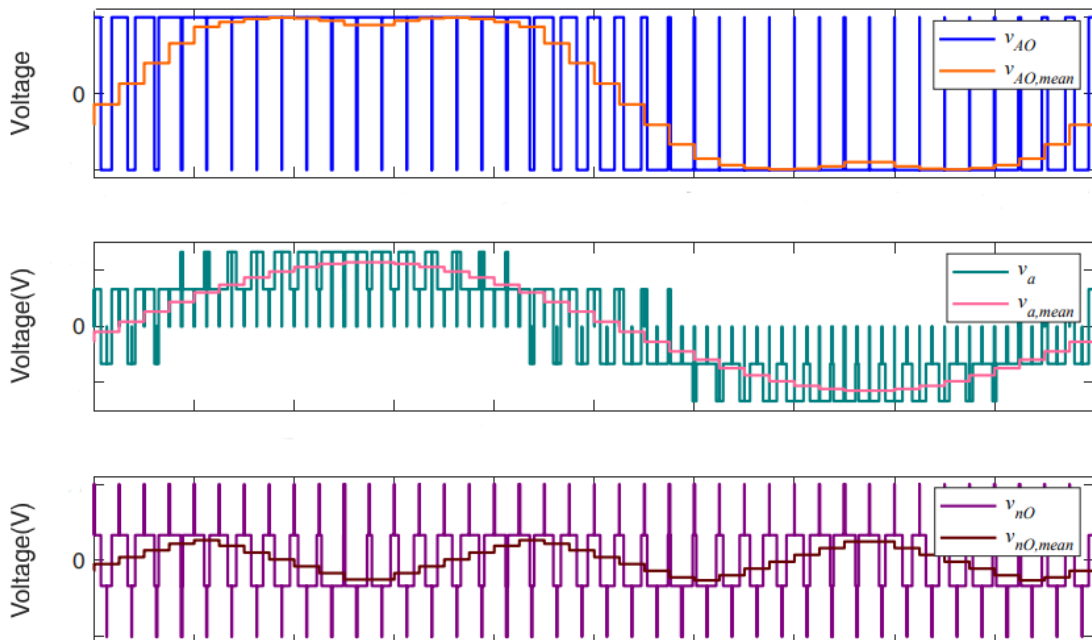


Figure 2. 24: SVM third harmonic influence [20]

The third harmonic is injected in the mobile mean value of the common mode voltage v_{n0} ; the phase voltage v_a does not have it.

2.3. Rotor flux position

Knowledge of the rotor flux position is one of the most important features of the FOC. The measure of the rotor flux position is different considering synchronous or asynchronous motors: for what concern the synchronous machines, the rotor speed is equal to the rotor flux speed. Therefore, the rotor flux position θ can be directly obtained by position sensor or by integration of rotor speed. The rotor position is required for variable transformation from stationary reference frame to synchronously rotating reference frame i.e., the Park transformation [15]. Thus, the key module of this control system is the information of the rotor position either from sensorless estimators or from Hall sensor.

2.3.1. Sensorless estimators

Either sliding mode observer (SMO) or flux observer are used to estimate the position feedback for field-oriented control algorithm.

Sliding mode observer

The sliding mode observer module generates a sliding motion on the error between the measured and estimated position. Doing so, it produces an estimated value that is closely proportional to the measured position. The block accepts stator voltages v_α and v_β , together with currents i_α and i_β as inputs and estimates the electromotive force of the machine model; then, by means of the EMF it further generates the observed rotor position and speed [21]. In particular, it uses per unit voltage and current values in the stationary (α, β) reference frame.

The following equations describe the computation of the electrical position and mechanical speed [22] [23] [24]:

$$\frac{di_{\alpha\beta}}{dt} = \phi i_{\alpha\beta} + \Gamma v_{\alpha\beta} - \Gamma e_{\alpha\beta} \quad (2.29)$$

where

$$e_{\alpha\beta} = \begin{bmatrix} -\lambda_m \omega \sin \theta \\ \lambda_m \omega \cos \theta \end{bmatrix} \quad (2.30)$$

$$\boldsymbol{\phi} = \begin{bmatrix} -\frac{R_s}{L_s} & 0 \\ 0 & -\frac{R_s}{L_s} \end{bmatrix} \quad (2.31)$$

$$\boldsymbol{\Gamma} = \begin{bmatrix} \frac{1}{L_s} & 0 \\ 0 & \frac{1}{L_s} \end{bmatrix} \quad (2.32)$$

The discrete-time sliding mode observer operations, by using per-unit values, are:

$$\hat{i}_{\alpha\beta(k+1)} = \mathbf{A}\hat{i}_{\alpha\beta(k)} + \frac{v_{rated}}{i_{rated}}\mathbf{B}(v_{\alpha\beta(k)} - \theta_{\alpha\beta(k)}) \quad (2.33)$$

$$\theta_{\alpha\beta(k+1)} = \theta_{\alpha\beta(k)} + 2\pi f_0 \times \left(\mathbf{Z}(i_{rated}(\hat{i}_{\alpha\beta(k)} - i_{\alpha\beta(k)})) - \theta_{\alpha\beta(k)} \right) \quad (2.34)$$

with

$$\mathbf{A} = e^{\boldsymbol{\phi}T_s} \quad (2.35)$$

$$\mathbf{B} = \int_0^{T_s} e^{\boldsymbol{\phi}\tau} d\tau \quad (2.36)$$

$$f_0 = \frac{F_0}{f_s} \quad (2.37)$$

being k the sample count, v_{rated} and i_{rated} the nominal voltage and current corresponding to 1 per-unit, \mathbf{Z} the attraction function (fig. 2.25), F_0 the cut-off frequency of the filter in cycles per sample, F_0 the cut-off frequency in cycles per second and $\theta_{\alpha\beta(k)}$ the estimated BEMF.

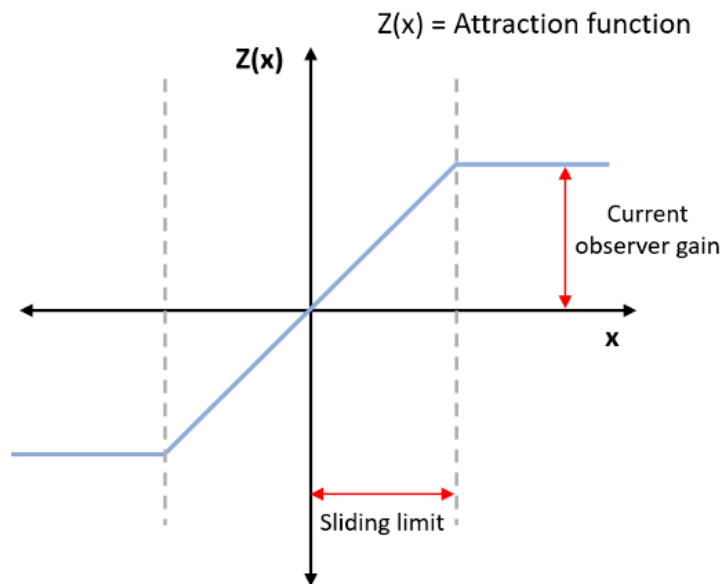


Figure 2. 25: SMO attraction function [22]

The current observer gain and sliding surface limit can be tuned: to improve stability, it is possible either to increase the sliding surface limit or lower the current observer gain; to reduce distortion, the current observer gain should be decreased or the sliding surface limit increased.

Flux observer

The flux observer module uses the same inputs of SMO ($v_\alpha, v_\beta, i_\alpha, i_\beta$) to estimate the rotor position; in addition, it can also compute the magnetic flux and electrical torque of rotor. The following equations show how the block estimates these quantities for a PMSM [25] [26]:

$$\lambda_\alpha = \int (v_\alpha - i_\alpha R_s) dt - (L_s \cdot i_\alpha) \quad (2.38)$$

$$\lambda_\beta = \int (v_\beta - i_\beta R_s) dt - (L_s \cdot i_\beta) \quad (2.39)$$

$$\lambda = \sqrt{\lambda_\alpha^2 + \lambda_\beta^2} \quad (2.40)$$

$$T = \frac{3}{2} p (\lambda_\alpha i_\beta - \lambda_\beta i_\alpha) \quad (2.41)$$

$$\theta = \tan^{-1} \frac{\lambda_\beta}{\lambda_\alpha} \quad (2.42)$$

2.3.2. Analog Hall sensor

In the following sub-section is introduced the solution chosen in this project to estimate the rotor position through analog Hall sensors.

Motor control by means of Hall sensors presents several advantages. In general, sensorless control methods produce acoustic noise and suffer secondary saliency and cross-saturation problems; the cross-saturation effects generate load-dependent position offset, while the secondary saliency that originated from the different spatial harmonics creates the periodical estimation errors [27]. Moreover, the use of Hall sensors does not require a mechanical coupling and is low-cost. Differently from sensorless estimators, the sensed method is able to work even at low velocities and permits a dynamical functioning like proper of the suspension project application. In particular, linear Hall sensors yield to a

better resolution than the discrete ones. However, their signals are usually contaminated by many uncertainties:

- Variations in the magnetization of the magnets.
- Positional variation in the Hall sensor mounting.
- Interference from the stator magnetic field.
- Air-gap field variations due to temperature changes.

Clearly, all these effects aggravate the rotor angle estimation accuracy but, with proper filtering it is possible to make an efficient overall system.

Analog Hall effect sensors generate a voltage output that is proportional to the applied magnetic field: they generally feature a quiescent voltage output of 50% of the supply voltage. They are devices with high accuracy in conjunction with small package size: they usually are temperature-stable components available in a miniature surface mount package and ultra-mini through-hole single in-line package. The characteristic of these linear devices make them ideal for use in automotive applications, operating through an extended temperature range (-40°C to 150°C). As regard as its functioning, when the supply is ramped to its operating voltage, the sensor output takes a finite time to react to an input magnetic field: power-on time is defined as the time it requires for the output voltage to begin responding to an applied magnetic field after the power supply has reached its minimum specified operating voltage, $V_{CC}(\text{min.})$ (fig. 2.26) [28].

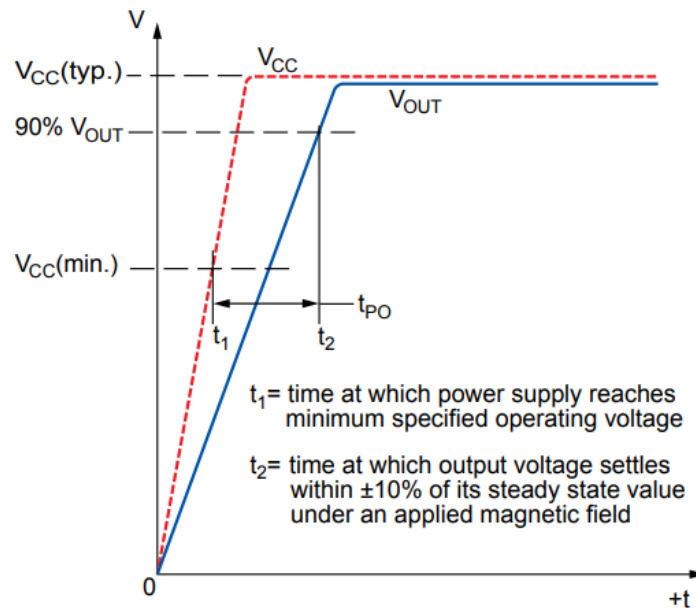


Figure 2. 26: Hall sensor output characteristic [28]

When there is no significant magnetic field, in the quiescent state, the output set to a ratio of the supply voltage. For what concern device sensitivity, the presence of a south-polarity magnetic field perpendicular to the branded surface of the package increases the output voltage from its quiescent value toward the supply voltage rail; the quantity of output voltage increase is proportional to the amplitude of the magnetic field applied. On contrary, the application of a north polarity field lower the output voltage from its quiescent value. This proportionality is named magnetic sensitivity, it is defined as:

$$Sens = \frac{V_{OUT(B+)} - V_{out(B-)}}{B(+)-B(-)} \quad (2.43)$$

where $B(+)$ and $B(-)$ are two magnetic fields with opposite polarities [28].

The solution utilized in this work to estimate rotor position from the voltage output of the linear Hall effect sensors consists of a lookup table whose output is the electrical angle i.e., rotor position. This is properly calibrated through the motor electrical angle mapping from the Hall sensors voltage waveforms.

Finally, experimental results demonstrate better reliability in the low-speed region than the sensorless algorithms. Furthermore, it brings the advantages of easy installation and less stator current distortion i.e., robustness with respect to the armature reaction. Additionally, it does not show any problem in speed reversal [27].

3. Design and simulation

In this chapter, the first phases of the motor control implementation are presented. Therefore, it deals with the requirements and functional analysis of the system, the design and calibration of the algorithm by means of numerical modelling and, finally, numerical validation of the control through simulation. These steps have been made in MATLAB/Simulink environment, especially, with the use of Motor control blockset toolbox. In addition to that, in the following sections the control is applied to two different electric motors. The first motor is the one utilized for the rotary regenerative suspension project i.e., the one in which the thesis gives its contribution. In particular, it is a synchronous motor and is the same for both damper solutions presented in section 1.2: the hydraulic shock absorber, named ‘EHA’, and the electro-mechanical one, called ‘RRSA’; in the last chapter it is shown the prototyping and implementation of the algorithm on this machine. Instead, the second application regards a flux map based motor model and is for simulation scope only.

3.1. Control algorithm overview

The overall control strategy chosen for the project is presented in section 1.3; figure 3.1 depicts the system-level block diagram for field-weakening control of a PMSM. The block diagram shows the field-oriented control architecture combined with FWC algorithm. They includes the following components:

- Current controller composed of two proportional-integral regulators.
- MTPA and field-weakening current reference generator.
- Clarke, Park and inverse Park transforms to convert between stationary and rotating synchronous frames.
- Space vector generator module to transform v_α and v_β commands into pulse-width modulation signals applied to stator windings.
- Protection and auxiliary functions.
- Sensors or observer to estimate rotor angular position.

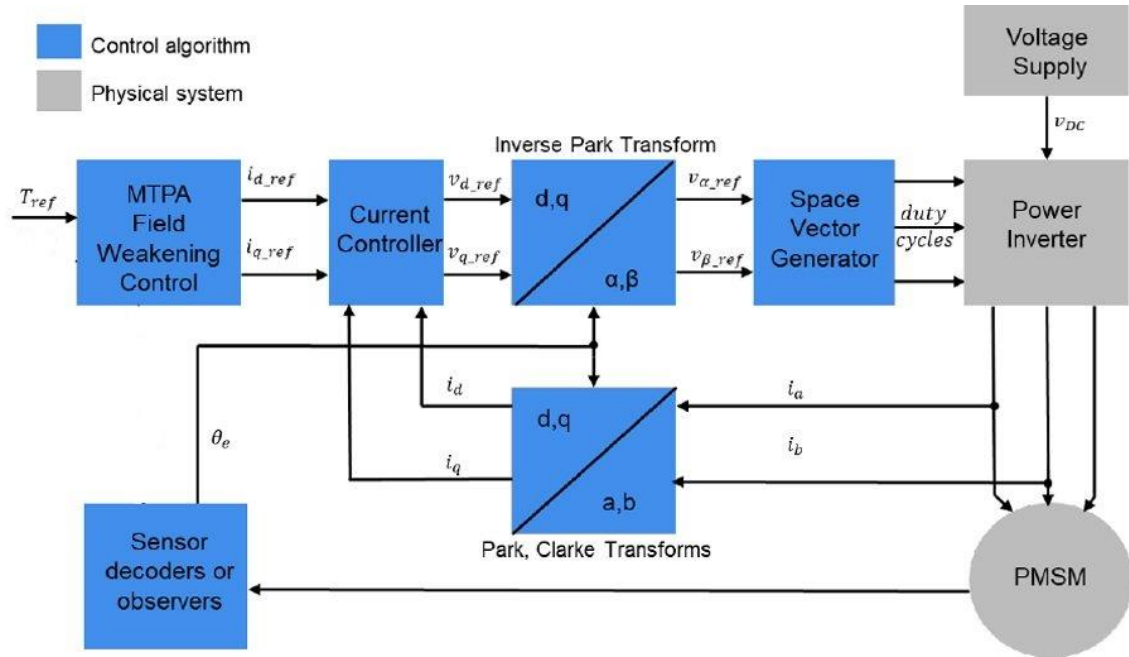


Figure 3. 1: Control algorithm overview [29]

The steps needed to design the control algorithm are the following [30]:

- Develop controller architecture with two PI regulators for the current loop.
- Tune the gains of the PI controllers to reach performance requirements.
- Design a space vector modulator for managing of PWM.
- Design an observer algorithm to estimate rotor position in case of sensorless control.
- Implement the sensors needed to measure rotor position if sensed control is used.
- Design maximum torque per Ampere and field weakening control strategies to generate optimal d and q-axis current references.
- Implement computationally efficient Park, Clarke and inverse Park transforms.
- Design fault detection and protection logic.
- Validate the controller performance in different working points.
- Implement the controller on a microcontroller for connections to the power stage.

3.2. RRSA and EHA

3.2.1. Functional specifications

The control algorithm is intended to drive an electric motor integrated in a regenerative automotive suspension. The contribution of this work is to provide the design and implementation of the control strategy to manage the torque and current of the machine positioned in the final stage of RRSA and EHA projects. The aforementioned electric motor is the same for both technologies: it is a 3-phase permanent magnet synchronous motor, with surface mounted PMs (fig.3.2).

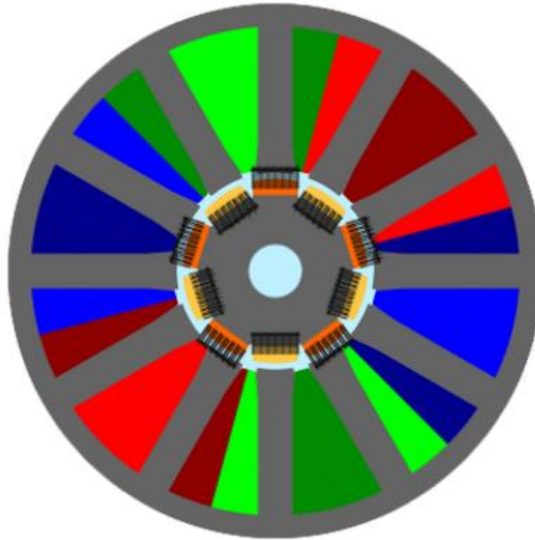


Figure 3. 2: SPM motor cross-section view

The parameters of the machine are listed in the following table:

Table 3. 1: Electric machine parameters

Description	Symbol	Value
Number of pole pairs	p	5
Phase resistance	R_s	68 m Ω
Synchronous inductance	L_s	350 μ H
Permanent magnet flux linkage	λ_m	6.64 mWb
DC-link voltage	v_{dc}	48 V
Maximum RMS current	$i_{\max(RMS)}$	40 A

In addition to that, the switching frequency of the power stage connected to the motor is $f_s = 20$ kHz, while the maximum voltage is $v_{max} = 27.71$ V (eqn. 2.16).

By means of these values other important variables have been computed, permitting to understand what are the main motor working points. The maximum phase current that can be driven by the motor is:

$$i_{max} = i_{max(RMS)}\sqrt{2} = 56.57 \text{ A} \quad (3.1)$$

The machine torque constant is calculated as:

$$k_t = \frac{3}{2}p\lambda_m = 0.0498 \frac{\text{N}}{\text{A}} \quad (3.2)$$

Thus, the maximum torque which can be requested to the motor is:

$$T_{max} = i_{max}k_t = 2.82 \text{ Nm} \quad (3.3)$$

This torque value, defines the torque constant region, it can be obtained till the base speed which is:

$$\omega_b = \frac{v_{max}}{p\sqrt{(L_s i_{max})^2 + \lambda_m^2}} = 265.41 \frac{\text{rad}}{\text{s}} \cong 2534 \text{ rpm} \quad (3.4)$$

Moreover, the maximum speed that can be reached by the motor and fed by the inverter is:

$$\omega_{max} = \frac{f_s \cdot 60}{p \cdot 20} = 12000 \text{ rpm} \cong 1256 \frac{\text{rad}}{\text{s}} \quad (3.5)$$

The latter value is calculated considering a frequency modulation index $m_f = f_s/f_o$ of 20 with f_o the output frequency. Finally, the machine characteristic current I_0 has been computed (eqn. 2.19): it is equal to 18.97 A.

3.2.2. Control algorithm design

The steps taken to design the motor control algorithm are presented in the following subsection. The design, tuning and numerical validation of the control strategy have been made in Simulink, in particular, through the use of Motor control blockset toolbox. It provides the development of multirate simulations to detect and correct errors across the complete operating range of the motor before proceeding with hardware testing. Thus, this method permits to reduce the amount of prototype testing and verify the robustness of the control algorithm to fault conditions.

MTPA control reference

The first module designed is the MTPA control reference (fig. 3.3). It computes the d-axis and q-axis current reference values according to equations 2.7. The obtained signal values

result in efficient output for the SPM motor in the constant torque region; successively, these references are interfaced with the FWC output.

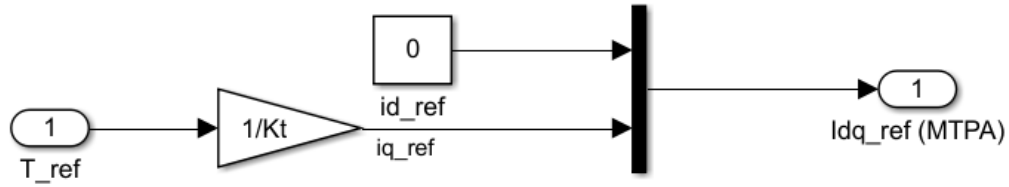


Figure 3. 3: MTPA control reference

Basically, this block converts the input torque reference in the corresponding q-axis current while setting the d-axis current to zero. Moreover, its execution sample time is equal to 0.005 s. It is important to highlight that all the following control modules that are presented in the next lines are performed at the switching frequency rate to simulate the real microcontroller interrupt service routine i.e., with $T_s = 5.00e - 05$ s.

Sensorless estimators

Proceeding, the other inputs of the current controller have been processed i.e., the feedback signals. Sensorless control has been chosen for this simulation, thus, either the sliding mode observer or the flux observer are used to estimate the rotor position, as presented in section 2.3.

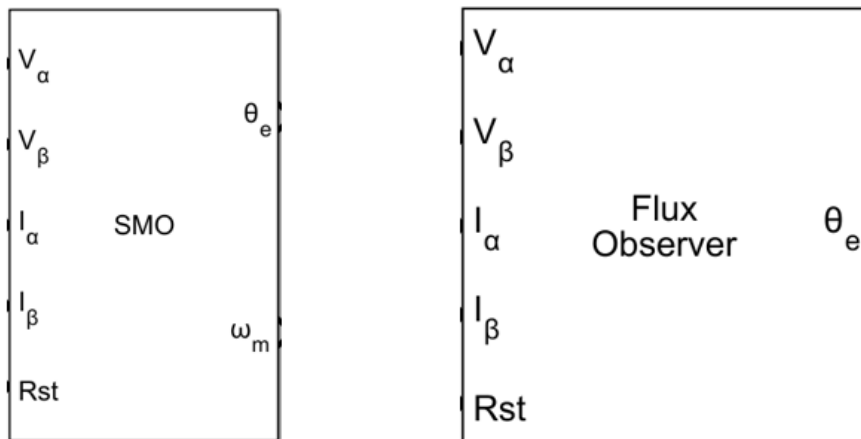


Figure 3. 4: Sensorless estimators

The SMO is tuned with a current observer gain equal to 0.01 and a unity sliding surface limit; it outputs the electrical angle in rad and the mechanical speed in rad/s, instead the flux observer only the electrical angle. They both accept as input the per-unit value of

voltage and current, coming internally from the control, using as reference value for the conversion respectively v_{mx} and i_{max} . These signals are properly processed by a unit delay and a DC component removal module (fig. 3.5). The latter is inserted to cancel the offset introduced by the observer’s errors. In particular, it is composed by an infinite impulse response filter which modifies the signal with a discrete low pass filter using the following equation:

$$y(k) = a \times x_k + (1 - a) \times y_{k-1} \quad (3.6)$$

where a is the filter coefficient, y is the filtered output value and x is the sampled input value. The theoretical cutoff frequency is computed as:

$$f_c = \frac{a}{(1 - a) \cdot 2\pi \cdot T_s} \quad (3.7)$$

Therefore, a lower filter coefficient gives better filtering at the cost of increasing the delay in the response time; in this case, the filter coefficient is set to 0.005.

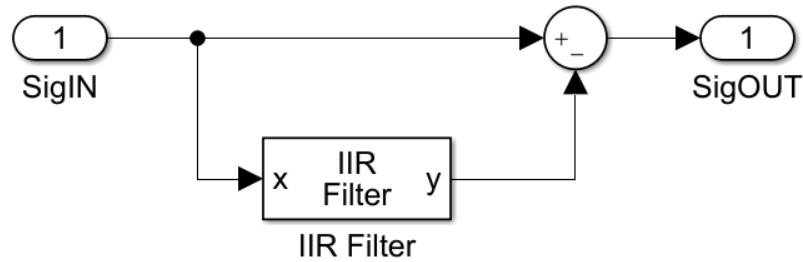


Figure 3. 5: DC component removal

Clarke and Park transforms

Clarke and Park transforms are needed to translate i_a and i_b phase current measurements from the motor model in the d and q-axis current feedbacks.

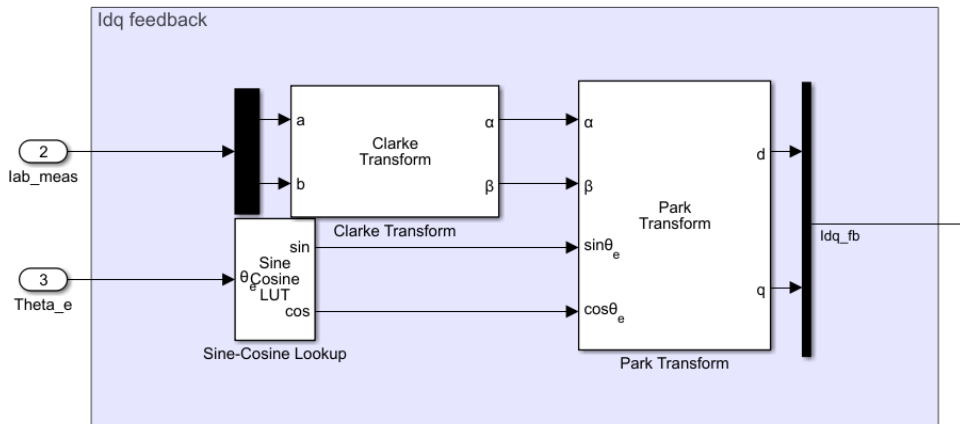


Figure 3. 6: Phase current feedback

Current controller

Figure 3.7 shows the current controller block scheme.

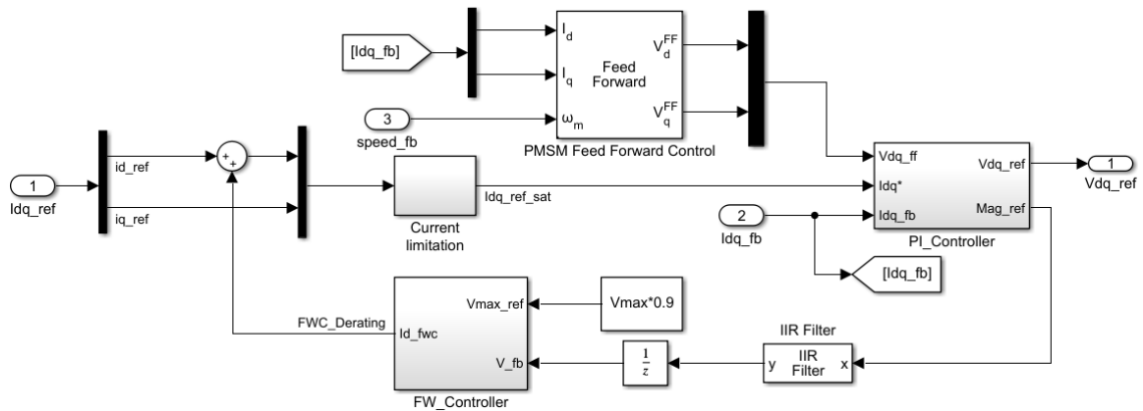


Figure 3. 7: Current controller block scheme

The inputs are the currents i_{dq_ref} and the speed feedback that in this simulation is simply the reference speed imposed to the motor; the outputs are the v_{dq_ref} voltages.

Before entering in the PI regulators, the current references are modified by means of the flux-weakening controller contribution and the current saturation. The FWC (fig. 3.8) accepts as input the maximum voltage reference and the magnitude of the v_{dq_ref} voltage imposed by the PI controllers. This last variable is first processed through a IIR filter, with coefficient 0.01, and a unit delay.

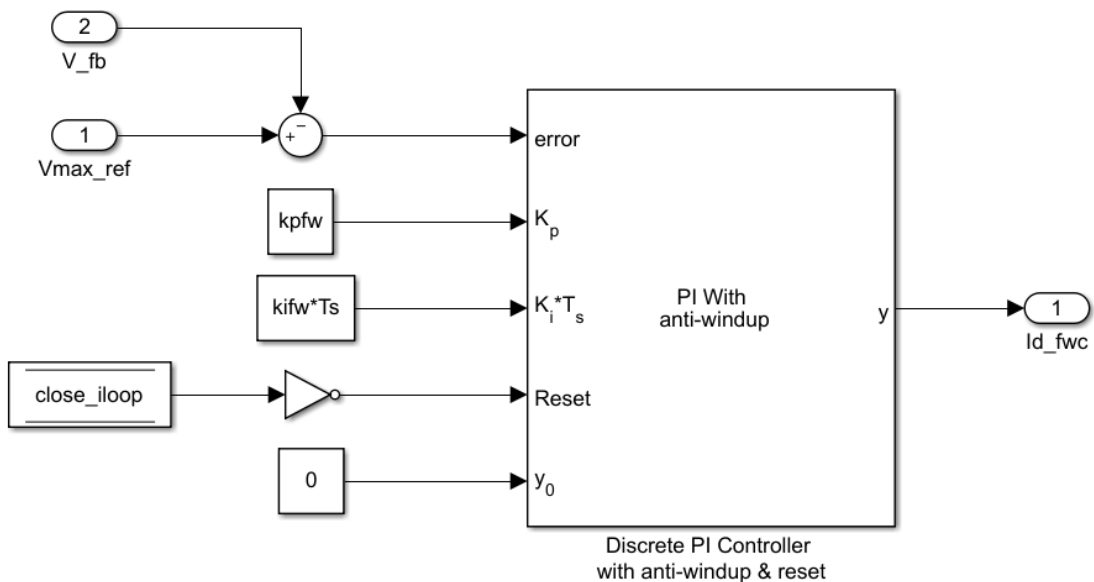


Figure 3. 8: Flux-weakening controller

The FWC is designed to have the same behaviour shown in sub-section 2.1.2. It features a discrete PI regulator and anti-windup calibrated with:

- Proportional gain $k_{p_{fw}} = 12.5 \text{ A/V}$.
- Integral gain $k_{i_{fw}} = 0.06 \text{ A/Vs}$.
- Saturation limit $[0, -i_{max}]$.

Therefore, if increasing the speed of the motor the magnitude of the v_{dq_ref} exceeds its maximum value, set to $0.9 \cdot v_{max}$, a negative i_d current is imposed to the drive, to maintain this reference. This means that the base speed is reduced with respect to its standard value reached at v_{mx} , but the motor can still adequately run with a higher speed properly reducing the flux. In particular, for this machine $I_0 < i_{max}$, thus, the current protection module is designed as in figure 3.9 to complete the work of the FWC.

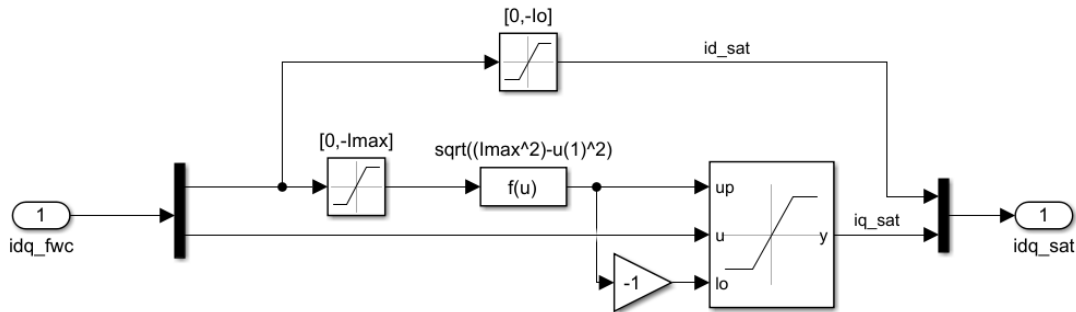


Figure 3. 9: Current limitation

The overall strategy and the behaviour of the current space vector are the one illustrated in figure 2.14.

Once obtained the final current reference values, these fed the PI current regulator in figure 3.10; only one is needed since the machine is isotropic, so the inductance is the same for d and q axis.

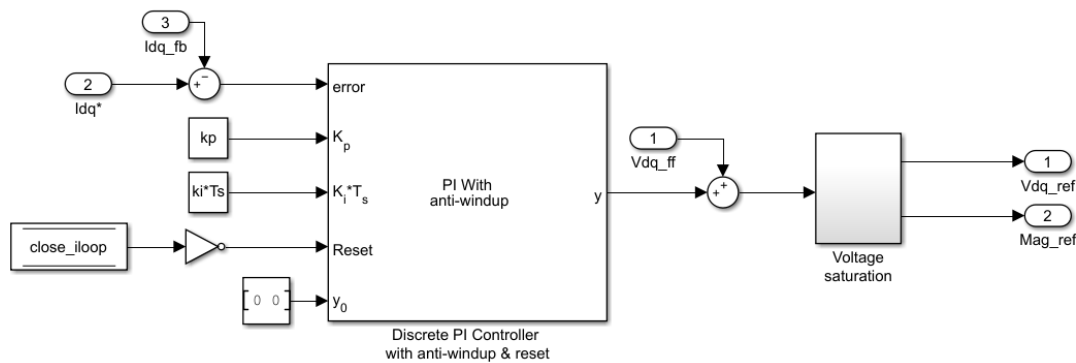


Figure 3. 10: PI current regulator

The i_{dq_ref} currents are compared with the feedback currents and depending on the error the voltage references are chosen, with a maximum absolute value equal to v_{max} . The calibration has been made according to the equations 2.14:

- Current control bandwidth $\omega_c = 1000 \cdot 2\pi = 6283$ rad/s.
- Proportional gain $k_p = 2.2$ V/A.
- Integral gain $k_i = 427.2$ V/As.

Figure 3.11 and 3.12 shows basic frequency control analysis exclusively of the FOC current control system, without FWC, considering the SPM motor parameters in table 3.1.

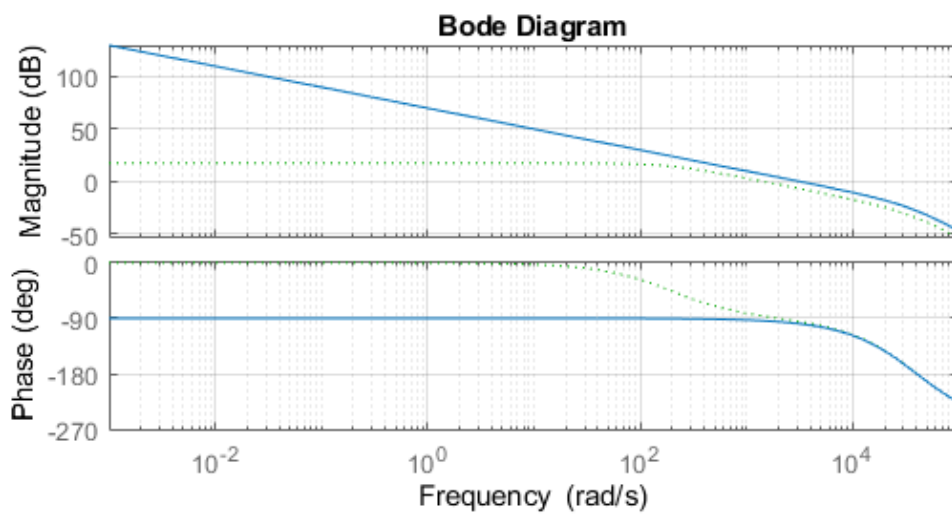


Figure 3. 11: Bode diagram

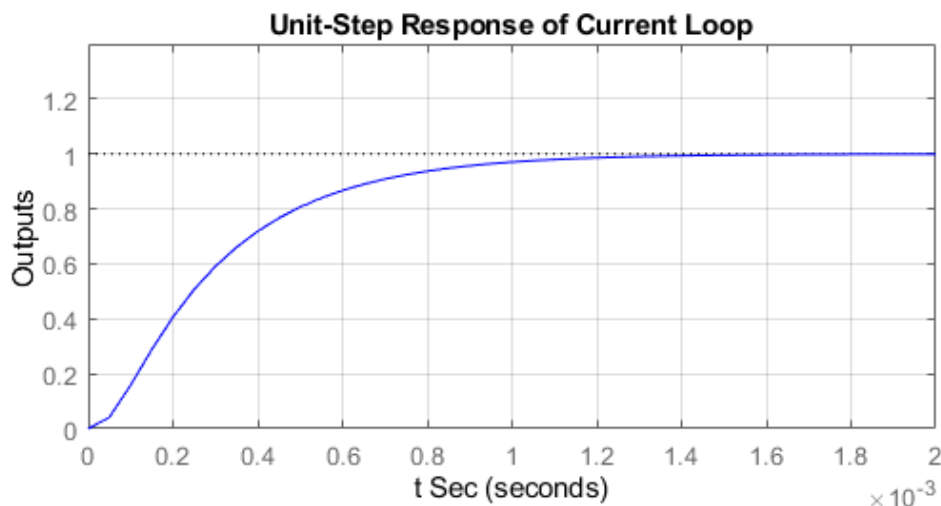


Figure 3. 12: Step response

The gain margin is equal to 28.3 dB while the phase margin is 81.2°.

Successively, the feed-forward of the motional terms is added to decouple the d and q-axis control. Finally, the resultant voltages pass through the voltage saturation module below that implements the equations 2.16.

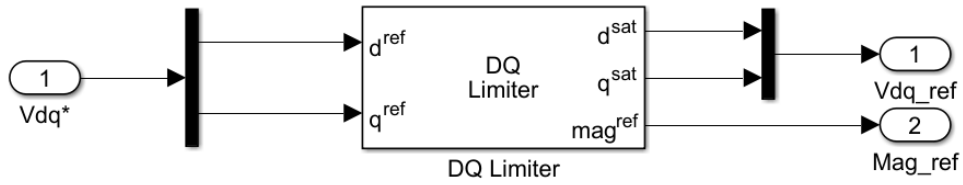


Figure 3. 13: Voltage saturation

Space vector generator

The last module before the physical system model is the space vector generator.

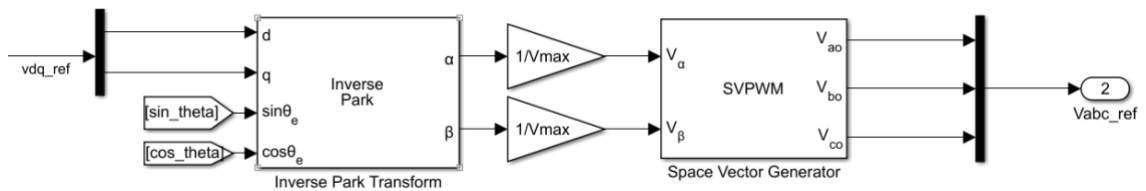


Figure 3. 14: Space vector modulation

Firstly, the d and q-axis voltage references are transformed through the inverse Park transform and converted into per-unit values. Successively, they are sent to the space vector generator block which generates the space vector modulation signals, according to the SVM strategy illustrated in the section 2.2. The outputs are double hump signals between -1 and 1 , thus, they are properly rescaled and translated to obtain the final duty cycles to be sent to the inverter (fig. 3.15).

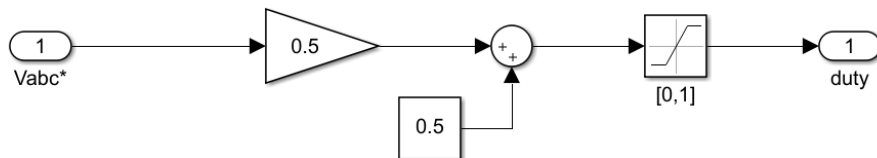


Figure 3. 15: Duty cycles conversion

3.2.3. Simulation

In this sub-section are presented the plant model utilized to test the control system and the related results.

Plant model

An accurate plant model is used to verify the functionality of the control algorithm and optimize the design.

Firstly, the 3-phase inverter has been implemented (fig. 3.16).

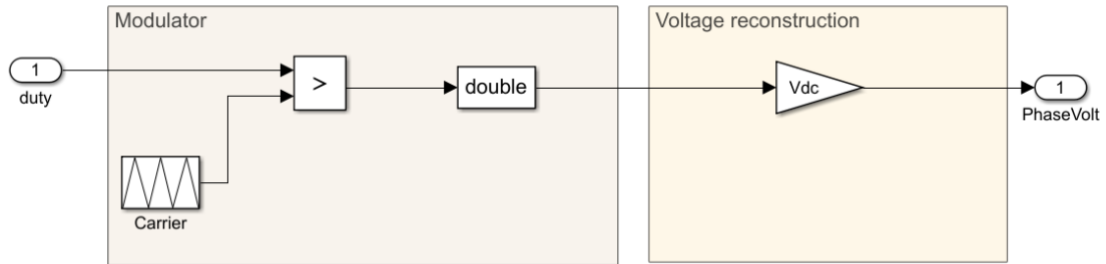


Figure 3. 16: 3-phase inverter

It is composed of the modulator and voltage reconstruction. The modulator compares the duty cycles coming from the control algorithm with a unipolar triangular carrier between 0 and 1, running at the switching frequency f_s . The output of the comparison is 1 if the duty signal is higher than the carrier, zero on contrary; then, through the voltage reconstruction, the phase voltages imposed to the motor are formed as pulses between 0 and v_{dc} . This model permits to simulate the switching effects of the power stage.

Secondly, the SPM synchronous motor dynamics is modelled through a ready to use block of the toolbox, which implements the equations shown in appendix A.2, together with the parameters in table 3.1. It is set to have the speed imposed by an external load and be controlled in torque, by means of the phase voltages. The block outputs several variables, both for feedback measurements or to plot and verify the control functionality.

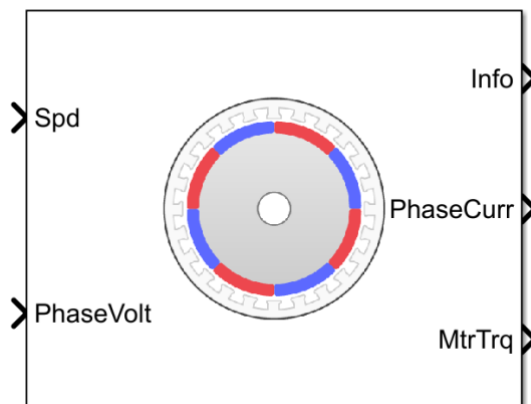


Figure 3. 17: Motor model

Finally, these signals are suitably affected by the control algorithm processing delays, as in the picture below.

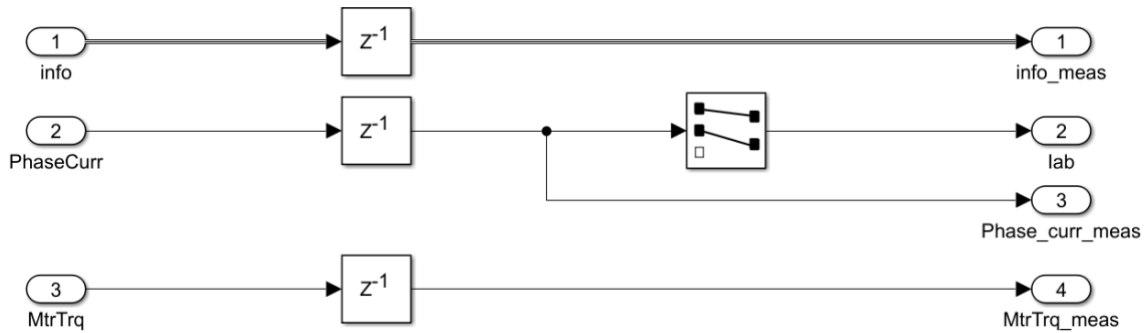


Figure 3. 18: Algorithm processing delays

In particular, it is simulated the PWM switching delay which is equal to half the switching time period in the worst case.

Test 1

Algorithm numerical validation has been performed controlling the presented plant model in several simulations, exploring different operating points of the machine, both in the constant torque region and over the base speed. During the tests, the control system has been tuned by iteration to find its final optimal calibration; at the end, the functionality and robustness of the design have been verified, accurately inspecting the main variable results. In the following lines, some simulation examples are shown to demonstrate the control system numerical validity. The inputs of the simulations are the mechanical speed, imposed externally to the motor, and the reference torque fed to the control algorithm; the flux observer is selected to estimate the rotor position.

In the first test, the motor is driven with an increasing speed and torque through steps till the base speed, where reached the maximum torque only the velocity is still enhanced. In figure 3.19 it is visible the behaviour of torque, speed and position variables. The speed range is from 0 to 6500 rpm, while the torque request is until 2.8 Nm. In the first region, before the base speed, the motor torque follows adequately its reference and is not affected by speed change; only at low velocities there is a small tracking error due to the observer offset. The base speed point is reached at around 4 s, with the maximum torque and a speed equal to 2400 rpm; the latter value is lower than the theoretical ω_b because of the FWC strategy that prevents the voltage to overstep the $0.9 \cdot v_{max}$ limit, giving to the system more stability and robustness. Above the base speed the machine is no more able to

follow the torque reference but the speed is still increased; in this region it is shown an optimal flux-weakening behaviour resulting in lower torque as the velocity is raised.

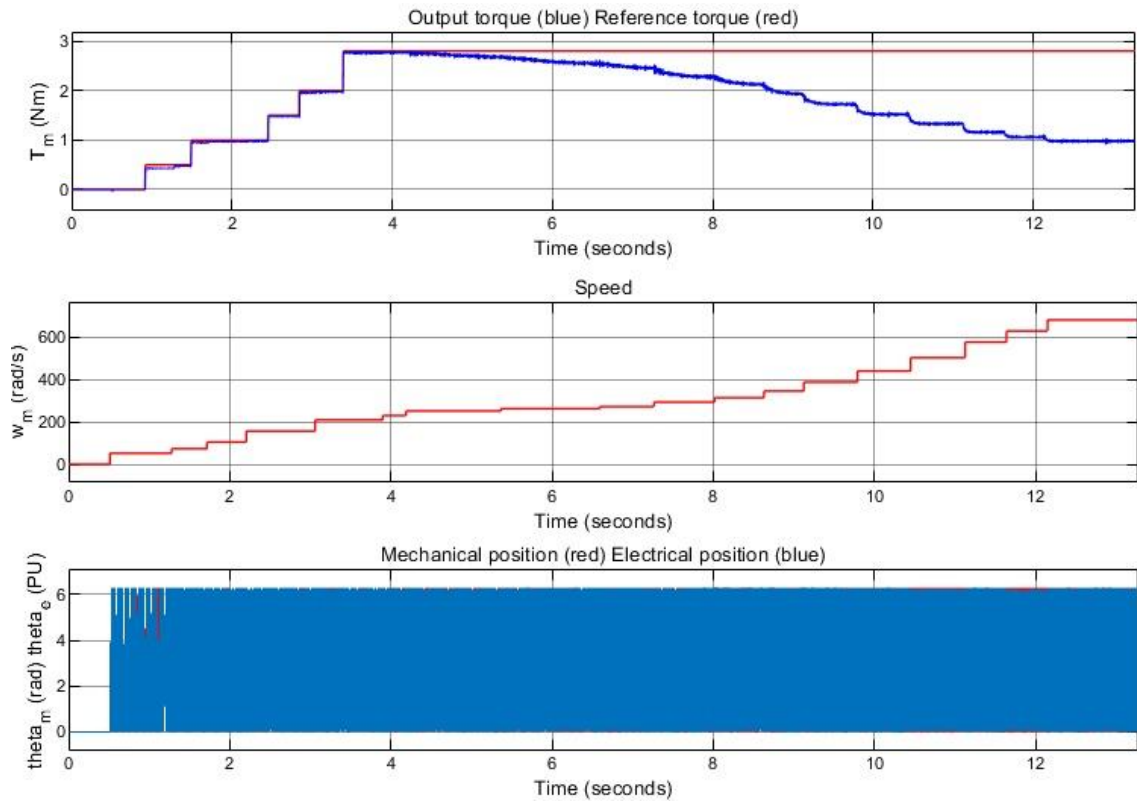


Figure 3. 19: Test 1, torque-speed-position

The FWC is more evident from the figure below, representing the current space vector.

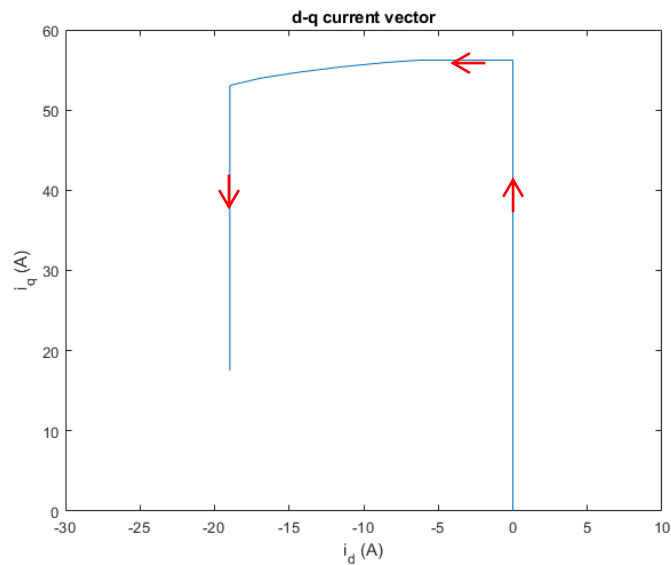


Figure 3. 20: Test 1, current space vector

The current vector follows the MTPA trajectory during the first part of the simulation; successively, the d-axis negative current is injected, firstly according to the maximum

current limit circle, then, reached the machine characteristic current, through the MTPV trajectory. In figure 3.21 the rotor electrical position estimation is presented, together with the mechanical position with 1/5 of the frequency due to the pole pairs; the angle seems to be optimally estimated.

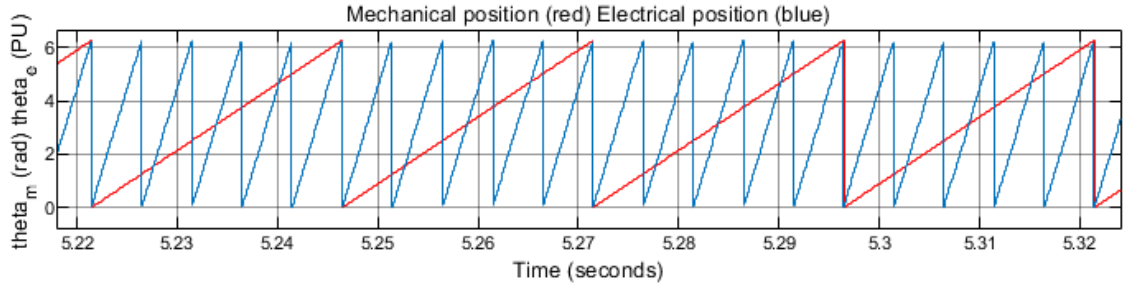


Figure 3. 21: Rotor mechanical and electrical angle

In the next picture, the electrical variables are shown, both in (a,b,c) and (d,q) reference frames.

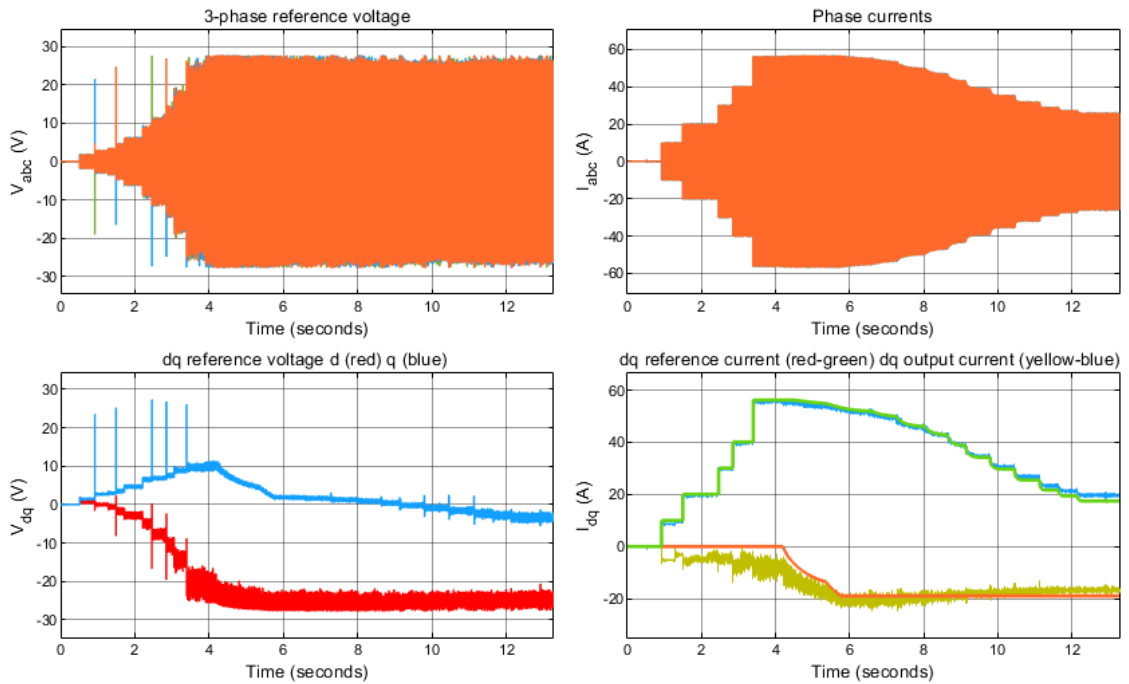


Figure 3. 22: Test 1, voltages and currents

The trend of the current follows the torque output. In particular, the q-axis current in the first region is proportional to the reference torque, while above the base speed depends on the flux-weakening. On contrary, the d-axis current reference below the base speed is null; however, it can be highlighted the offset error introduced by the observer. Then, in the FWC region negative d-axis current is imposed. As regards as the voltage, its trend is similar to the speed until the maximum voltage limit fixed by the FWC; at this point the

voltage amplitude is set to that bound. Successively, a highlight of the 3-phase voltages and current during flux-weakening is displayed, where it is visible the maximum voltage value and the sinusoidal current waveforms properly filtered by the plant inductance.

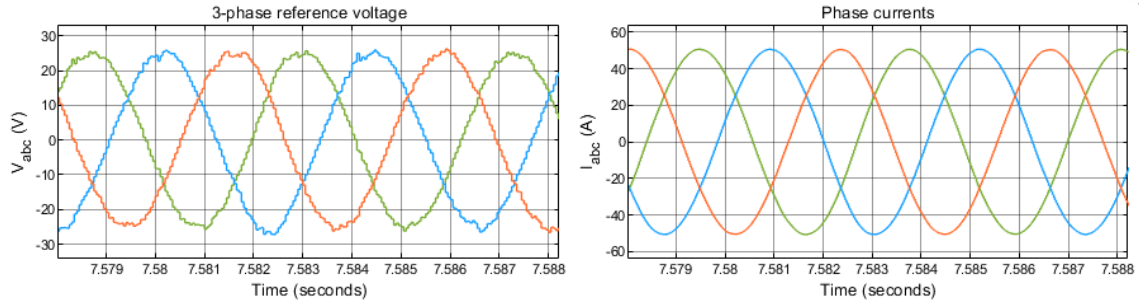


Figure 3. 23: Test 1, voltage and current highlight

Following, it is depicted the control system response time to a step change in the torque reference in the first region, and thus in the q-axis current reference.

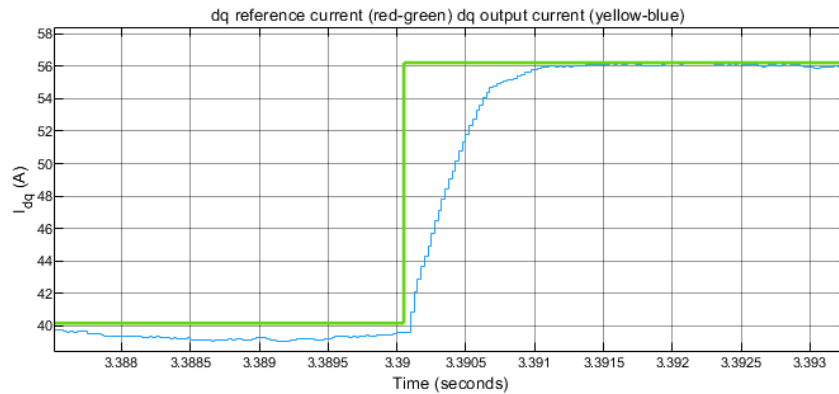


Figure 3. 24: Test 1, current step response

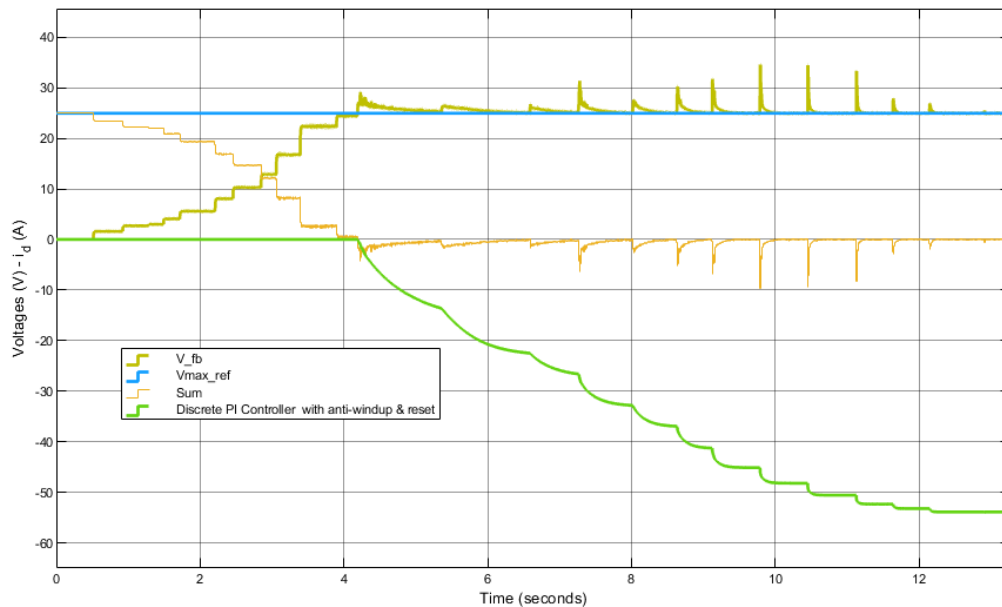


Figure 3. 25: Test 1, FWC

In figure 3.25, the FWC response is presented. It is active only if the amplitude of the voltage reference exceeds its maximum limit, in that case a negative d-axis current is provided. It is important to highlight that the response is here bounded at $-i_{max}$ value; then, it is the saturation block that imposes the proper trajectory, limiting it at the machine characteristic current. Finally, the next two plots show the duty cycles generated by the SVM, respectively during all the test time and a zoom in the field-weakening region.

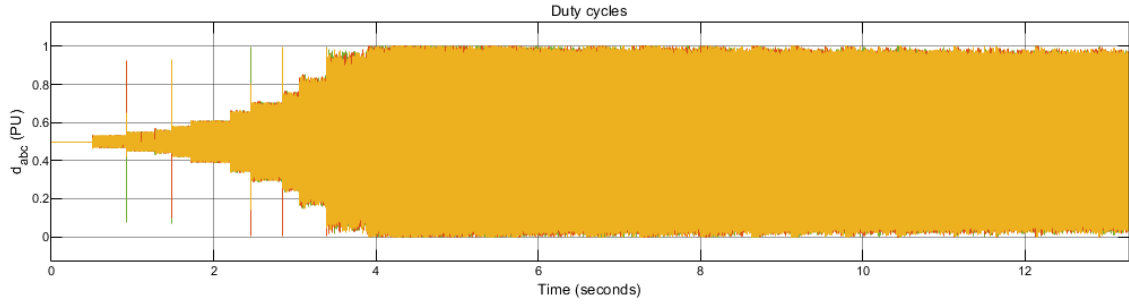


Figure 3.26: Test 1, duty cycles

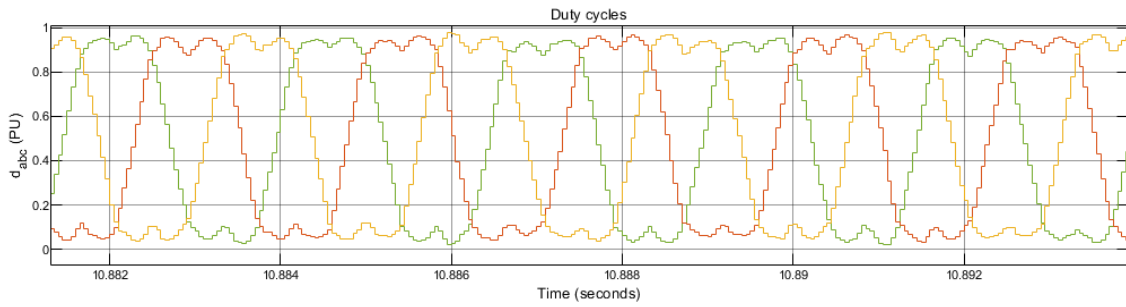


Figure 3.27: Test 1, duty cycles highlight

The double hump waveforms are correctly defined and they do not saturate.

Test 2

A second test was performed, in order to demonstrate the validity of the control system even in regenerative phase, when the motor speed is still increased through and external load by step and the torque reference is negative. The behaviour is analogous to the previous but reversed i.e., the q-axis current is negative and so also the current space vector.

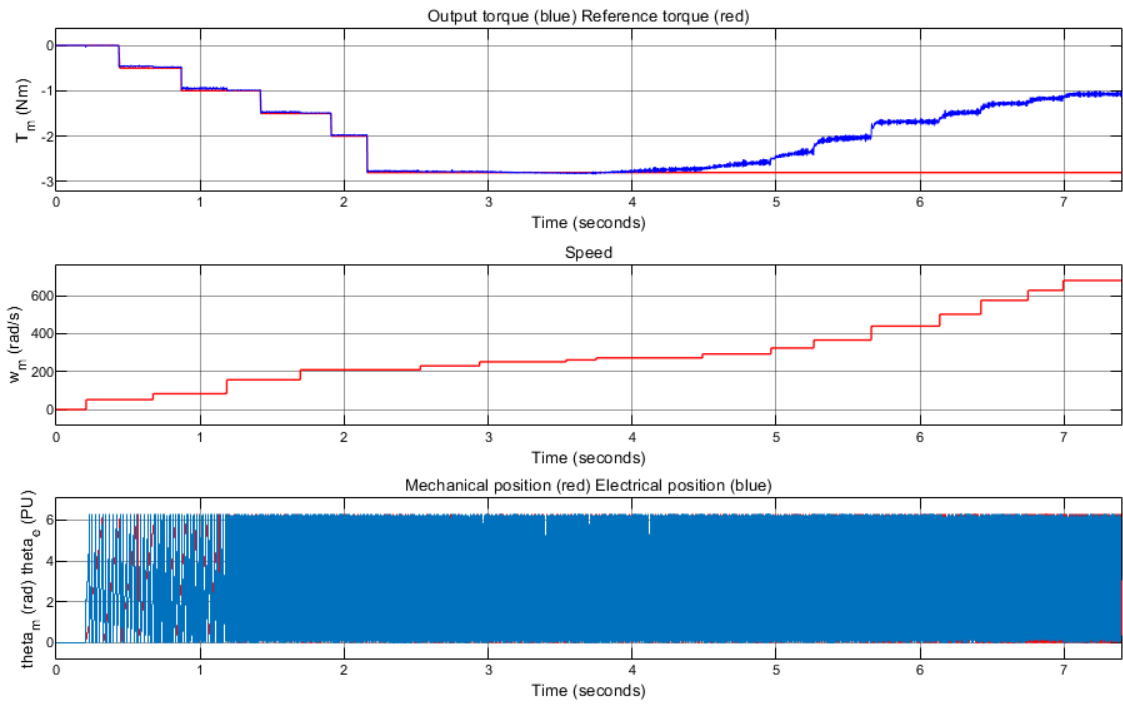


Figure 3. 28: Test 2, torque-speed-position

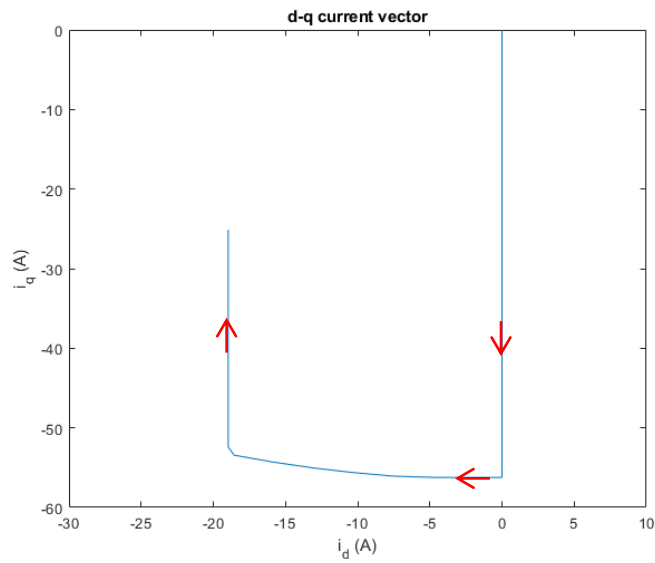


Figure 3. 29: Test 2, current space vector

Test 3

The following test verifies the functionality of the algorithm when alternate speed is imposed to the drive. This is the operating condition to which will be subjected the control system during the final stage of the suspension project i.e., a speed instantaneously alternating from positive to negative values, according to the shock absorber motion. Figures 3.30 and 3.31 depict respectively the mechanical and electrical variables trends.

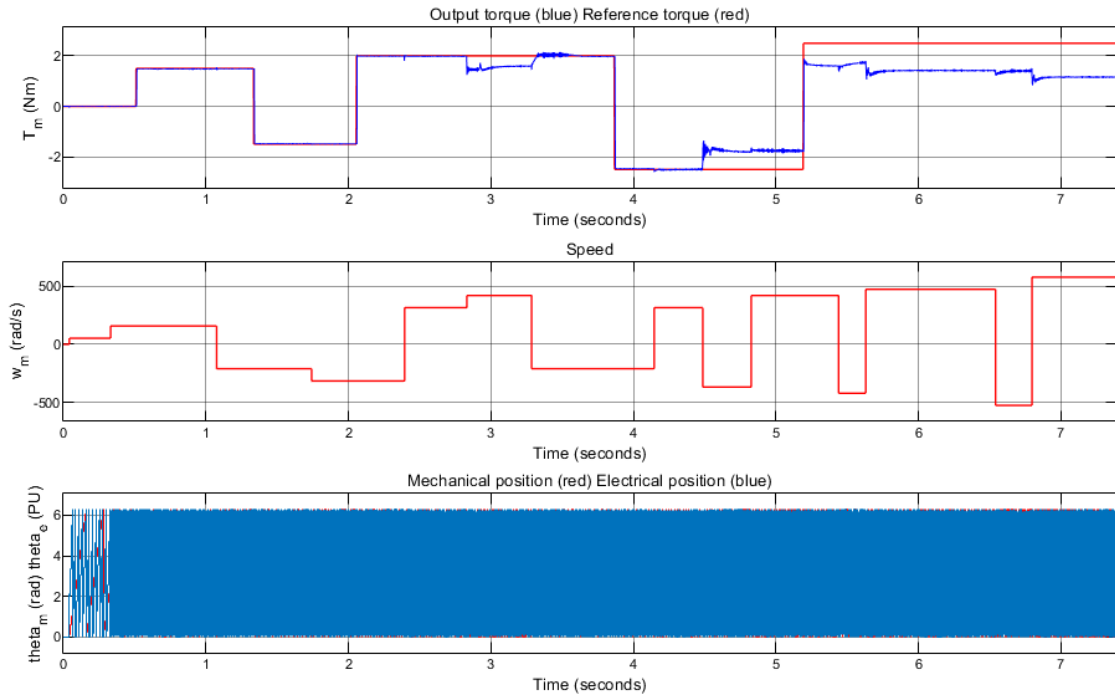


Figure 3.30: Test 3, torque-speed-position

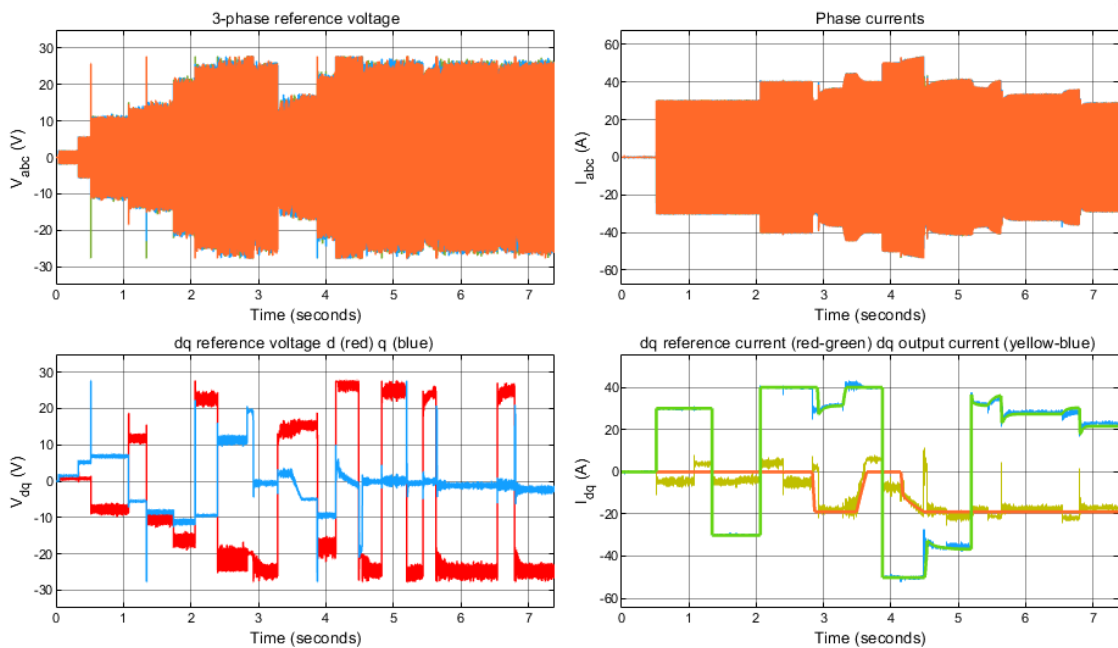


Figure 3.31: Test 3, voltages and currents

It can be concluded that this control system is fully numerical validated, since also in these operating conditions maintains stability and robustness, except for some normal spikes.

SMO test

A final simulation is illustrated in which the sliding mode observer has been selected to estimate rotor position. It presents some imperfections, thus, the flux observer solution is preferable for simulation phase.

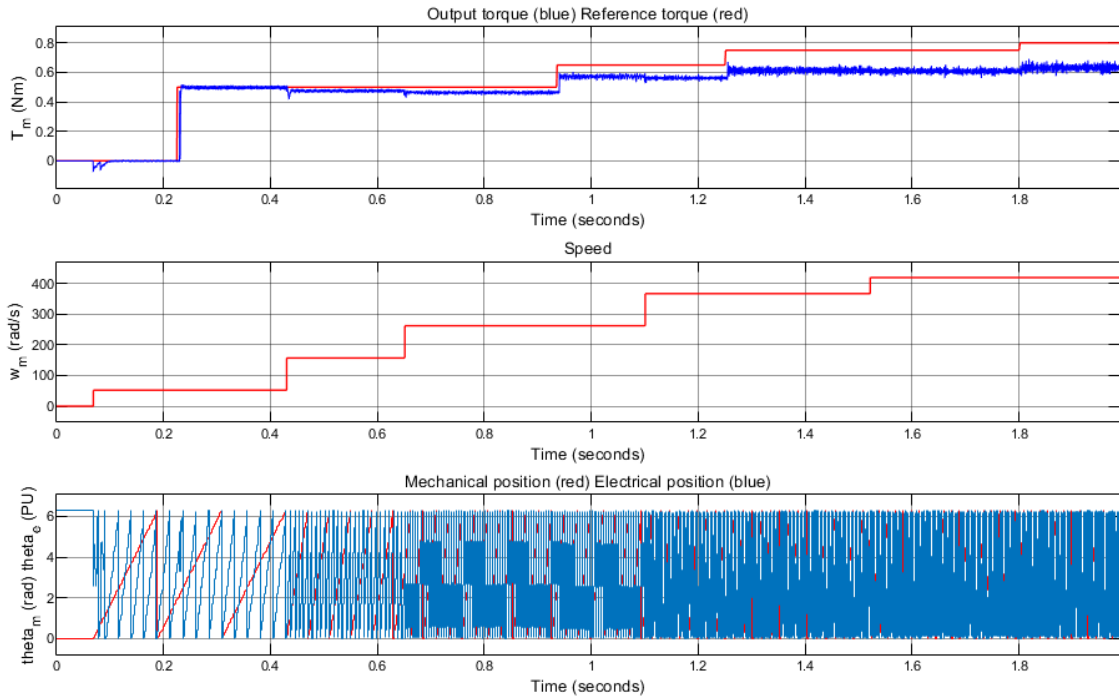


Figure 3.32: SMO test, torque-speed-position

In particular, it is less stable and robust than the flux observer; in fact, as in the figure, it maintains the control of the drive only for small torque references and for little step change. Moreover, the offset introduced is much more evident than the previous one.

3.3. Flux map based motor model

In the following section, it is presented the recalibration and application of the same control structure to a flux map based motor model. This has been done for simulation scope only, to demonstrate the flexibility of the designed algorithm to different motor parameters and also the influences of the magnetic saturation and iron losses on the results.

3.3.1. Calibration settings calculation

The new motor to control is a 3-phase PMSM with SPM. The model of this machine has been developed through the use of given flux maps, extracted from Flux-Motor; thus, also the parameters needed to calibrate the algorithm have been extrapolated by means of the following figures, describing the motor characteristics.

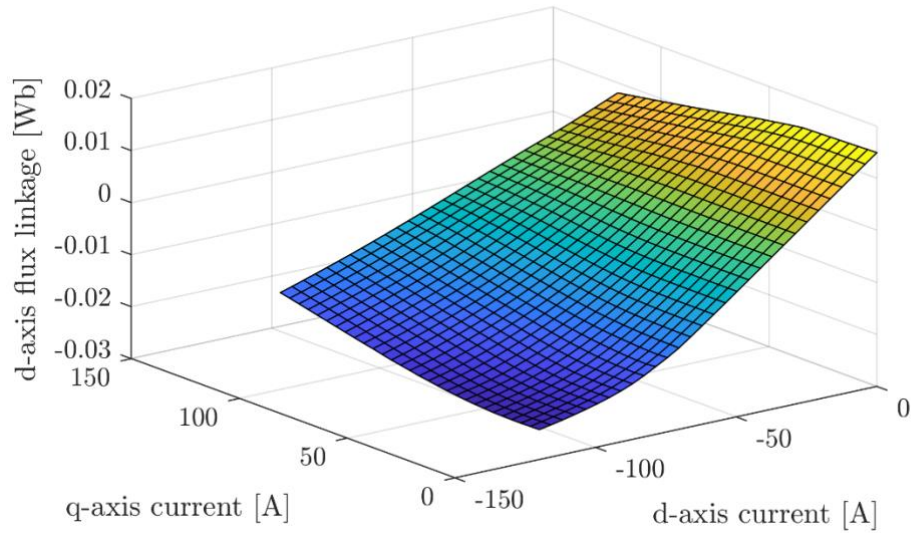


Figure 3. 33: d-axis flux map

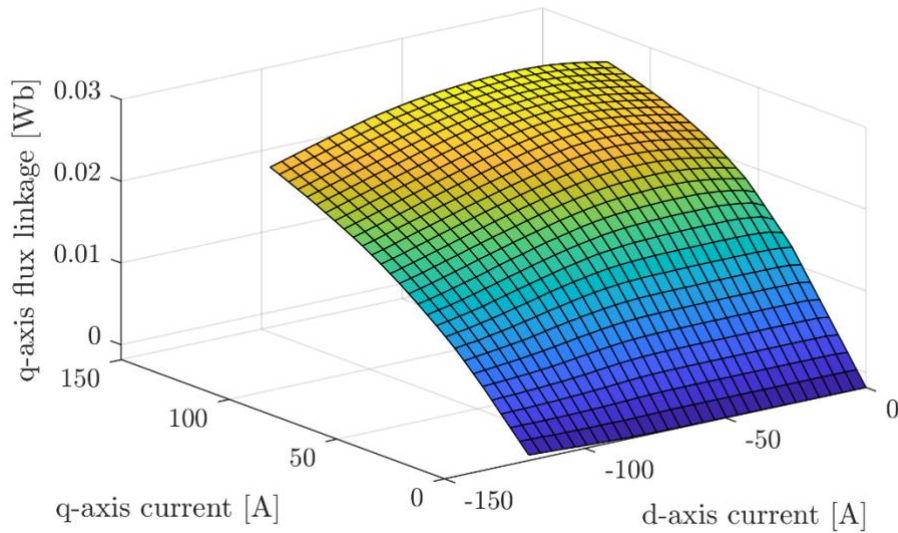


Figure 3. 34: q-axis flux map

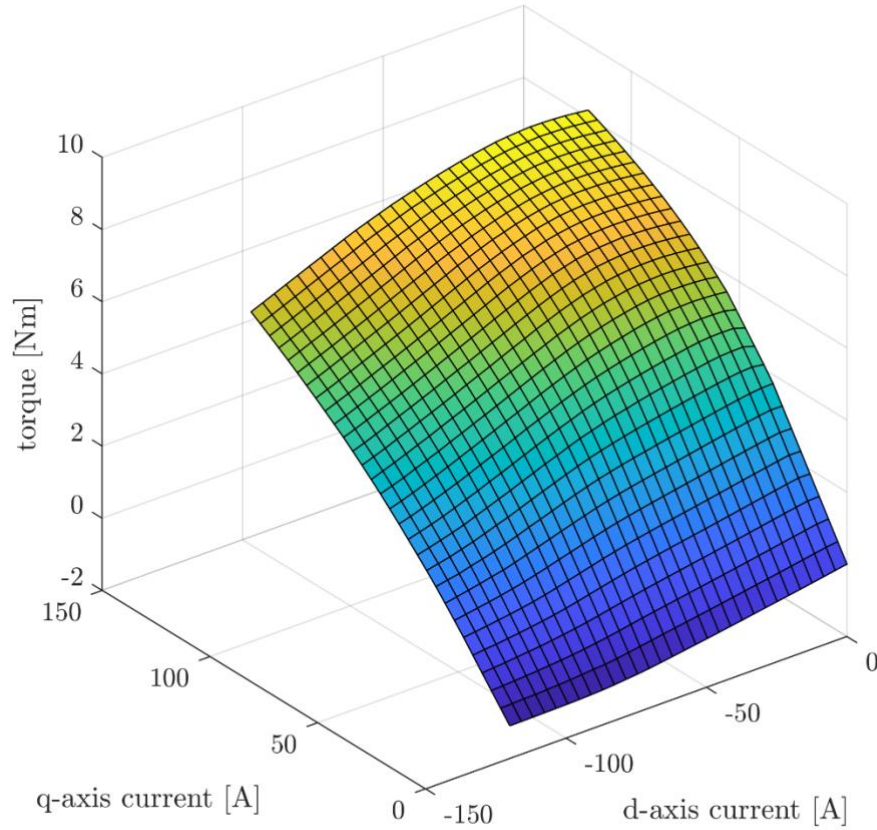


Figure 3. 35: Torque-current characteristic

These maps are used in the test to model the motor dynamics which is consequently affected by magnetic saturation i.e., inductance that varies with the applied current. The parameters obtained both from the maps or from calculation, as in the sub-section 3.2.1, are listed in the table 3.2. In particular, the synchronous inductance refers to the linear regions of the flux maps in d and q-axis: it has been computed isolating these parts and applying the following equations:

$$\begin{cases} L_d = \frac{\lambda_d(i_d, i_q = 0)}{i_d} \\ L_q = \frac{\lambda_q(i_d = 0, i_q)}{i_q} \end{cases} \quad (3.8)$$

Then, L_s has been obtained through the average of these two values, being them very similar to each other, thus keeping the SPM control features. In addition, the switching frequency and maximum voltage of the power stage are respectively $f_s = 20$ kHz and $v_{max} = 27.71$ V.

Table 3. 2: Flux maps machine parameters

Description	Symbol	Value
Number of pole pairs	p	5
Phase resistance	R_s	13.7 m Ω
Synchronous inductance	L_s	412 μ H
Permanent magnet flux linkage	λ_m	14.9 mWb
DC-link voltage	v_{dc}	48 V
Maximum RMS current	$i_{\max(RMS)}$	86.4 A (rms)
Maximum phase current	i_{\max}	122.2 A
Machine torque constant	k_t	0.11 N/A
Maximum torque	T_{\max}	8.1 Nm
Base speed	ω_b	105.5 rad/s
Maximum speed	ω_{\max}	1256 rad/s
Machine characteristic current	I_0	36.2 A

As regards as the control algorithm structure, it is the same of the previous application (sub-section 3.2.2), except for the calibration of the PI regulator for the FWC and current loop. The new tuning parameters are shown in the table below.

Table 3. 3: Flux maps control calibration

Description	Symbol	Value
FWC proportional gain	k_{pfw}	0.34 A/V
FWC integral gain	k_{ifw}	12.46 A/Vs
Current control bandwidth	ω_c	6283 rad/s
Current proportional gain	k_p	2.59 V/A
Current integral gain	k_i	86 V/As

These values have been computed with the same previous method, utilizing the linear synchronous inductance; however, since the machine saturation is simulated, the real control bandwidth will vary with the operating point.

3.3.2. Test

In this sub-section is presented a test to verify the control functionality with the flux map based motor model and highlight the differences with respect to the previous simulation (sub-section 3.2.3). The plant model is the same, except for the motor which uses a flux based model block of the toolbox (fig. 3.36), adequately set through the flux maps parameters.

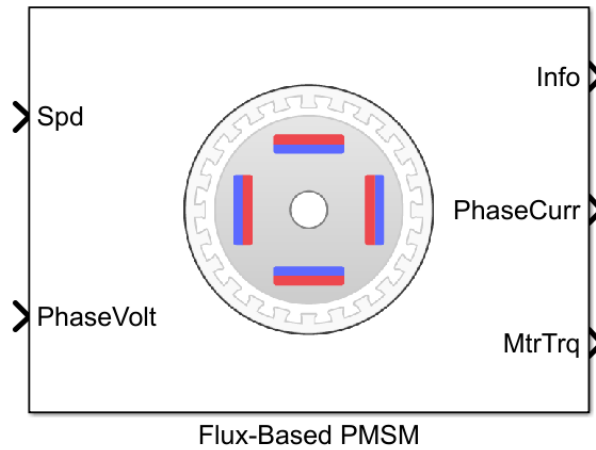


Figure 3. 36: Flux map based motor model

In the following simulation, the motor speed is imposed by an external load and the torque reference is given to the control algorithm; the rotor position estimation is performed by means of the flux observer. The speed range is between 500 and 6000 rpm while the torque request is increased by steps from 0 to 5 Nm. The plots below shows the mechanical and electrical variables results.

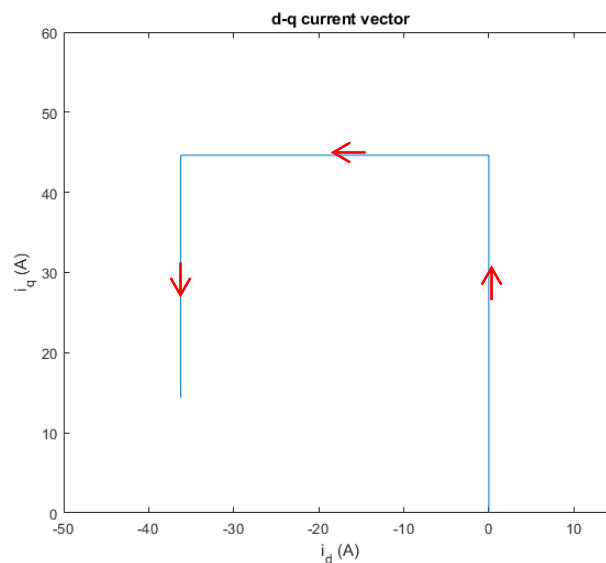


Figure 3. 37: Test flux, current space vector

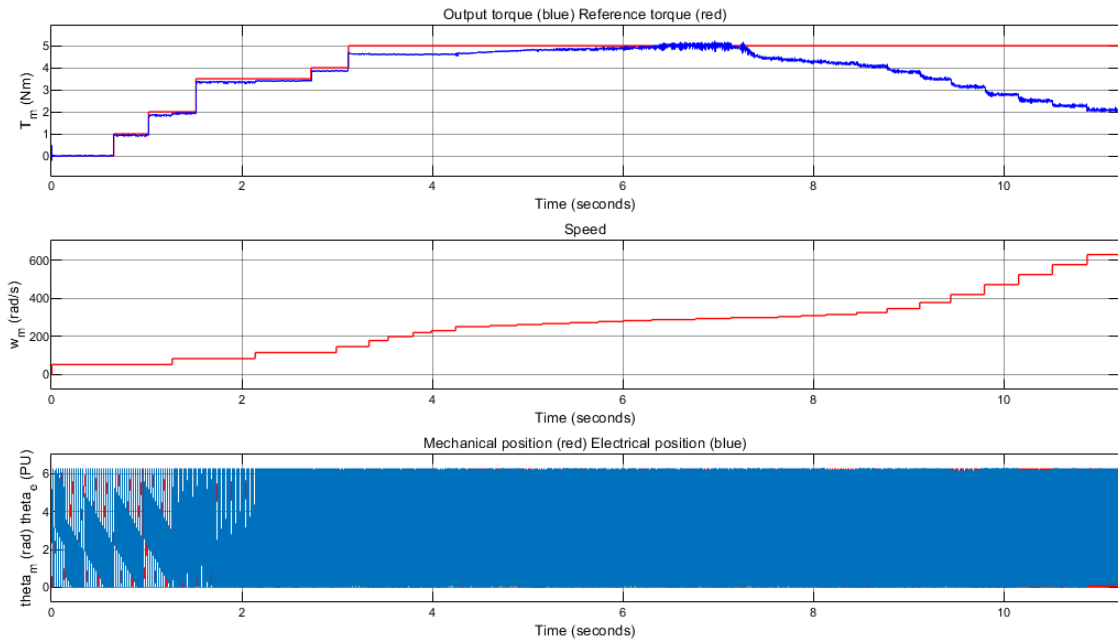


Figure 3.38: Test flux, torque-speed-position

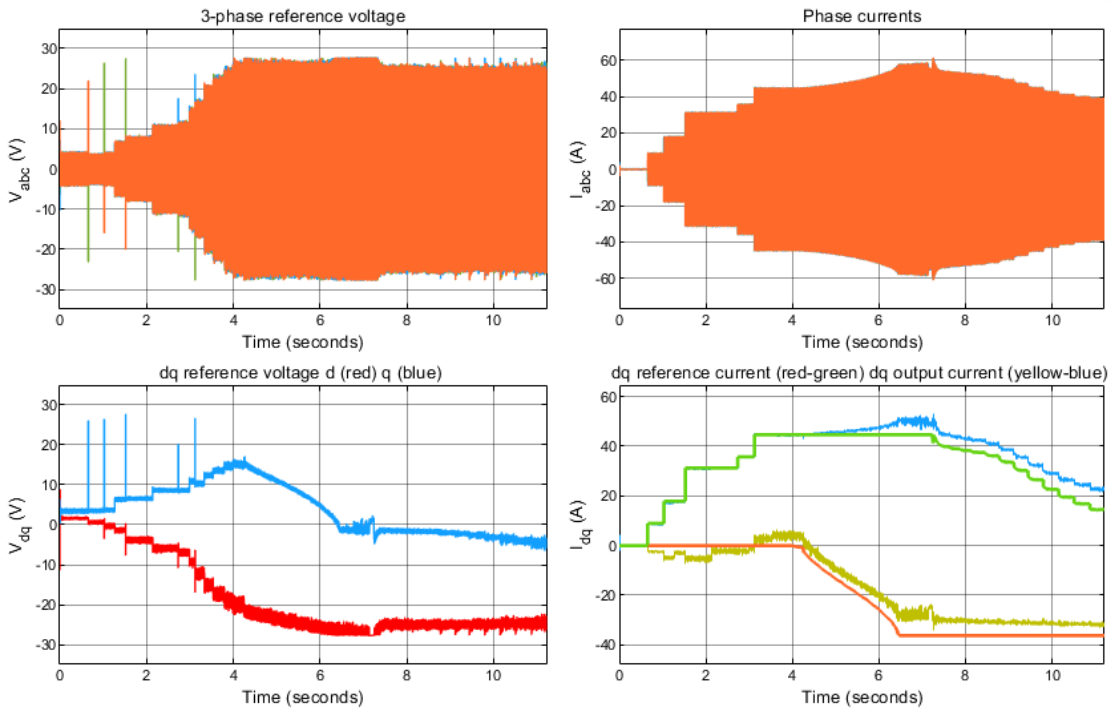


Figure 3.39: Test flux, voltages and currents

From the test, it can be deduced the validity of the control algorithm also for this application: the system correctly performs the same strategies and trajectories but with a different motor model and so different operating points. On the other hand, the errors that brings the magnetic saturation can be noted. In fact, the tracking error on the torque reference is more evident than the previous one, that was only due to the sensorless

estimators; now it rises increasing the speed because of the inductance and temperature change of the PMs.

4. Experimental campaign

In this chapter it is explained what has been done during the experimental campaign. The first practical contribution of the work has been the settings and validation of the power stage components. Therefore, two different 3-phase inverters are presented, together with their comparison and functionality considerations. Then, the battery pack analysis has been considered and the Hall sensors implementation and integration in the drive has been performed. Successively, the study has evolved into the test bench preparation, with the proper connection of a Texas Instruments development kit and the programming of the electronic control unit. Finally, the results are shown, together with the final considerations about the use of different combinations of components and algorithm calibration.

4.1. Power stage

4.1.1. *3-phase inverter*

Two different 3-phase inverters have been considered to run the motor. In order to make a proper choice they have been tested and calibrated under several conditions. They are the DRV8353RS and the DRV8323RS drivers of Texas Instruments: highly-integrated gate drivers for 3-phase applications, which use a smart gate drive (SGD) architecture to decrease the number of external components that are usually necessary for MOSFET slew rate control and protection circuits. Moreover, they optimize the dead time to prevent short-circuit conditions, also monitoring the gate-source voltage, and provide flexibility in lowering the EMI. In addition to that, various PWM control modes are supported for simple interfacing the external controller. The configuration setting for the gate driver and device are highly configurable through the SPI. Both devices integrate three high-accuracy trimmed and temperature compensated half-bridge drivers, each capable of driving high-side and low-side N-type MOSFETs. A doubler charge pump feeds the correct gate bias voltage to the high-side MOSFET across a wide operating voltage range in addition to providing 100% duty-cycle support; the internal linear regulator generates the gate bias voltage for the low-side MOSFET. Moreover, since 6x PWM mode has been selected, each half-bridge supports three output states: low, high or high-impedance. The next figure represents the block diagram of both drivers.

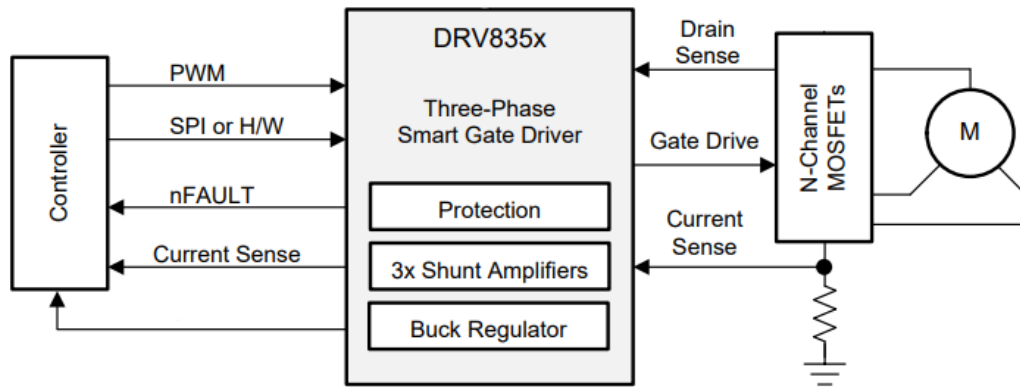


Figure 4. 1: Inverter block diagram

DRV8353RS

The first 3-phase inverter tested to check its functionality for the work application has been the TI DRV8353RS (fig. 4.2 and 4.3).

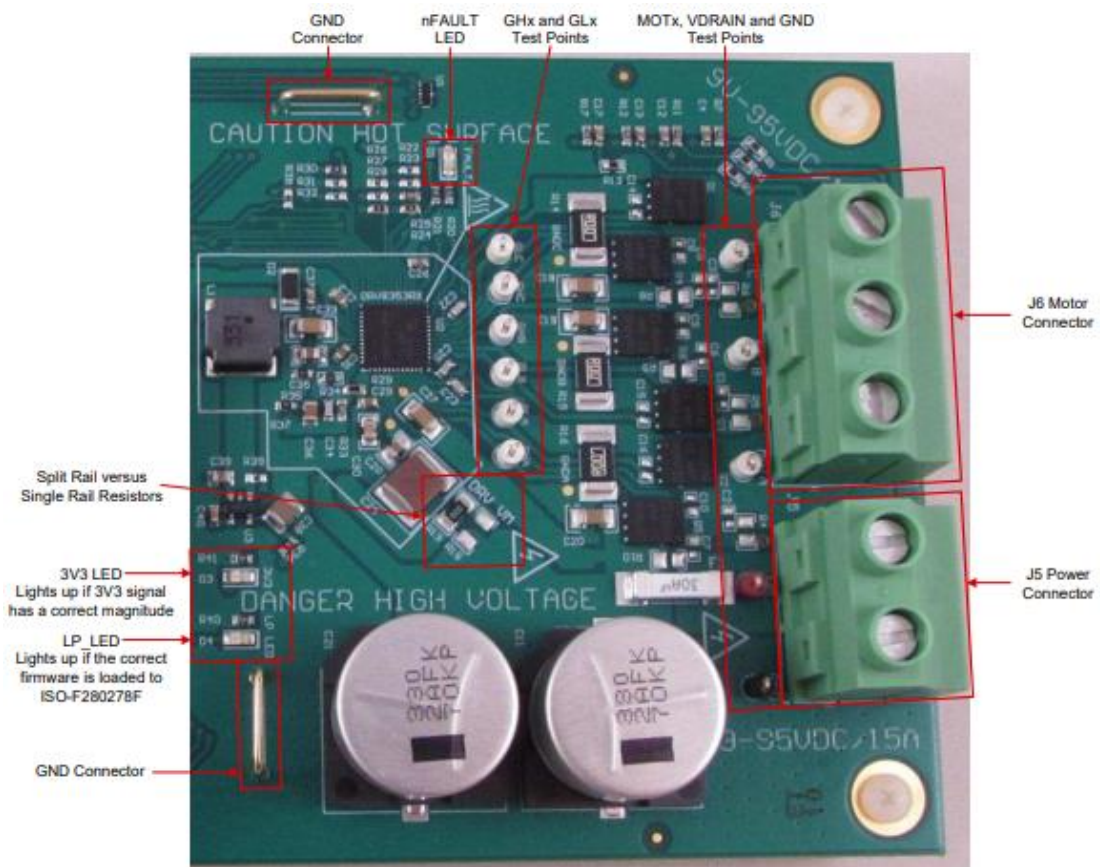


Figure 4. 2: DRV8353RS-first side [31]

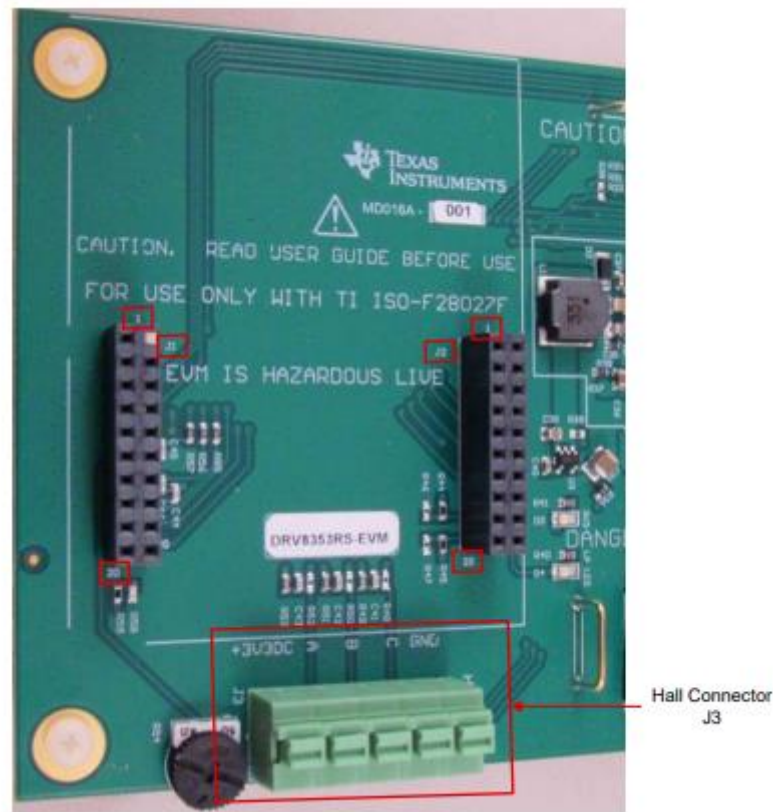


Figure 4. 3: DRV8353RS-second side [31]

It is designed for an input supply from $9 V_{dc}$ to $95 V_{dc}$ and up to $15 A$ continuous drive current.

Due to the wide range of system configurations and efficiency requirements, this driver supports a flexible power supply architecture to provide different trade-offs in power supply integration and device efficiency. Thus, it has been evaluated the optimal power supply configuration to integrate the inverter to the rest of the power stage. First of all, there are three primary power supply inputs [32]:

- VM, which is the driver primary power supply input.
- VDRAIN, that is the driver secondary power supply input.
- VIN, which is the buck regulator power supply input.

Two different power supply architectures are explained.

- Single power supply configuration (fig. 4.4):

In the single power supply configuration, all the three inputs are connected to a main external power supply which is also used directly for the external MOSFET half-bridges [32]. This method removes the intermediate buck regulator typically used to generate 12 to

15 V for the gate driver power supply. Thus, the driver internally regulates down the high voltage power supply to the immediate levels.

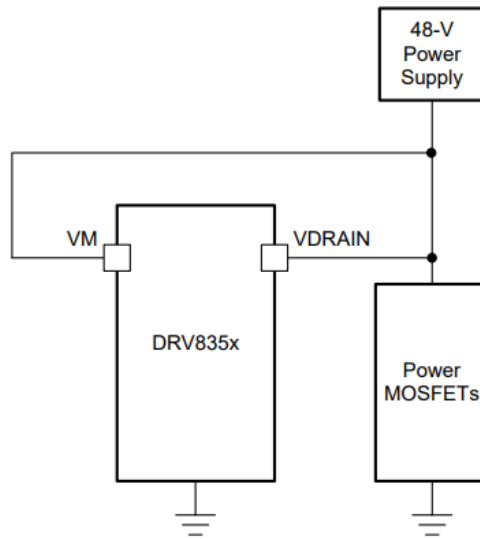


Figure 4. 4: Single supply configuration [31]

This solution cancels the need for an additional regulator in the system, lowering the system cost and size; on the other hand, there is an increased power dissipation inside the driver that is internally regulating the high voltage input down to the intermediate power supplies.

- Split power supply configuration (fig 4.5):

In this architecture only the VDRAIN and VIN inputs, together with the external MOSFET half-bridges are connected directly to the main external power supply [32]. The VM input is connected to the lower voltage supply between 12 and 15 V.

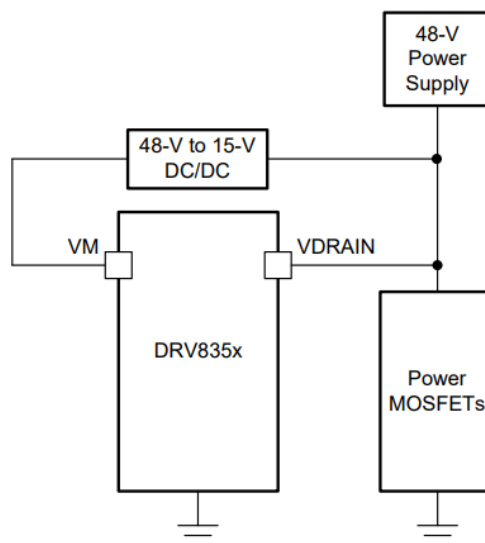


Figure 4. 5: Dual supply configuration [31]

This method reduces the internal power dissipation of the driver allowing it to work up to higher ambient temperatures, increases its efficiency and the max allowable gate drive current. However, it adds additional system cost and design complexity due to the need of an intermediate power supply voltage in between the main power supply and the logic power supply.

As regards as the project, both configurations have been tested. In particular, the work has been done with an original driver of this typology and a modified one. The original inverter is by default in split rail configuration: it incorporates the buck converter to provide internally $12 V_{dc}$. This voltage is also used by a low-dropout regulator (LDO) which is a DC linear voltage regulator used to feed $3.3 V_{dc}$ to the controller board. Another driver of the same typology has been used and modified to test the other configuration i.e., single supply: in this case also the buck regulator output has been lowered directly to $3.3 V_{dc}$ permitting to connect the control stage to it without using the LDO. Other modifications have been done in the half-bridges and sense side on this inverter and are successively explained.

As previously said, a standard SPI provides a simple method for configuring the various device settings and reading fault diagnostic information through an external controller. In fact, this driver integrates a wide range of protection features; these include power-supply undervoltage lockout, gate drive undervoltage lockout, drain-source voltage overcurrent monitoring, gate-driver short-circuit detection and overtemperature shutdown. The serial communication bus allows for an external controller to send and receive data with the inverter, with a four wire interface utilizing the following pins [33]:

- The SCLK pin, which is an input that accepts a clock signal to determine when data is captured and propagated on the SDI and SDO.
- The SDI pin, that is the data input.
- The SDO pin, which is the data output.
- The nSCS pin, which is the chip selected input i.e., a logic low signal on this enables SPI communication with the driver.

The SPI works in slave mode and connects to a master controller. The SDI consists of a 16 bit word, with a 5 bit command and 11 bits of data (fig. 4.7); the SDO word is composed by 11-bit register data, with the first 5 bits that are do not care bits (fig. 4.8) [33].

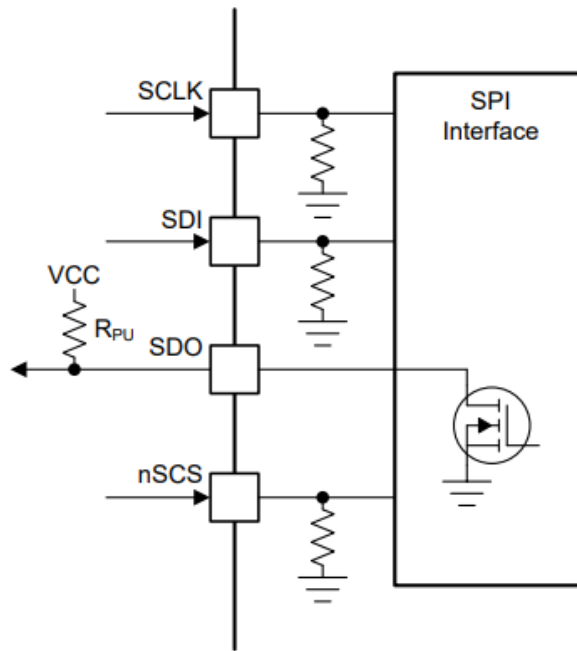


Figure 4. 6: SPI [33]

R/W	ADDRESS					DATA										
B15	B14	B13	B12	B11	B10	B9	B8	B7	B6	B5	B4	B3	B2	B1	B0	
W0	A3	A2	A1	A0	D10	D9	D8	D7	D6	D5	D4	D3	D2	D1	D0	

Figure 4. 7: SPI input data [33]

DON'T CARE BITS					DATA										
B15	B14	B13	B12	B11	B10	B9	B8	B7	B6	B5	B4	B3	B2	B1	B0
X	X	X	X	X	D10	D9	D8	D7	D6	D5	D4	D3	D2	D1	D0

Figure 4. 8: SPI output data [33]

The slave timing diagram to obtain a valid frame is depicted below.

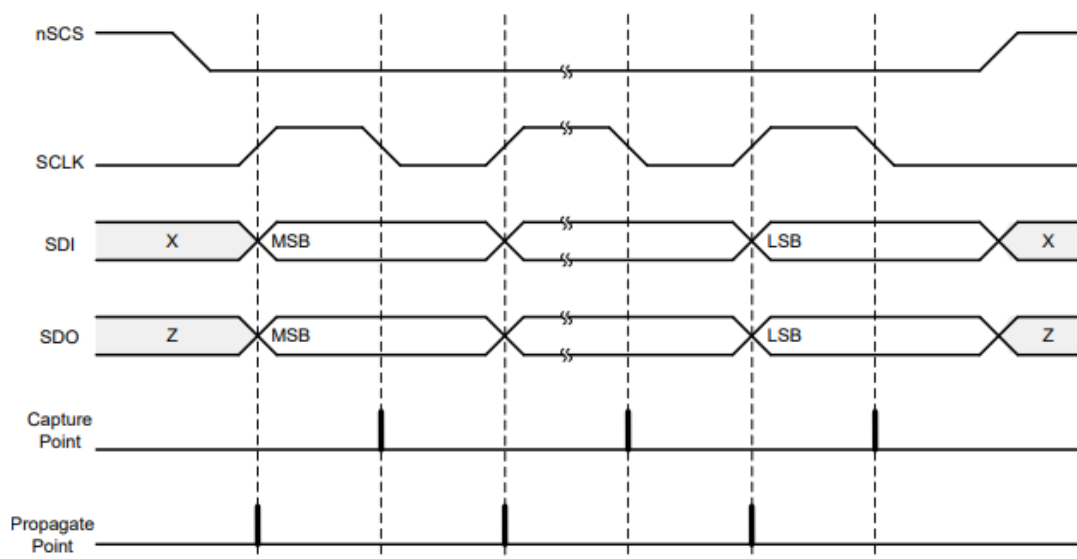


Figure 4. 9: SPI slave timing diagram [33]

The aforementioned communication is fundamental to set the proper gate-drive current needed to control the MOSFETs. The gate drivers use an adjustable, complimentary, push-pull topology for both the high-side and low-side drivers; this permits both a strong pullup and pulldown of the external MOSFET gates [33]. This architecture is implemented through the IDRIVE component. In addition, the TDRIVE device provides a smart architecture able to control and protect the MOSFETs. In particular, the IDRIVE component implements adjustable gate-drive current to control the MOSFET v_{ds} slew rates, resulting in desired rise and fall times. These are critical factor for optimizing energy and duration of diode recovery spikes, optimizing radiated emissions and switching voltage transients related to parasitic in the external half-bridge. Therefore, the slew rates are determined by the rate of gate charge i.e., the gate current delivered during the MOSFET charging region Q_{dg} . The driver allows to dynamically switch between gate drive currents, thus controlling the slew rate of the external power MOSFETs, through a SPI register settings. By default, they are set to a value equal to 1 A which is absolutely too high for the application and can yield to the risk of damaging the driver; as a matter of proof, during the experimental tests two drivers burned due to the latter default settings. Thus, both the original and modified inverters of the project have been tuned with a 150/300 mA gate drive current. Moreover, this are delivered to the gate, respectively, during the turn-on and turn-off of the external power MOSFET for the t_{drive} time duration; then, the gate driver switches to a smaller hold I_{HOLD} current to improve the driver efficiency [33]. In parallel to this strategy, there is the work of the TDRIVE component; it is an integrated gate-drive state machine that provides automatic dead time insertion through switching handshaking, to avoid cross conduction, parasitic dV/dt gate turn-on prevention by means of a strong pulldown I_{STRONG} current on the opposite MOSFET gate and gate-fault detection. Figure 4.10 illustrates an example of state machine in operation. If the I_{DRIVE} selected is too low for a particular MOSFET, then the latter may not turn-on completely within the t_{drive} time and a gate-drive fault may be caused. In addition, slow rise and fall times lead to higher switching power losses. At the end, I_{DRIVEP} and I_{DRIVEN} current for both the low-side and high-side MOSFET should respect the following equations:

$$\begin{cases} I_{DRIVEP} > \frac{Q_{gd}}{t_r} \\ I_{DRIVEN} > \frac{Q_{gd}}{t_f} \end{cases} \quad (3.9)$$

where Q_{gd} is the known gate-to-drain charge while t_r and t_f are the desired rise time and fall time [33]. However, the I_{DRIVE} should not be too strong since it may cause cross-conduction damages and output ringing.

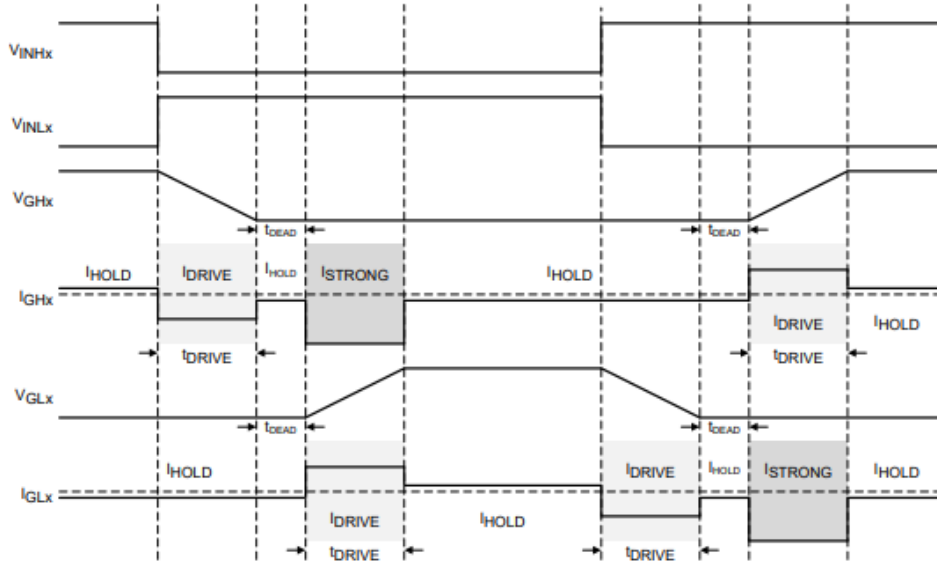


Figure 4.10: TDRIVE state machine [33]

At conclusion of the smart gate driver’s current consideration, the switch node and gate lines have been checked through an oscilloscope to make sure that the MOSFETs were fully getting turned on and there was minimal ringing on the lines due to overshoot and undershoot; of course, the test has been done with the aforementioned choice of I_{DRIVE} currents. The figure below shows its correct switching functionality.

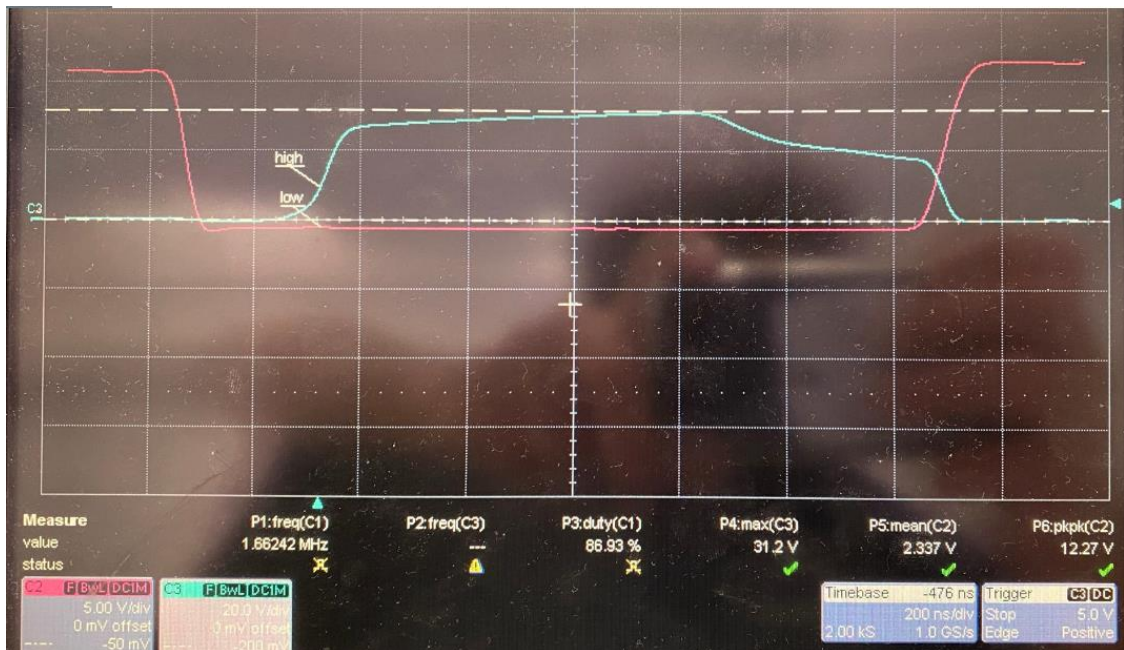


Figure 4.11: DRV8353RS switching

Finally, thermal considerations on the half-bridges and sense side of the inverter have been performed. The driver integrates three high-performance bidirectional current-shunt amplifiers for monitoring the current level through each of the external half-bridge using a low-side shunt resistor. By means of the SPI communication it is possible to set the gain of the shunt amplifier and adjust the output bias point. Therefore, all three amplifiers can be used to sense the current in each of the half-bridge legs. It is obtained through the measure of the analog voltage v across the shunt resistor R_{SENSE} pins, that is multiplied by the gain setting G_{CSA} ; the current is then deduced with the use of the following equation:

$$I = \frac{v_{SO}}{G_{CSA} \times R_{SENSE}} \quad (3.10)$$

where, being used the default option for the shunt amplifier gain, G_{CSA} is set to 20 V/V; instead R_{SENSE} is equal to 7 m Ω in the original inverter [33].

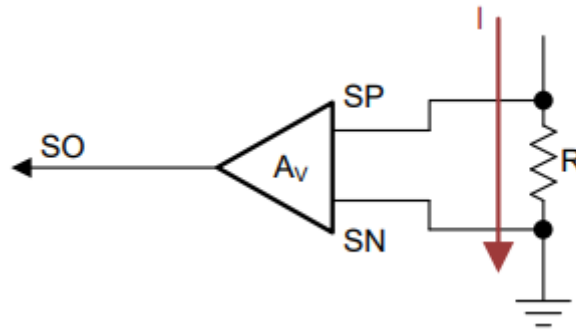


Figure 4. 12: Current-shunt amplifier [33]

The sense resistor value must be selected on the base of the target current range, sense-resistor power rating and operating temperature range. Therefore, in the following lines thermal tests performed on the original inverter are presented, in order to make considerations about its standard settings. Figure 4.13 shows the test bench preparation: it consist of the inverter fed by a 48 V_{dc} power supply, the TI development kit which drives the power stage through the input coming from the connected laptop, the load that is an SPM synchronous motor and the thermal imaging camera used to take the measurements. The first check has been done with the inverter in sleep-mode condition, just powered-up with disabled switching. In the figure 4.14 there is the result, where it is visible the LDO reaching 81.3 °C. This is an anomaly in the original configuration of this driver; in fact, it is not able to power the control board that must be fed by the USB cable of the laptop. As a consequence, the single supply configuration of the modified inverter could be seen as the correct choice between the two available architectures; however, it is even preferable for

this type of applications to split the power level with the control level, providing the $3.3 V_{dc}$ voltage to the control board through an external buck regulator interfaced between the power supply and the board itself.

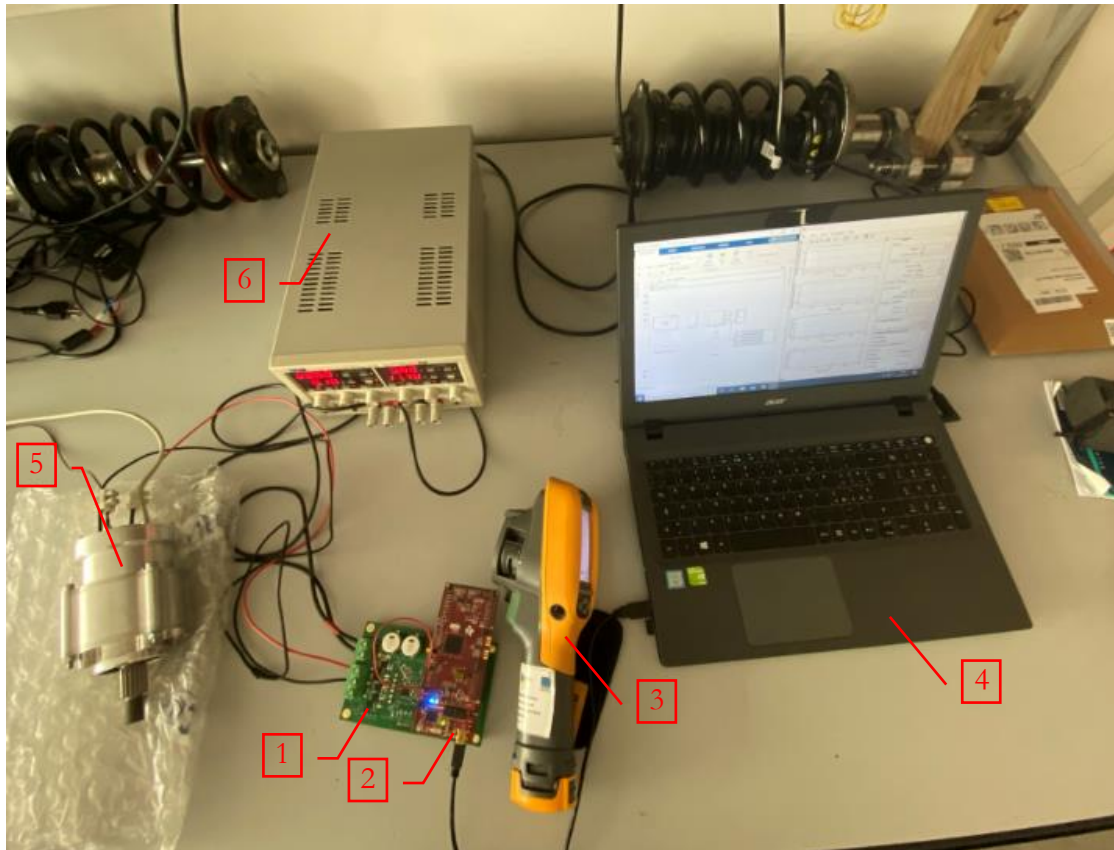


Figure 4.13: DRV8353RS thermal test bench. DRV8353RS inverter (1), LAUNCHXL F28379D (2), thermal imaging camera (3), laptop (4), SPM e-motor (5), power supply (6)

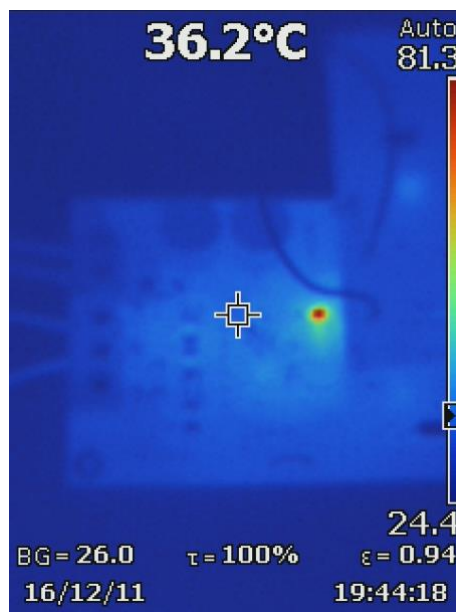


Figure 4.14: LDO thermal test

The second test has been performed driving the load with $15 A_{dc}$ to the a and b-phases and acquiring the temperatures of the MOSFETs and shunt resistors every 30 s. In the following pictures there are the acquisitions, where the pointer is positioned on the MOSFET surface and the sense resistor's temperature level is the maximum in the region shown.

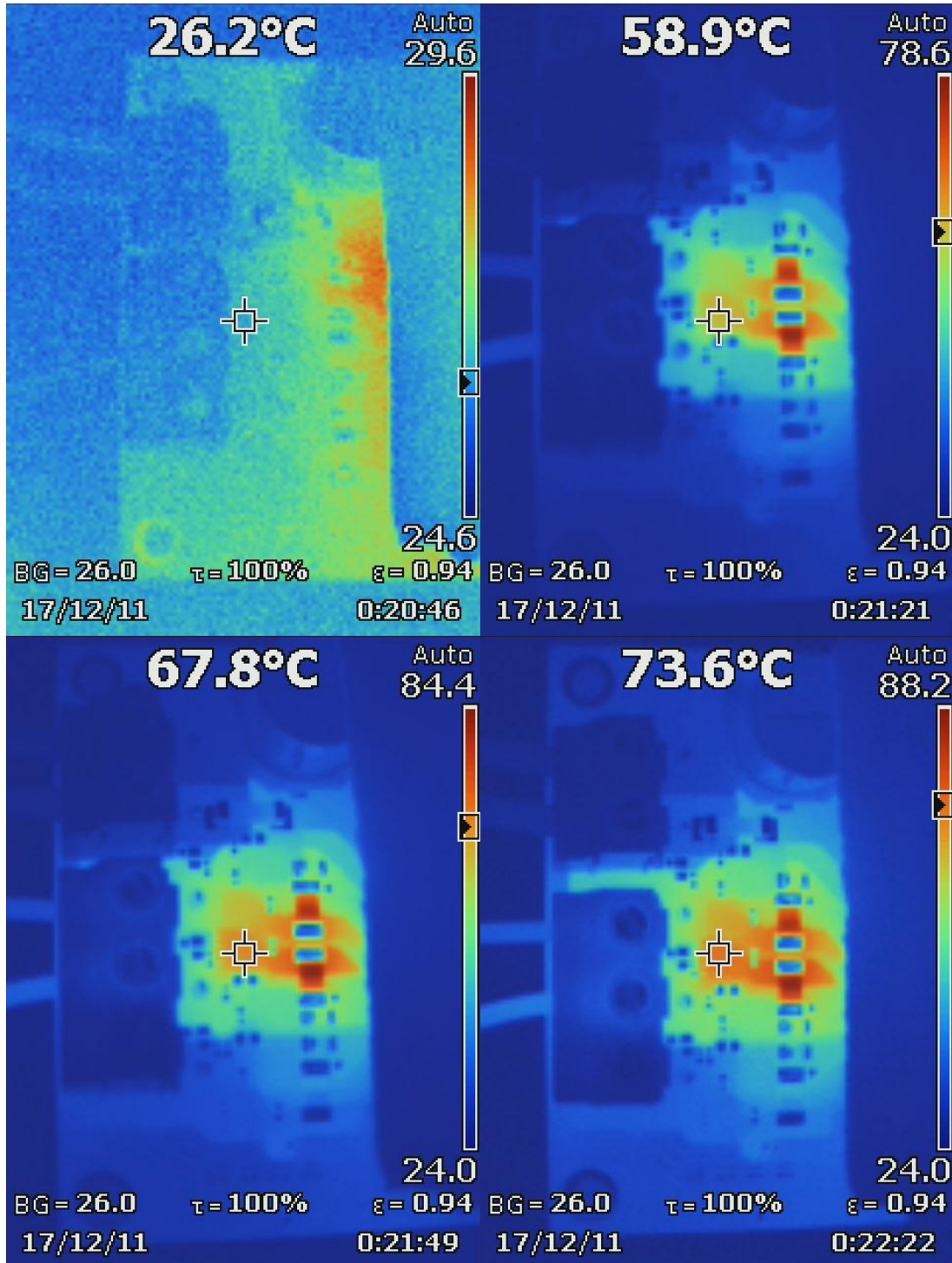


Figure 4. 15: DRV8353RS thermal test, $15 A_{dc}$

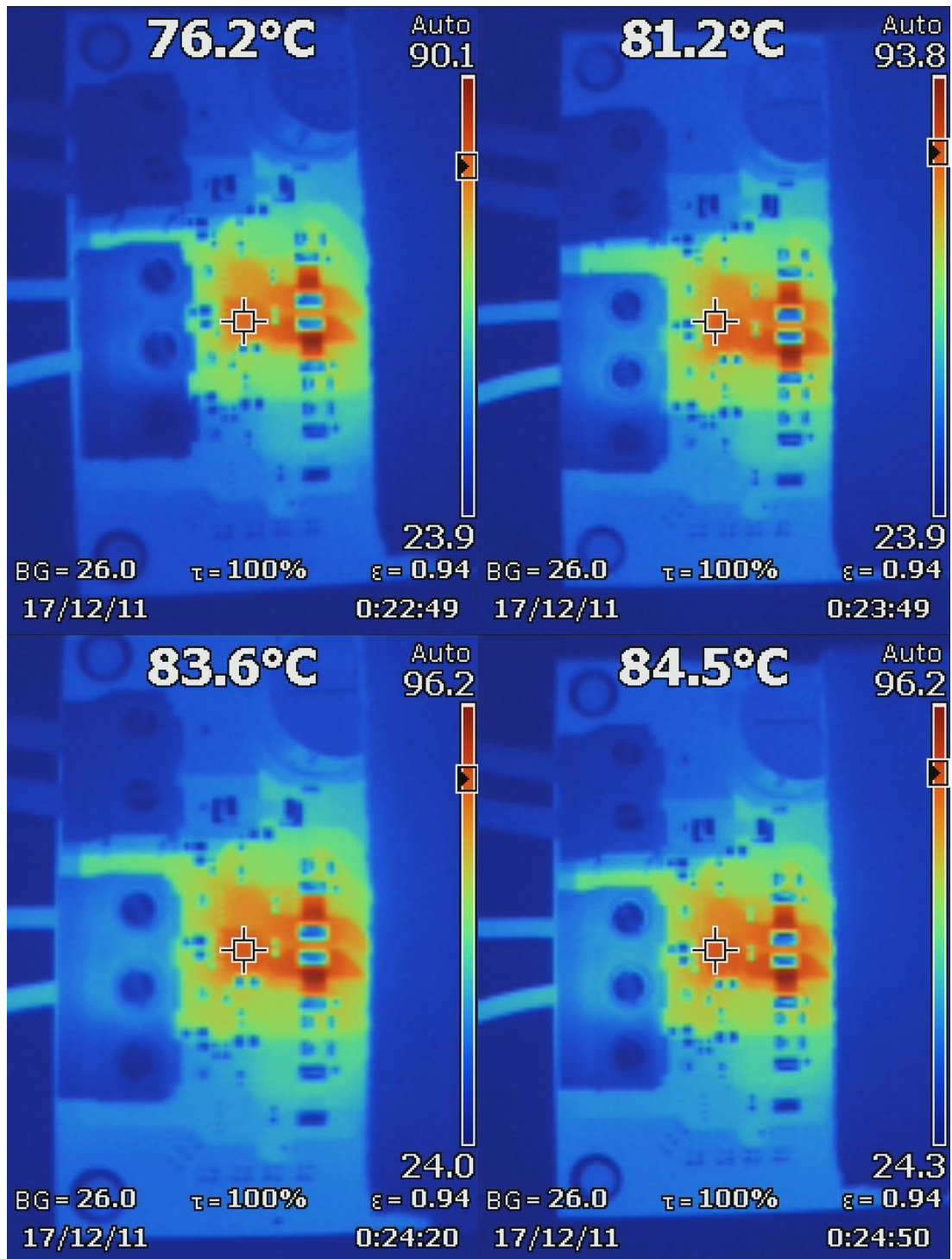


Figure 4. 16: DRV8353RS thermal test, 15 A_{DC}

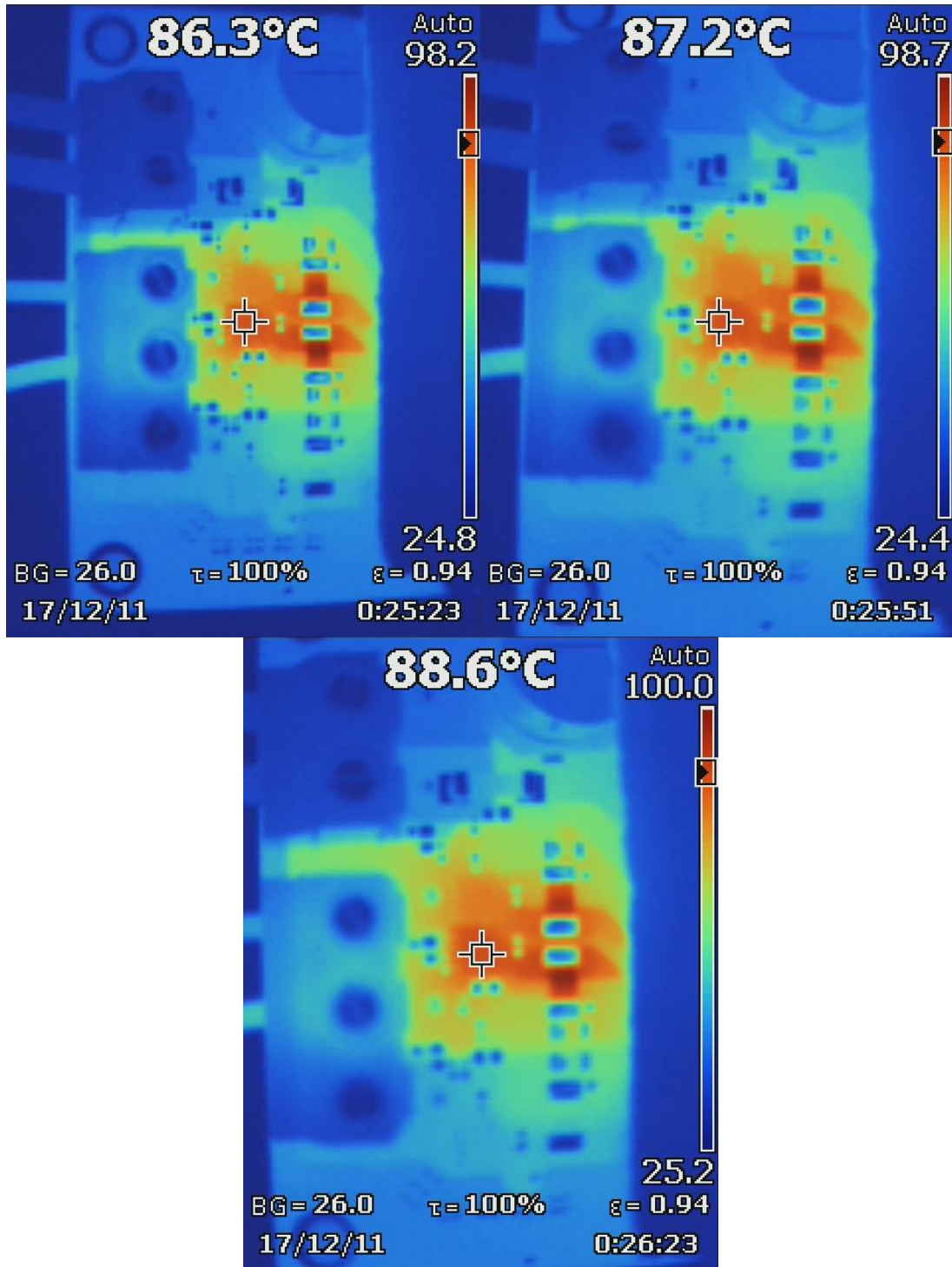


Figure 4. 17: DRV8353RS thermal test, 15 A_{DC}

The following table collects the value of the MOSFET temperature versus time:

Table 4. 1: DRV8353RS thermal test, 15 A_{DC}

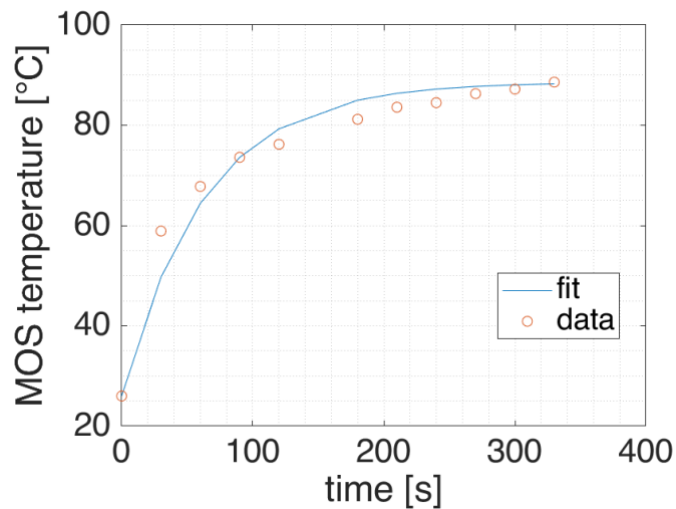
Time (s)	Temperature (°C)
0.01	26
30	58.9
60	67.8
90	73.6
120	76.2
180	81.2
210	83.6
240	84.5
270	86.3
300	87.2
330	88.6

It is possible to note that as expected the temperature dynamics is similar to the one of a first order system:

$$T = T_0 + (T_{end} - T_0) \left(1 - e^{-\frac{t}{\tau}}\right) \quad (3.11)$$

Therefore, through the use of the MATLAB Curve fitting toolbox the following parameters of the function have been computed:

- $T_0 = 26$ °C.
- $T_{end} = 88.6$ °C.
- $\tau = 62.99$ s.

**Figure 4. 18:** DRV8353RS thermal test, 15 A_{DC} dynamics

Finally, another check has been computed driving the load with 30 A and 50% duty-cycles to the a and b-phases.

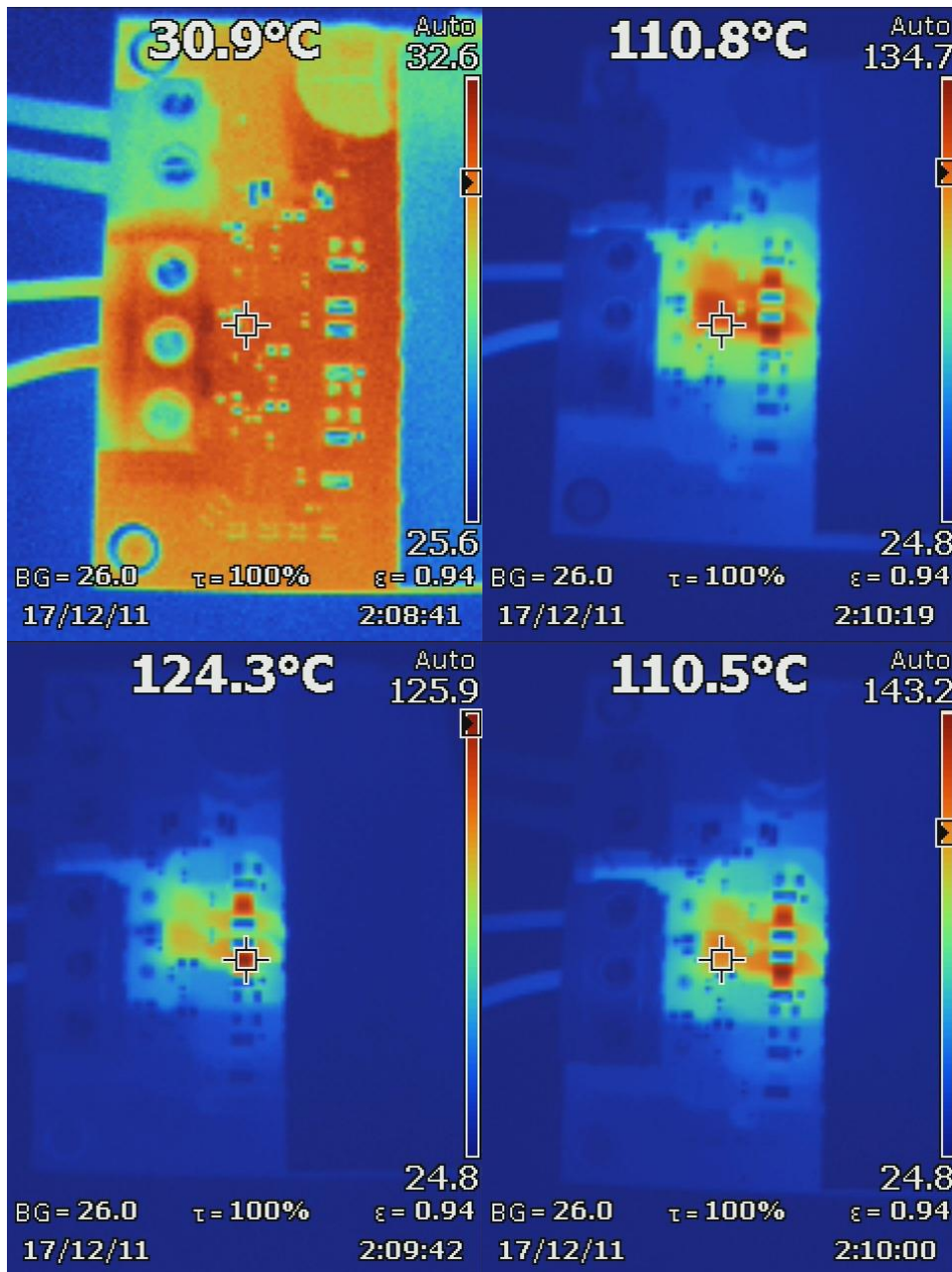


Figure 4. 19: DRV8353RS thermal test, 30 A 50% duty-cycles

In this case, after two minutes, the shunt resistors and MOSFETs reach temperature levels in the order of 140 °C and 110 °C respectively.

As regards as the half-bridges and sense side of the driver, it is possible to conclude that its original configuration do not provides safety working condition because of the huge increment in the MOSFETs and shunt resistors temperature. Additionally, the currents

driven by the suspension in the project can reach even approximately values greater than 100 A through small spikes; thus, the modified version of the same inverter, previously presented, also includes these changes (fig. 4.20):

- $R_{SENSE} = 1 \text{ m}\Omega$.
- Heat sinks mounted on the MOSFET surfaces and on the bottom of the board.
- 100 V_{dc} – 30 A fuse removed.

In parallel, another consideration has been done regarding the maximum measurable current, limited by the ADC voltage range: the v_{SO} voltage in the equation 3.10 is bounded and after a certain value it is no more able to follow current increments. Thus, the product $G_{CSA} \times R_{SENSE}$ should be properly set depending on the current levels; therefore, apart from decreasing the shunt resistor value, also the gain setting may be tuned at 5 V/V, which its minimum settings, in order to increase the maximum obtainable current.

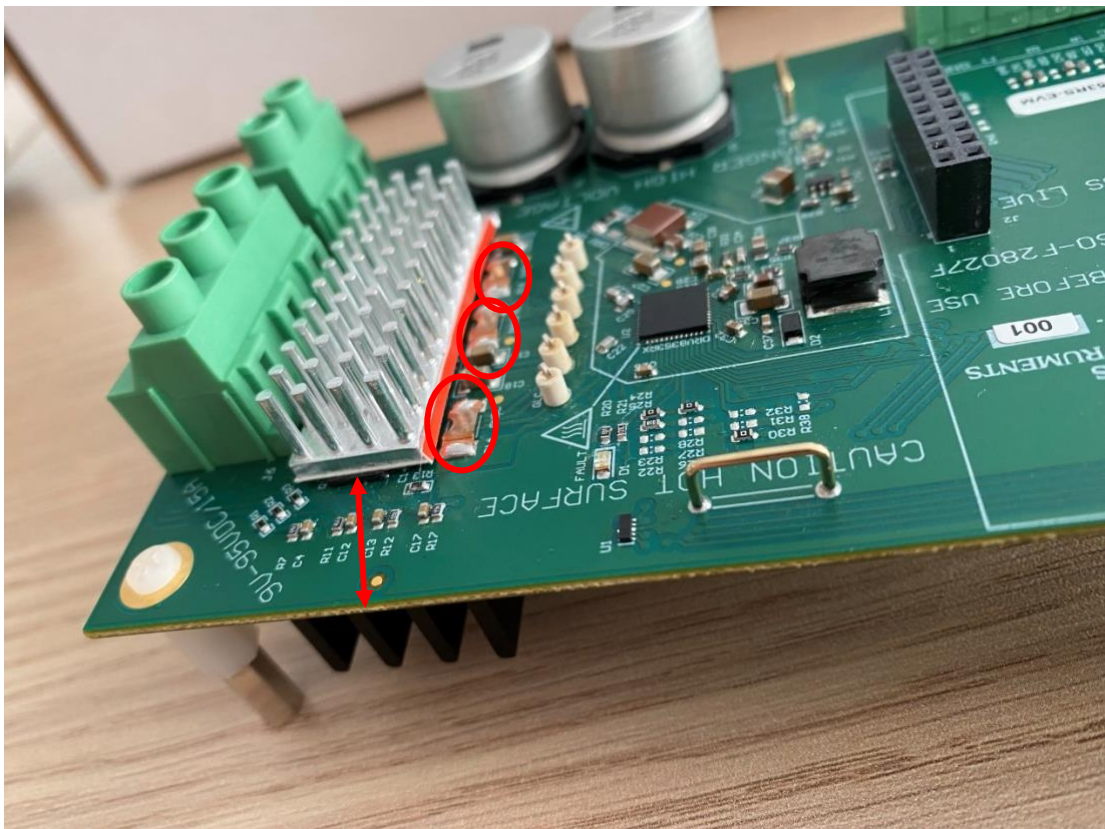


Figure 4. 20: DRV8353RS, modified version

DRV8323RS

The second 3-phase typology tested for the project has been the TI DRV8323RS.

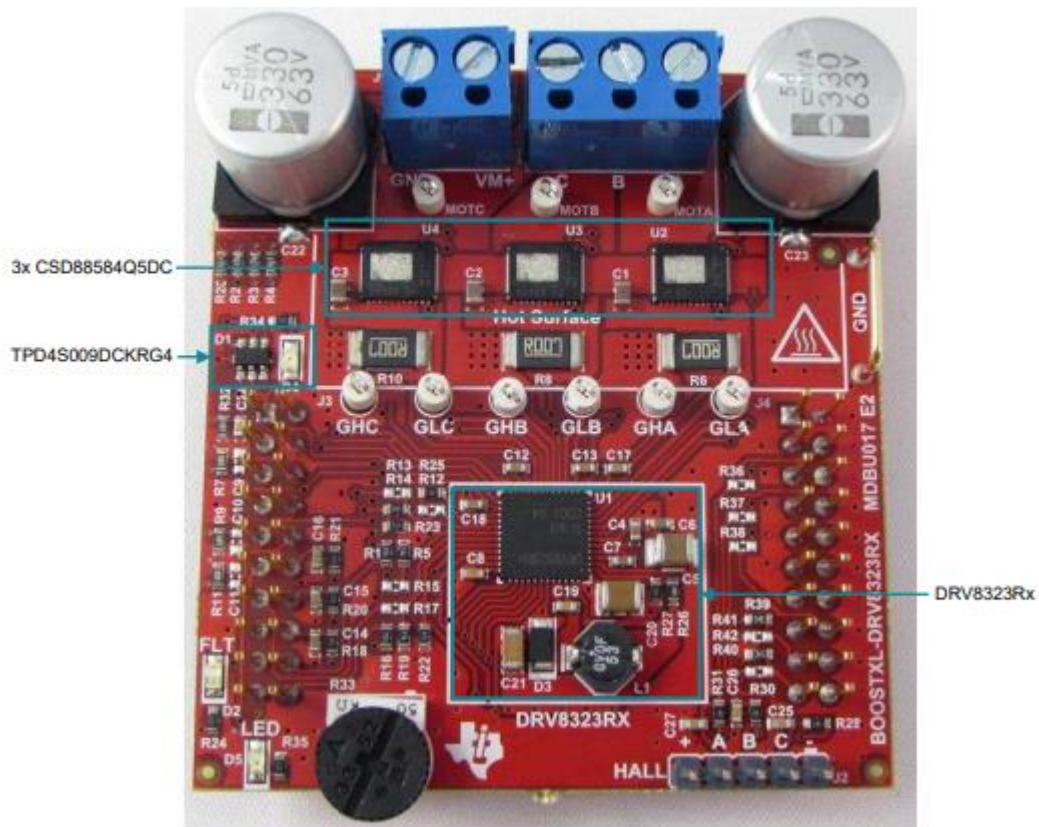


Figure 4. 21: DRV8323RS overview [34]

It is designed for an input supply from 6 to 54 V and up to a 15 A drive current [34].

Firstly, this driver has only one power supply architecture: the voltage supply of the low-side gate driver is generated using a linear regulator that operates from the VM voltage supply input; its output is fixed at 11 V [35]. In addition to that, another linear voltage regulator is integrated to provide the supply voltage for the low-power ECU i.e., the 3.3 V_{DC}. Thus, in this case the controller board can be fed directly by the inverter with no problem, although, as previously stated, it is preferable to power it from an external buck regulator.

As regards as the SPI communication, the two driver's standards are exactly the same, together with their functionalities. On contrary, the SGD architecture of this typology supports peak gate drive currents up to 1 A source (i_{DRIVEP}) and 2 A sink (i_{DRIVEN}); therefore, it does not require any tuning of the latter currents that are just set to their default values.

Successively, considering the half-bridges and sense sector, this driver integrates the same three bidirectional current sense amplifiers strategy for monitoring the current level (fig. 4.12); moreover, it includes different MOSFET's typology but a R_{SENSE} shunt resistor value

still equal to $7\text{ m}\Omega$. Also in this case, thermal considerations have been performed on the original inverter to check its standard settings. The previous test bench has been adopted (fig. 4.13), except for the driver. It has been firstly tested providing 15 A_{DC} to the a and b-phases of the load: the following images shows the temperature levels reached on the board after every minute for three times; the pointer is positioned on the shunt resistors, moreover it is important to highlight that the MOSFET's surfaces are covered by a sheet metal which is blue in the pictures but their temperature values can be approximated from the levels immediately around.

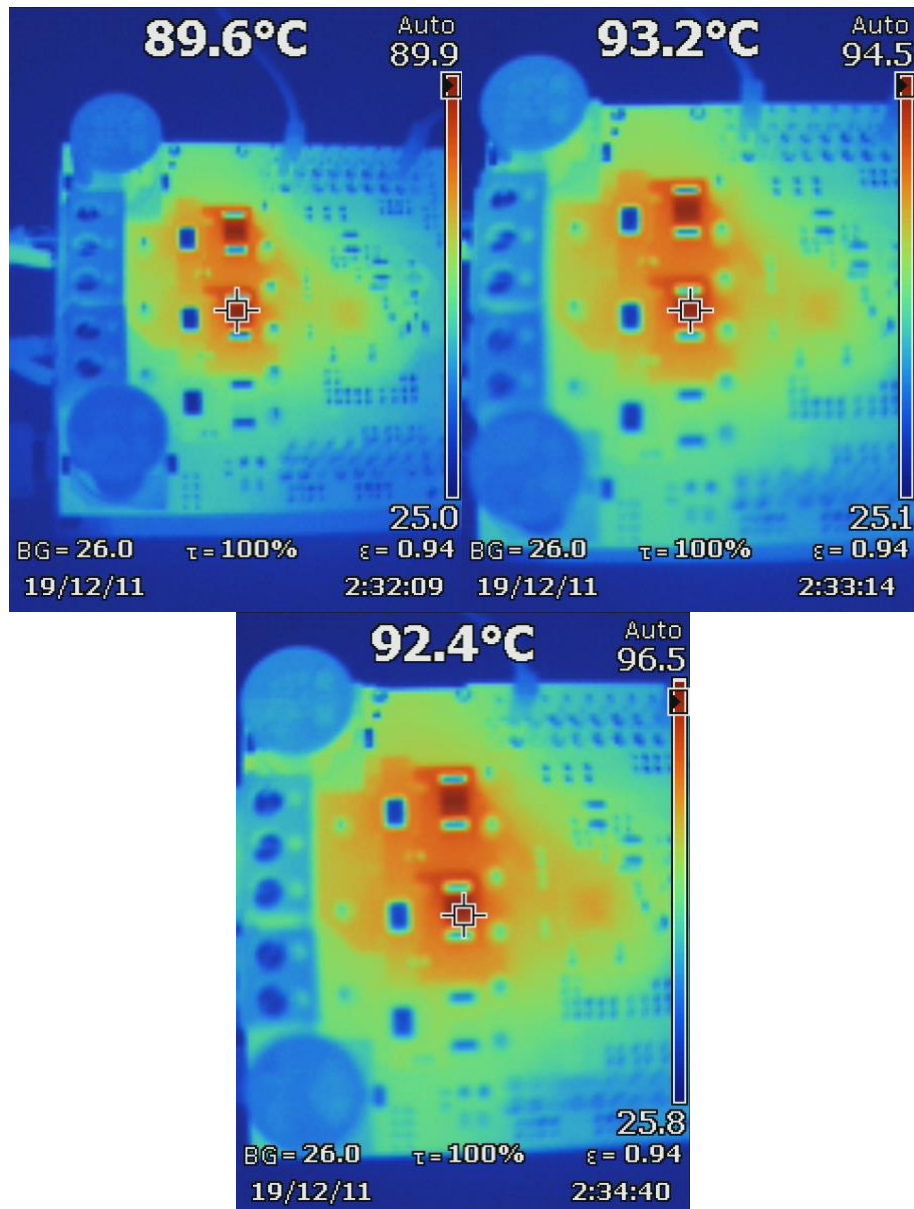


Figure 4. 22: DRV8323RS thermal test, 15 A_{DC}

Secondly, another check has been performed driving the load with 30 A and 50% duty-cycles to the a and b-phases. One acquisition has been done after two minutes.

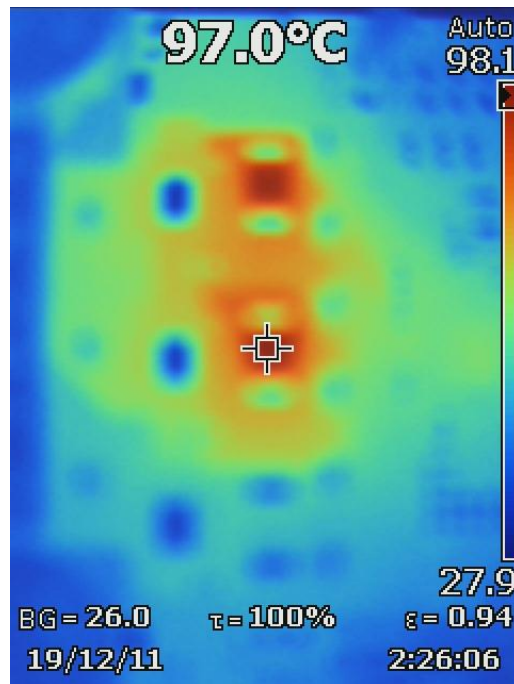


Figure 4. 23: DRV8323RS thermal test, 30 A 50% duty-cycles

It can be concluded that the shunt resistor temperature reaches too high levels making the whole area warm. Also in this case, some modifications have been made on a modified inverter of the same typology:

- $R_{SENSE} = 1\text{ m}\Omega$.
- Heat sinks mounted on the MOSFET surfaces, also covering the shunt resistors.

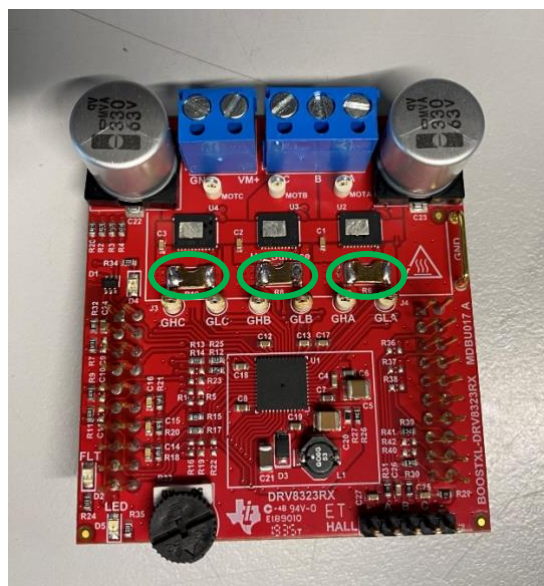


Figure 4. 24: DRV8323RS, shunt resistor change

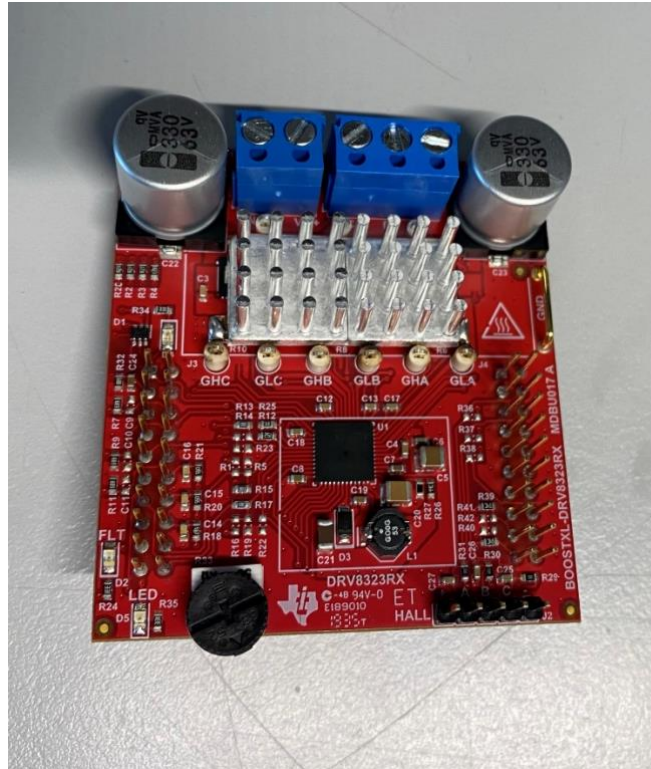


Figure 4. 25: DRV8323RS, heat sinks

Drivers' comparison

At the end, after several tests performed on both the DRV8353RS and the DRV8323RS drivers, together with their characteristics analysis, a choice between the two has been made in order to integrate one in the project power stage. The 3-phase inverter DRV8323RS has been selected as the most suitable driver typology for this application. Firstly, it includes a power supply architecture that do not need any modification and do not present criticalities. Secondly, the smart gate driver is much more robust: in fact, the default IDRIVE currents can be maintained without any problem. Additionally, by means of the thermal analysis performed, it is evident that this inverter is able to dissipate heat better; nevertheless, its modified version is used, with $1\text{ m}\Omega R_{SENSE}$ and the heat sinks mounted. On the other hand, it has a voltage supply input range lower than the other but during the work operations the power stage will never exceed the limit of 54 V . Finally, the integration of this inverter with the control board lead to a much more compact system due to its reduced sizes with respect to the other solution.

4.1.2. Battery pack

This sub-section presents a benchmarking analysis regarding the possible battery pack solutions to integrate in the suspension power stage.

In general, in the electric vehicles the battery is an electrochemical storage element representing a bidirectional energy source. The research has started considering its main features, that are:

- The capacity (Ah), which is the value of the charge that the battery is able to deliver during a full discharge process.
- The rated voltage (V) i.e., the output voltage provided by a fully charged battery.
- The rated energy (Wh), that is the product between the rated capacity and the rated voltage.
- The state of charge (SOC), which is the residual charge of a battery.
- The recharge and discharge rate.

For the application, a $48 V_{DC}$ battery pack is needed with as little as possible dimensions; additionally, it has been selected among the one with the Lithium iron-phosphate ($LiFePO_4$) technology. Actually, this is one of the best and most demanded battery typologies (fig. 4.26). It provides an optimal energy density, good high temperature performance and recyclability; moreover, there is not thermal run-away and no fire or explosion risks.

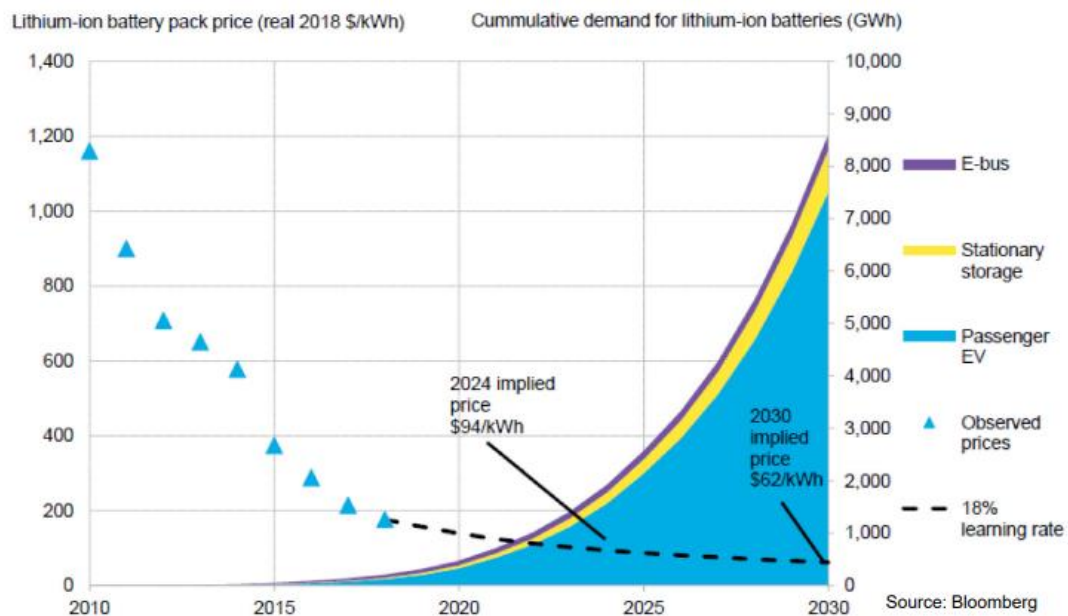


Figure 4. 26: Lithium iron-phosphate battery

Then, a standard automotive final solution (fig. 4.27) has to be reached i.e., with an embedded BMS. This device manages different functionalities, such as monitoring and communication, through current, voltage and temperature measurements to improve the battery lifespan and security.

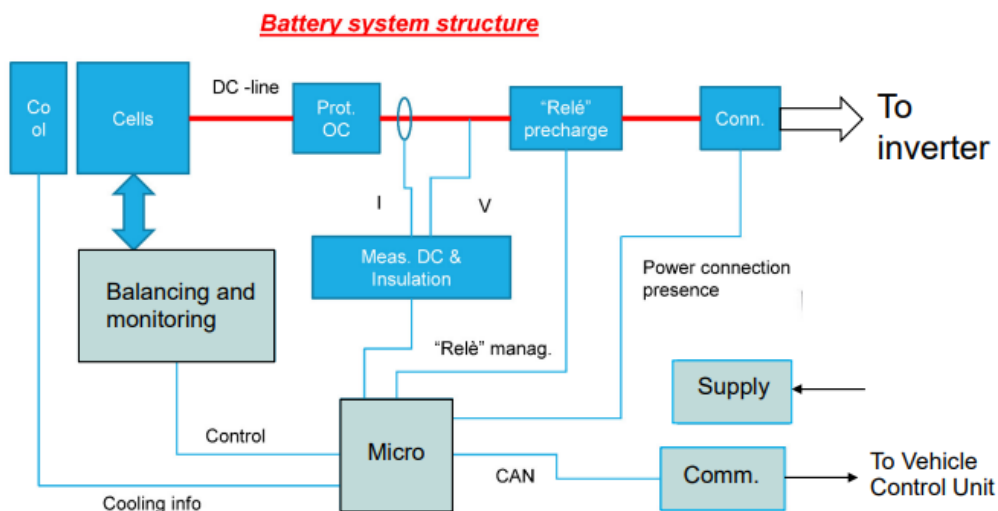


Figure 4. 27: Battery structure

As regard as the peak current that the battery has to face, a high level analysis has been performed. Firstly, it has been considered the electric motor power peak request of a motorbike that has one rear and two front suspensions: for each front suspension 1.7 kW are needed while for the rear 5.3 kW; the total power demand is equal to 8.7 kW. Therefore, being the power equal to the product between the current and the supply voltage, the peak current value is 181 A.

By means of the aforementioned features, the benchmarking analysis has been developed. Three LiFePO₄ batteries have been compared, all sold by PowerBrick+ manufacturer. The following table lists their main parameters, where two batteries in series are needed to have the desired rated voltage for the 24 V_{DC} solutions.

Table 4. 2: Battery pack solutions

	48 V – 25 Ah	24 V – 32 Ah	24 V – 50 Ah
Weight (kg)	12.6	7.8	11.8
Dimensions (mm)	260x168x212	197x166x169	260x168x212
Peak discharge current	270 A	150 A	350 A
Discharge current	50 A _{DC}	50 A _{DC}	50 A _{DC}

Finally, the 48 V – 25 Ah battery pack has been chosen, especially for weight and dimensions considerations. Its price is around 1300 € and the technical specifications are shown in the following figure.

Electric	Nominal voltage	51.2 V
	Nominal capacity	25 Ah
	Stored energy	1280 Wh
	Internal resistance	≤ 50 mΩ
	Cycles	>3000 cycles (see chart)
	Self discharge	< 3% per month
	Energy efficiency	> 98 %
Standard Charge	Charge voltage	57.6 V ± 0.8V
	Charge mode	CC/CV : Constant Current / Constant Voltage
	Continuous charge current / Maximum charge current	12.5 A / 25 A
	BMS charge cut-off voltage	59.2 V ± 0.4V
Standard Discharge	Instant peak discharge current	270 A ± 30 A (max 100mS)
	Continuous discharge current	50 A (2.56 kW)
	Maximum discharge current (< 30s)	100 A (5.12kW)
	BMS discharge cut-off voltage	40 V
Environment	Charge temperature range	0°C to +60°C
	Discharge temperature range	-20°C to +60°C
	Storage temperature	0°C to +50°C @60±25% relative humidity
	IP protection level	IP 65
Mechanical	Type of cells	Cylindrical
	Casing material	ABS
	Dimensions	L : 260mm x W : 168mm x H : 212 mm
	Weight	12.6 kg
	Terminal	M8 bolt

Figure 4. 28: Battery data [36]

It has the following important features [36]:

- High service life, with more than 3000 cycles.
- Deep discharge allowed up to 100 %.
- More than ten years calendar life.
- Excellent temperature robustness (−20 °C up to +60°C).
- Energy efficiency greater than 98 %.
- No memory effect.

4.2. ECU programming

This section deals with the electronic control unit programming and its integration into the power stage. In particular, the TI development kit is presented, with its features and connections; then, the control algorithm implementation and final calibration, depending on the components choices is illustrated.

4.2.1. *Texas instruments development kit*

The control board designed for the project is the Texas Instruments launchpad LAUNCHXL F28379D. It is a dual core 32-bit DSP optimized for motor control with multiple I/O. Its key features are:

- Fast serial connection for project debugging.
- CAN-enabled communication with transceivers.
- MATLAB/Simulink support for fast code generation.

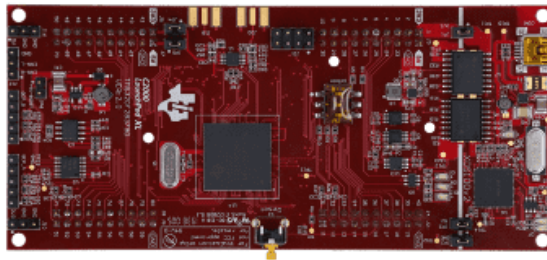


Figure 4. 29: TI development kit

This is a complete low-cost development board with a standardized and easy to use platform. It includes the TMS320F28379D microcontroller, USB connection for real-time debug and flash programming, 4x20-pin headers, programmable buttons and LEDs, supports for two BoosterPack plug-in modules, two encoder interface connectors and isolated CAN transceiver connector [37].

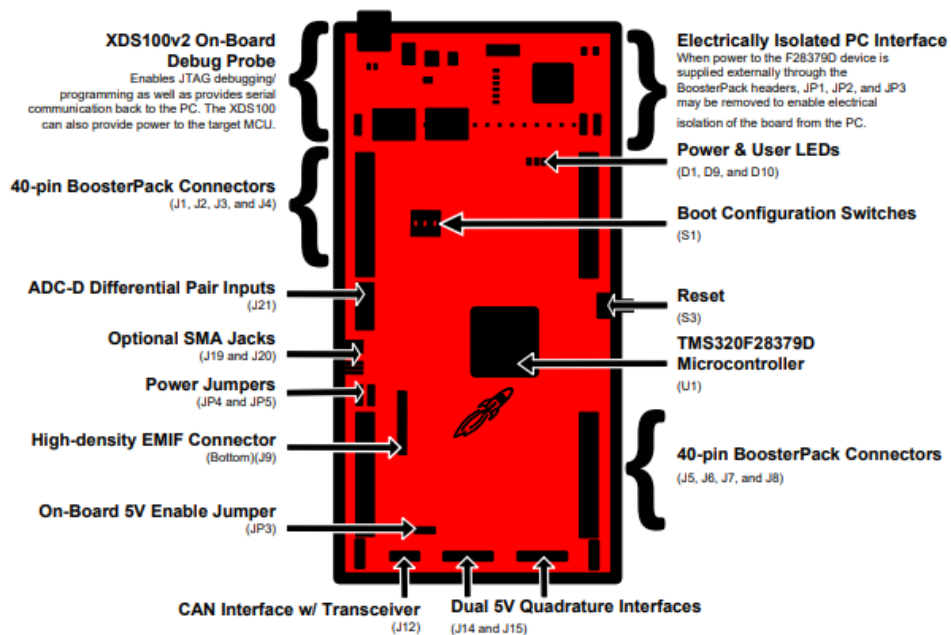


Figure 4. 30: Launchpad overview [37]

Additionally, the board has four independent 16-bit/12-bit ADCs all routed to the inverter headers. Regarding the power domain, the launchpad has several different configurations to enable USB isolation. The settings is performed through jumpers that provide different method for powering the device. As introduced in the sub-section 4.1.1 the control board $3.3 V_{dc}$ is fed by the DRV8323RS linear voltage regulator; in future works it will be necessary to separate the control domain from the power domain feeding the launchpad from an external buck regulator. Finally, this board has been also selected for its connection capability: In fact, it integrates connectors aligned in grids to allow easy and inexpensive development of add on drivers which can access all of the GPIO and analog signals [37].

4.2.2. *Implementation*

The following sub-section presents the implementation of the control algorithm into the ECU. Firstly, it is shown the test bench preparation, with the selected components and their communication. Successively, the design and calibration of the control system through the Motor control blockset of MATLAB/Simulink is illustrated on the basis of what described in the section 3.2.

Test bench

The Figure 4.31 shows the test bench utilized during the final phase of the thesis work to validate the control system developed and the components selected, extrapolating proper results by monitoring different working points of the RRSA and EHA electric motor. The depicted and chosen devices are:

- 3-phase TI inverter DRV8323RS, modified version (sub-section 4.1.1).
- TI development kit LAUNCHXL F28379D.
- RRSA and EHA SPM synchronous motor.
- Power supply.

All these components have been properly connected to make them communicate. Cables are used to match the motor and the inverter corresponding three phases.

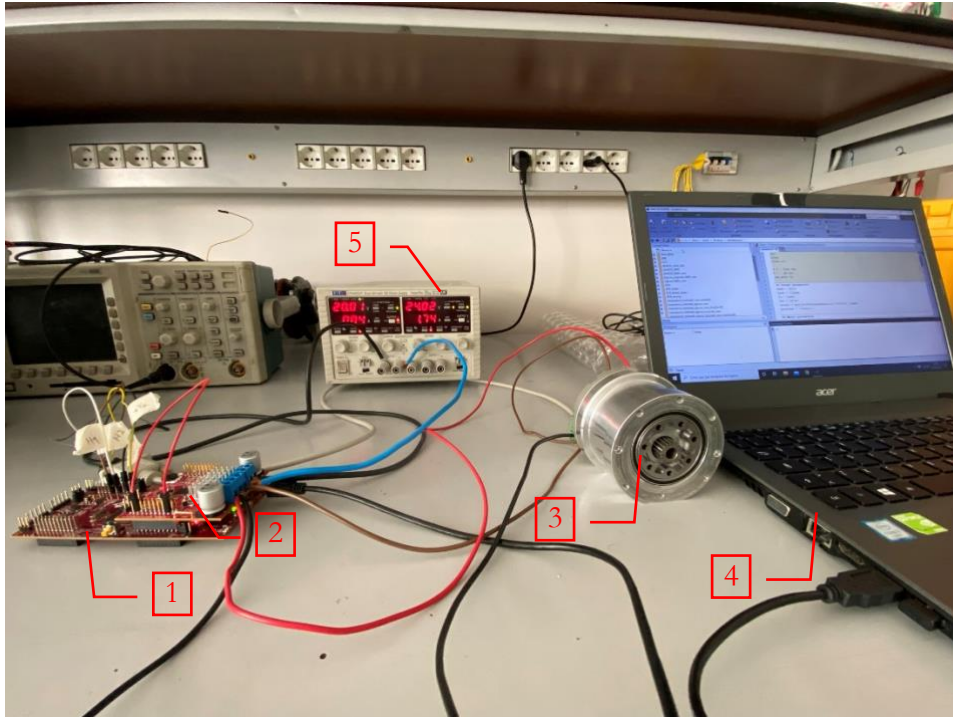


Figure 4. 31: Test bench. LAUNCHXL F28379D (1), DRV8323RS inverter (2), SPM e-motor (3), laptop (4), power supply (5)

Other two cables provide the ground and $+V_{dc}$ connection of the power supply with the inverter. In particular, as in the following figure, the power supply is set to feed 20 V_{dc} voltage by means of the output one port: this value has been selected in order to test the prototype motor in the FW region without the need to reach too high speeds.



Figure 4. 32: Power supply

Additionally, proper interfaces are established for the launchpad with the inverter, the motor and the laptop.

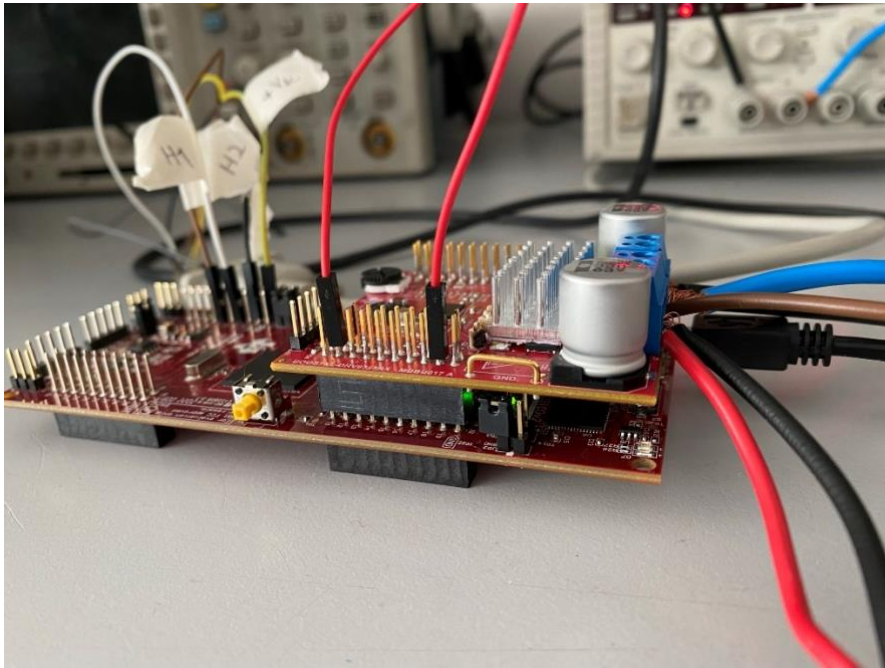


Figure 4. 33: Launchpad connections

The motor integrates two linear Hall effect sensor Allegro A132x [28]: they are powered by the launchpad $3.3 V_{dc}$ which accepts on its ADC ports their outputs. Moreover, the development kit is assembled with the driver to pilot its PWM pulses and is in communication with the laptop, through a USB cable, implementing host-target communication provided by the Motor control blockset.

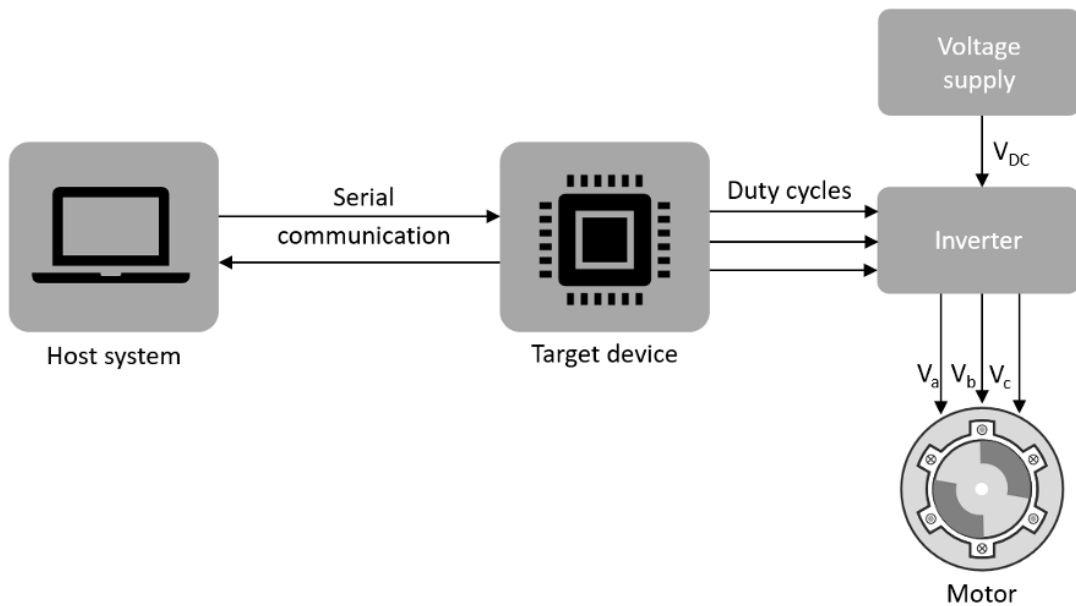


Figure 4. 34: Host-target communication

In particular, by means of a communication interface between the host model and the target model it is possible to control the motor and monitor the feedback. This can be done thanks to modules that enable serial communication in order to monitor, control and customize the motor operation in real time. The host model is a user interface for the controller hardware board; it commands, controls and exchanges data with the target hardware. Before running it, the deployment of the target model on the launchpad has to be made. In fact, this latter runs on the controller hardware board.

Thus, the steps that have been made to design a compact and fast C code for the target model are illustrated in the following lines. The implementation consists of the same control architecture and calibration used during the simulation stage, described in the subsection 3.2.2, since the controlled SPM motor is the same, with its parameters in the subsection 3.2.1. Therefore, only the additional features and changes in the calibration are presented here.

Limitations

The first functionality difference is in the limitation of the variables. In particular, during this prototyping phase the DC-link voltage v_{dc} is set to **20 V**: this yields to a maximum voltage v_{max} equal to **11.5 V** (eqn. 2.16). In addition to that, the maximum current i_{max} is limited at **9 A**. This comport a significant change in the flux-weakening operation: the motor never reaches the machine characteristic current, thus, the strategy becomes the one depicted in figure 2.12. Of course, also the current saturation module is modified (fig. 3.9), with the i_d current range between **0** and $-i_{max}$. Finally, the speed input is bounded between **-5000** and **5000 rpm**.

Speed loop

In this case, the motor is controlled in the speed, through an external speed loop running at one tenth of the switching frequency i.e., at **2 kHz**. This is done because the prototype runs without any load, so this additional loop is needed to make the rotor spin. Therefore, the input of the control system is the speed reference in **rpm**; then, it imposes the needed current space vector to the drive through the rest of the strategy, in order to win the inertial and friction forces. Furthermore, the speed controller consists of a PI regulator that from the speed feedback computes the reference i_q current.

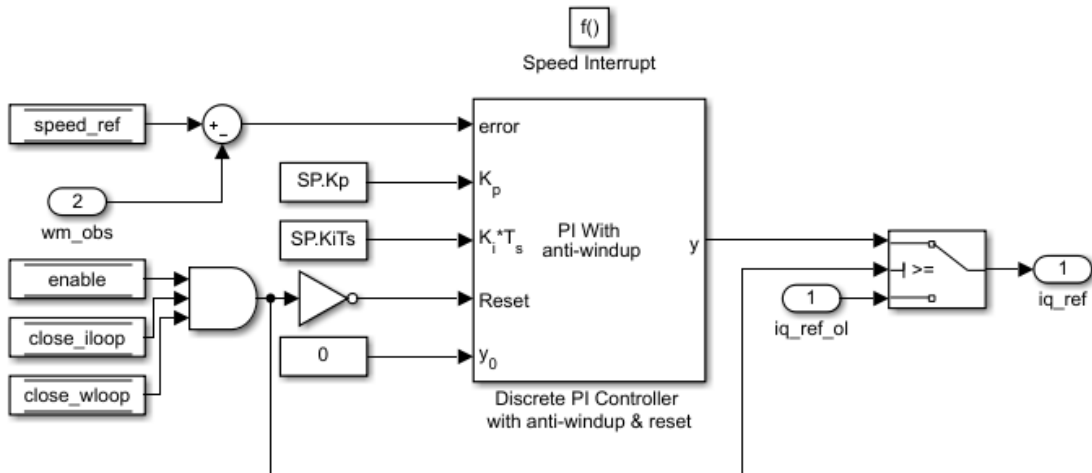


Figure 4. 35: Speed loop

The proportional and integral gain are respectively 0.001 and 0.08 while the maximum absolute value of the output is i_{max} .

Open-loop to closed-loop transition

In the previous figure it is possible to notice three commands: they are inserted to implement the enable, to close the current loop and close the speed loop. In fact, once given the enable, the control algorithm can run in open-loop controlling only the current with an imposed angle through a position generator module.

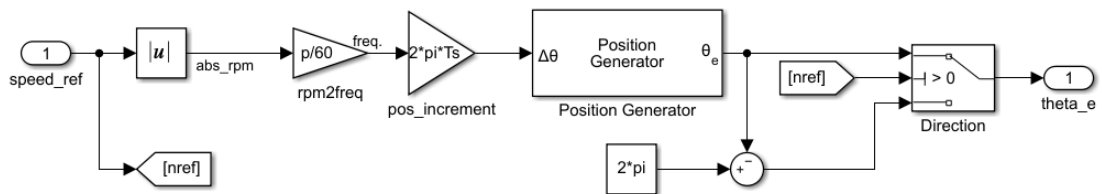


Figure 4. 36: Position generator

This block generates a position ramp of required frequency, permitting to impose the desired reference speed. The output is the electrical angle that feeds the current control. However, being this an open-loop, the angle can have some misalignments; thus, this strategy is used only to start the motor and then the transition to the closed-loop system is performed.

Rotor position

To estimate the rotor position the control system feature both the SMO or the flux observer, for sensorless control, and the two linear Hall effect sensors mounted on the motor, for sensed control.

Regarding the observers, the features and the calibrations are the same of the simulation, except for the DC component removal (fig. 3.5) that has been not necessary for the real plant. Additionally, the flux observer needs an external estimation of the speed to provide the feedback to the speed loop. This is implemented through the following speed measurement block, that computes the mechanical speed from the angular position.

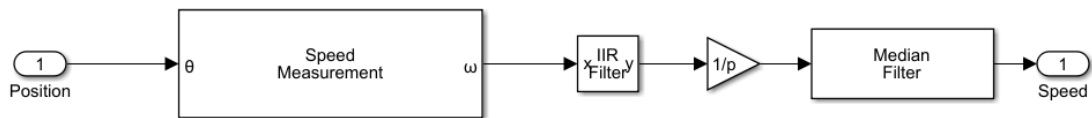


Figure 4. 37: Speed measurement

Its output is properly filtered by means of an infinite impulse rejection module, with filter coefficient set to **0.02** (eqn. 3.6) and a median filter.

For what concern the sensed control, the strategy is shown in the following picture.

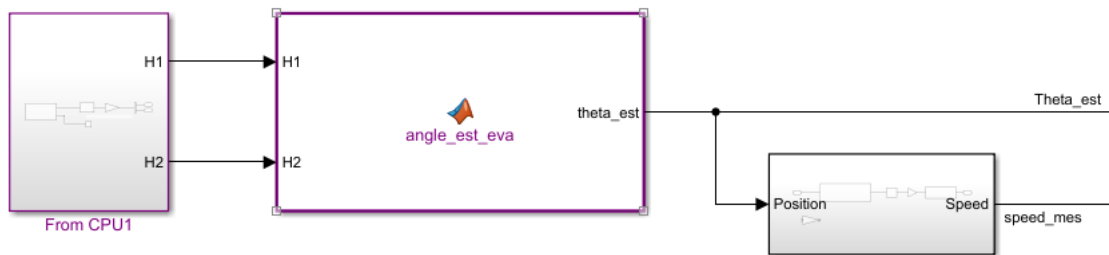


Figure 4. 38: Hall sensor logic

In particular, the two voltage signals are read from the launchpad ADC pins; successively, these feed a suitably pre-calibrated lookup table which outputs the electrical angle estimation filtered by means of a medial filter. Also in this case, the speed measurement module is then used.

Current measurements

The a and b-phase current feedback for the Clarke and Park transforms are obtained from other two launchpad ADC pins. The measurements are inevitably affected by the hardware

offset and the ADC resolution errors. For this reason, the values read from the pins are properly processed, cancelling the offset and multiplying the result by the ADC gain, to obtain the voltage from the ADC counts.

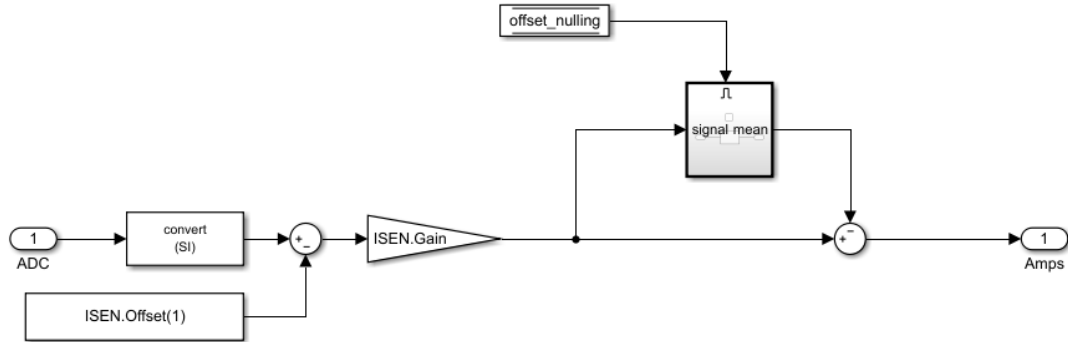


Figure 4. 39: Current measurement

This can be performed manually, by setting a proper fixed current offset value in a data store memory. On contrary, to achieve a better precision, a command is inserted to calculate the exact value of the offset. It is activated one time when zero current is requested: then, it computes the mean value of the measured current and stores it; the stored value is the offset that will be successively removed.

Current controller

The simulation current control structure is used (fig. 3.7). The PI calibration of the current loop is recalled:

- Current control bandwidth $\omega_c = 1000 \cdot 2\pi = 6283 \text{ rad/s}$.
- Proportional gain $k_p = 2.2 \text{ V/A}$.
- Integral gain $k_i = 427.2 \text{ V/As}$.

There are small differences in the FWC tuning: as shown in the following table, the chosen parameters are different depending on the rotor position measurement strategy.

Table 4. 3: FWC calibration

	Hall	SMO	Flux observer
$k_{ifw} \text{ [A/Vs]}$	3.1	6.25	12.5
$k_{pfw} \text{ [A/V]}$	0.03	0.03	0.06
IIR filter	0.001	0.01	0.01

The sliding mode observer and the hall sensor provide a faster closed loop response than the flux observer. Thus, their FWC bandwidth is lowered by proportionally decreasing the integral and proportional gains. Additionally, the integral gain and filter coefficient of the Hall sensor FWC are further reduced due to the increased noise that is registered in the Hall sensor angle estimation at high speeds. In addition to that, the maximum amplitude reference voltage as input of the FWC PI regulator is set to $0.9 \cdot v_{max}$ for all the estimators; this means that the FWC is activated when the voltage reaches 10.39 V. A lower value is selected with respect to the simulation parameter in order to avoid saturation problems coming from the hardware noise.

Space vector generator

The space vector modulation is the last functionality of the controller. The strategy is the one presented in the sub-section 3.2.2, except for the final stage, where there are the interface blocks to communicate with the driver.

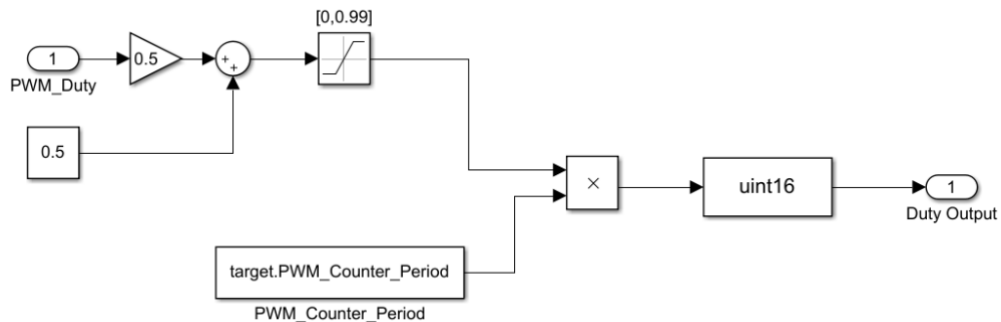


Figure 4.40: Duty-cycles scaling

In particular, the interface blocks that command the PWM pulses of the inverter expect the duty cycle value to range from zero to the period counter register value; therefore, the duty cycles are multiplied by this value.

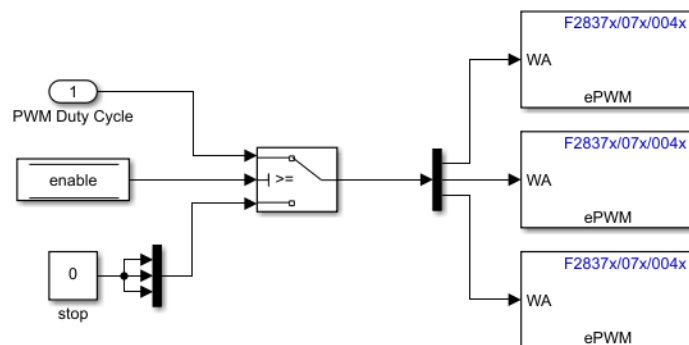


Figure 4.41: PWM interface blocks

Interrupt service routine

Finally, once developed the control system structure implemented in the target model, the interrupt service routine of the development kit board has been properly calibrated in order to avoid overruns, permitting to the microcontroller to execute all the tasks. The following figure shows the event sequence, interrupt trigger and software execution time for the control algorithm in the target hardware.

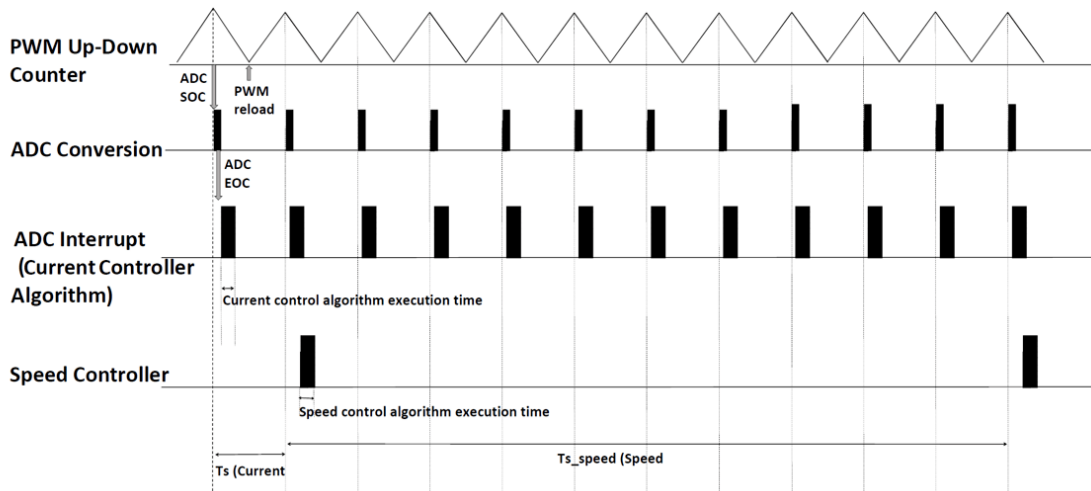


Figure 4. 42: Task scheduling

The current controller and the measurements are performed synchronously to the switching frequency, at 20 kHz. Together, they represent the first task designed in the interrupt service routine (ISR), the one with most important priority. In particular, the processor peripheral PWM triggers the start-of-conversion event for the ADC module when the PWM counter value is equal to the PWM period. Successively, the ADC module converts the sampled analog signal into digital counts and triggers the end-of-conversion event; at the end this entails the ADC interrupt that schedules the current controller. The second priority task is given to another implemented routine designed for the communication with the host model. It permits to receive and send data from and to the host machine and is executed at 4 kHz. Finally, the lowest priority is provided to the speed loop controller, that as previously stated runs at 2 kHz. These tasks are all implemented in the first CPU: to be sure that the board is able to run all the steps in time, it has been monitored the heaviest task time execution i.e., the one with the current controller and the measurements, by means of processor-in-the-loop testing. Its maximum registered execution time has been equal to $2.2e5$ ns; this corresponds to a maximum CPU utilization

of 43.8 %. It can be concluded that the ISR of the first CPU is correctly implemented. Additionally, the second CPU has been utilized only to perform the Hall sensor angle estimation. In fact, the use of the lookup table burdens a lot the system and positioning it on another CPU avoids any risk of overruns; it is executed synchronously to the switching frequency and its duration is of $3e5$ ns.

4.3. Results

In this section are presented the main results obtained by controlling the RRSA and EHA motor in different operating condition, through the test bench in figure 4.31, in order to validate the control algorithm and the power stage components.

Once developed the target model, it has been deployed to the target hardware by generating the C code; the system uses serial communication to download the specific file to the control board and runs the downloaded algorithm in the hardware with the host model in the figure below.

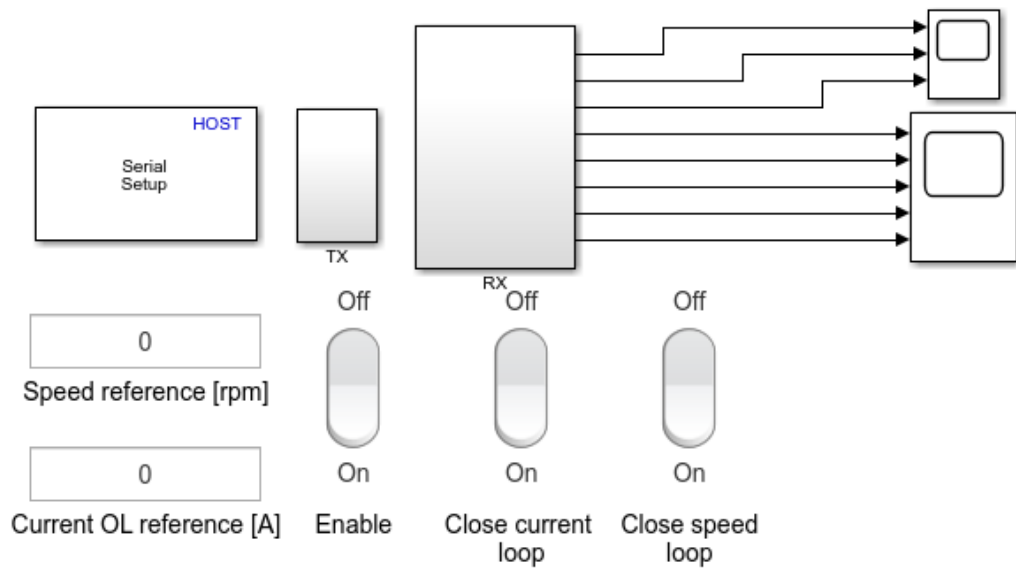


Figure 4. 43: Host model

4.3.1. Open-loop

The first test has been performed in open-loop, to check the functionality of the current loop controller at lower speeds, without exceeding the constant torque region.

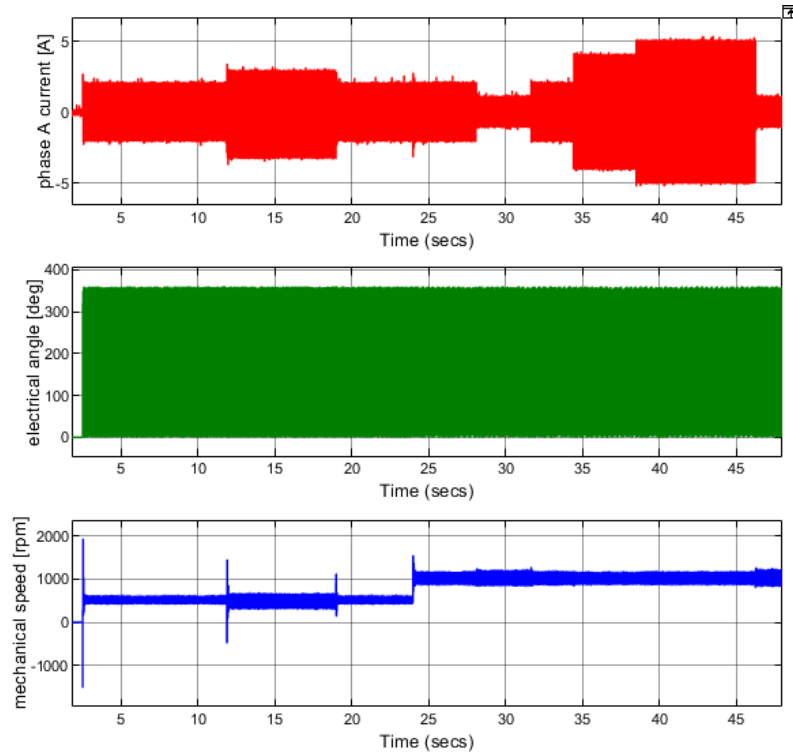


Figure 4.44: Open-loop test

The frequency of the position ramp generator imposes a speed of 1000 rpm with good precision (third plot). The first plot shows the a-phase measured current which, as visible in the figure below, is a clean sinusoidal waveform.

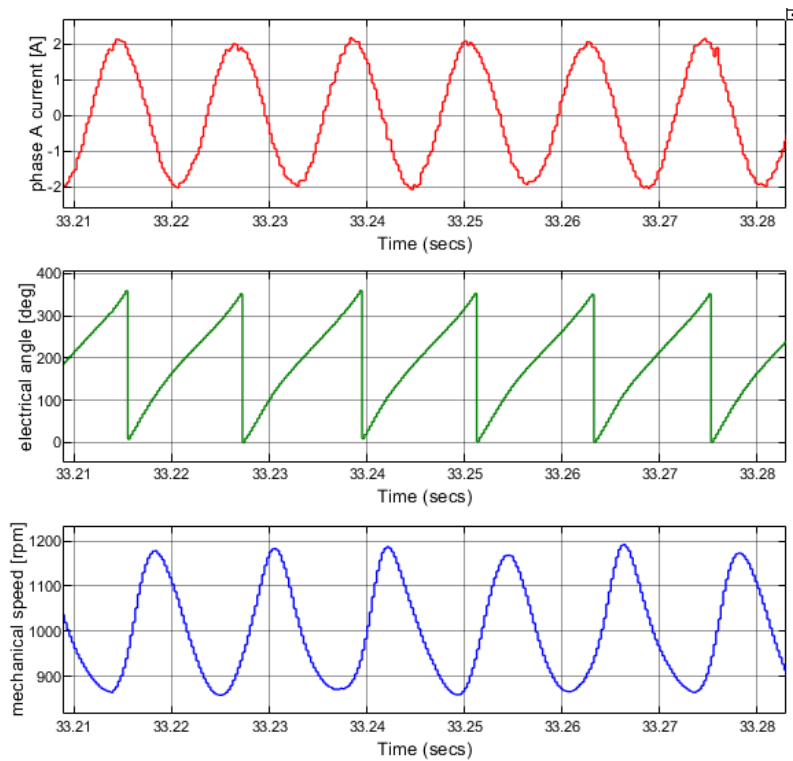


Figure 4.45: Open-loop test, zoom

In the next picture is shown a step change in the reference current from 2 A to 4 A properly adempted.

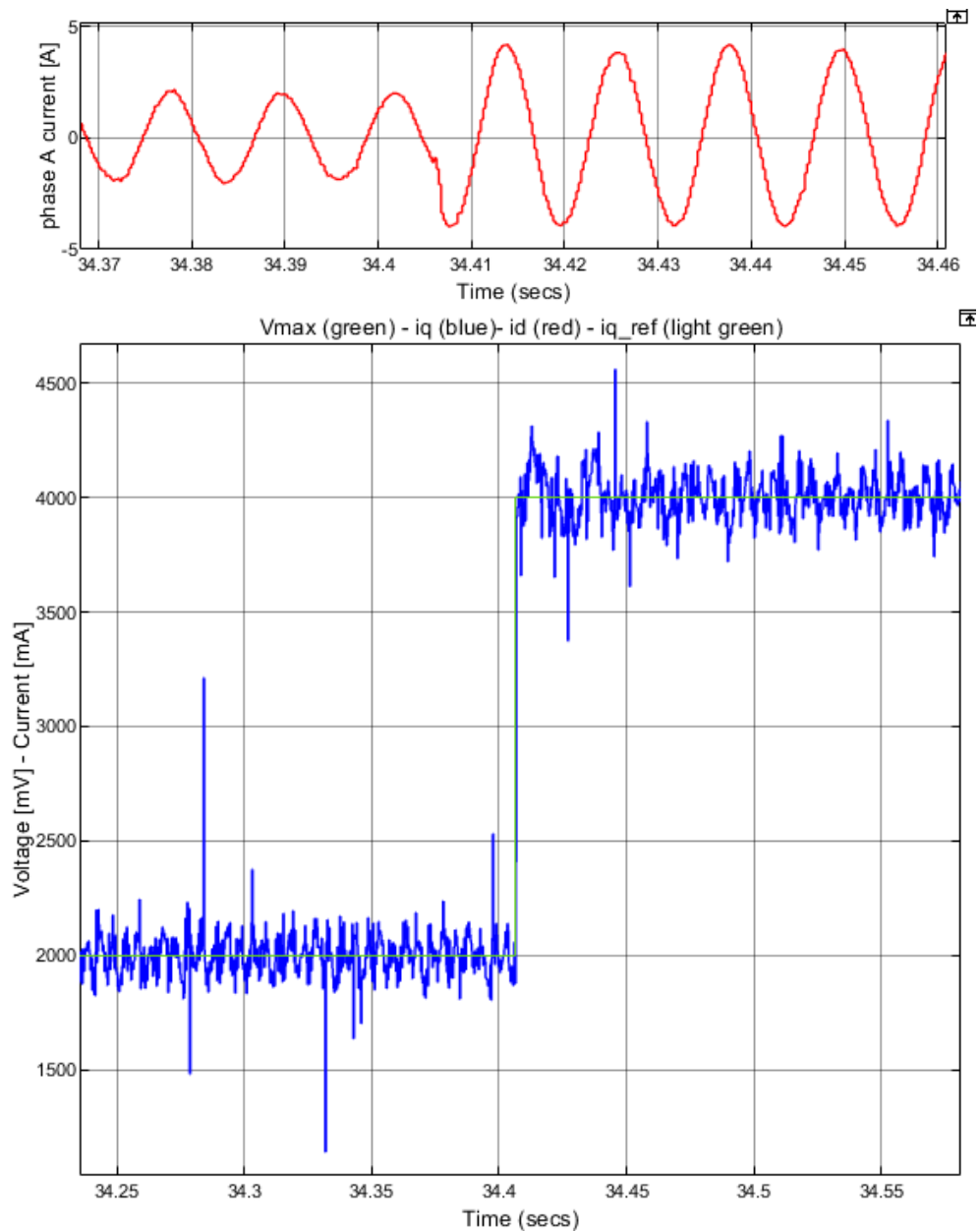


Figure 4. 46: Open-loop test, current reference step

A most severe step change, from negative to positive value of the reference current, is shown, with correct control of the system.

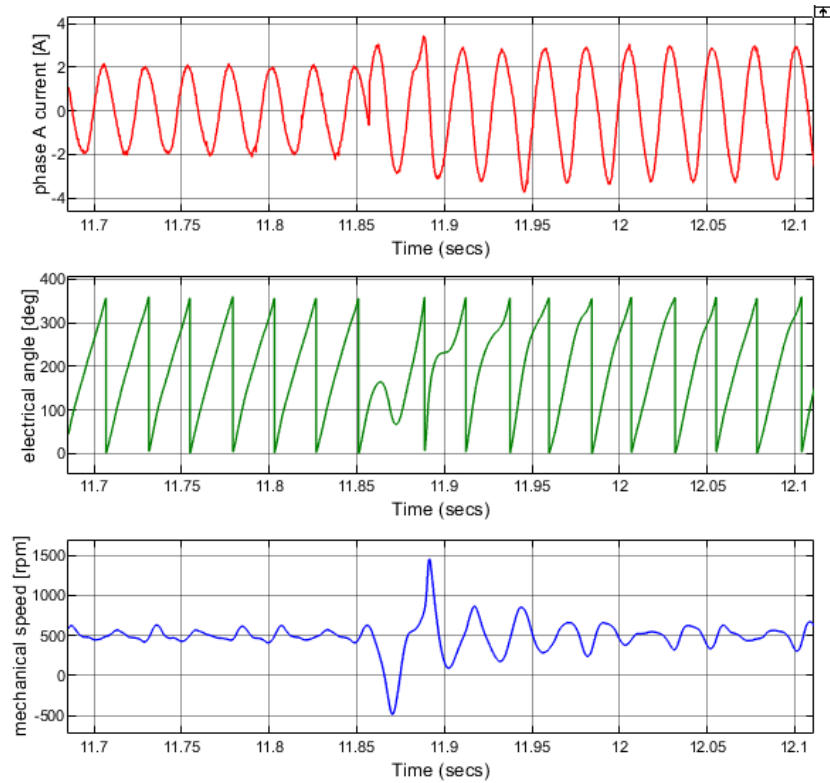


Figure 4. 47: Open-loop test, current reference step negative to positive

The overall electrical variables behaviour during the positive region of the test are depicted below. It is highlighted that in the constant torque region the d-axis current is set to zero.

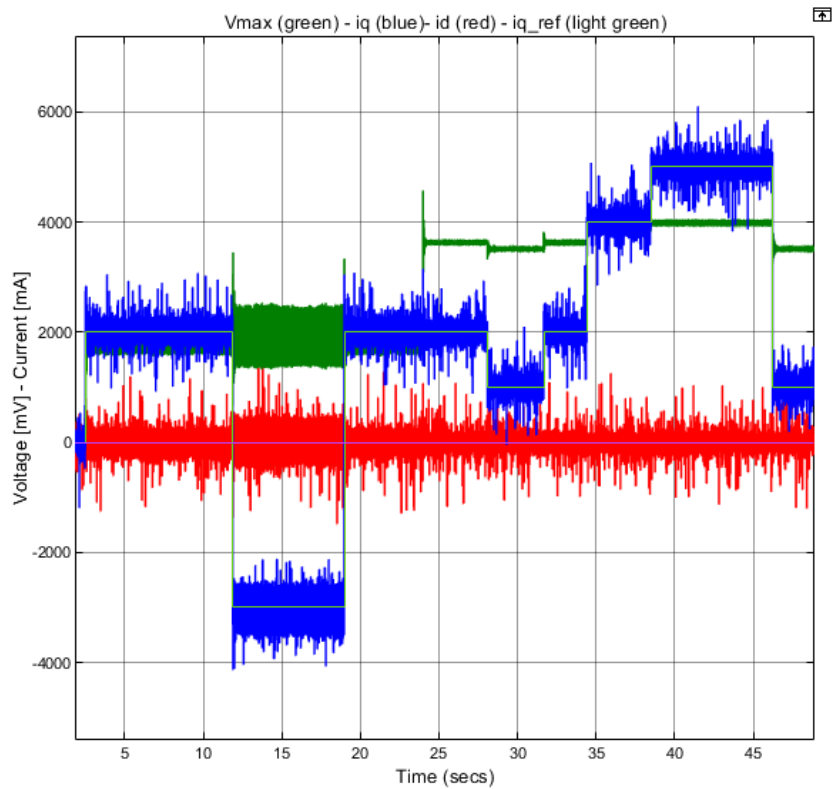


Figure 4. 48: Open-loop test, electrical variables

4.3.2. Flux observer

The following test is performed in sensorless control, through the flux observer, running the motor also at higher speeds with the need of the flux weakening controller.

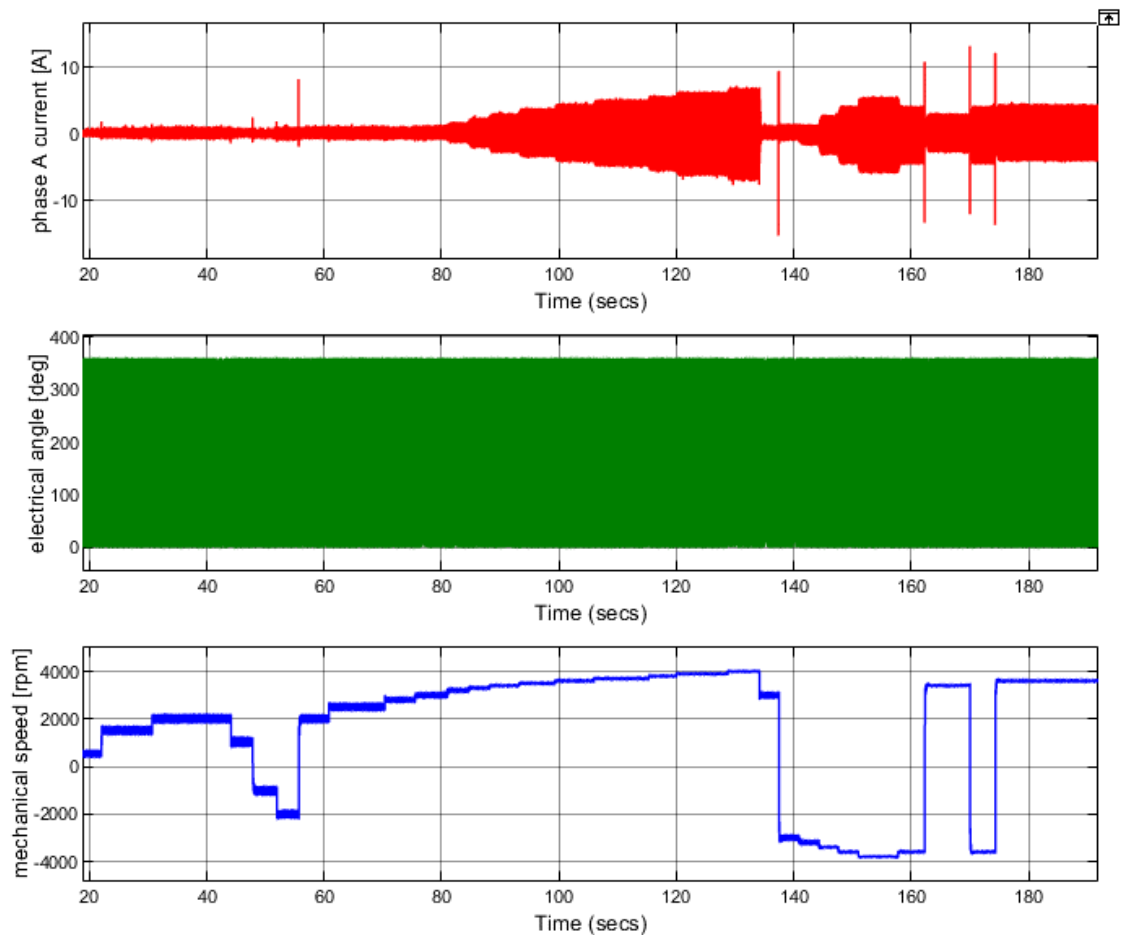


Figure 4. 49: Flux observer test

It can be seen that the motor has been driven with different speed reference values through step changes in alternate way, in a range between $[-4000, +4000]$ rpm. During all the operation, the control of the drive is perfectly maintained and the system responds reactively.

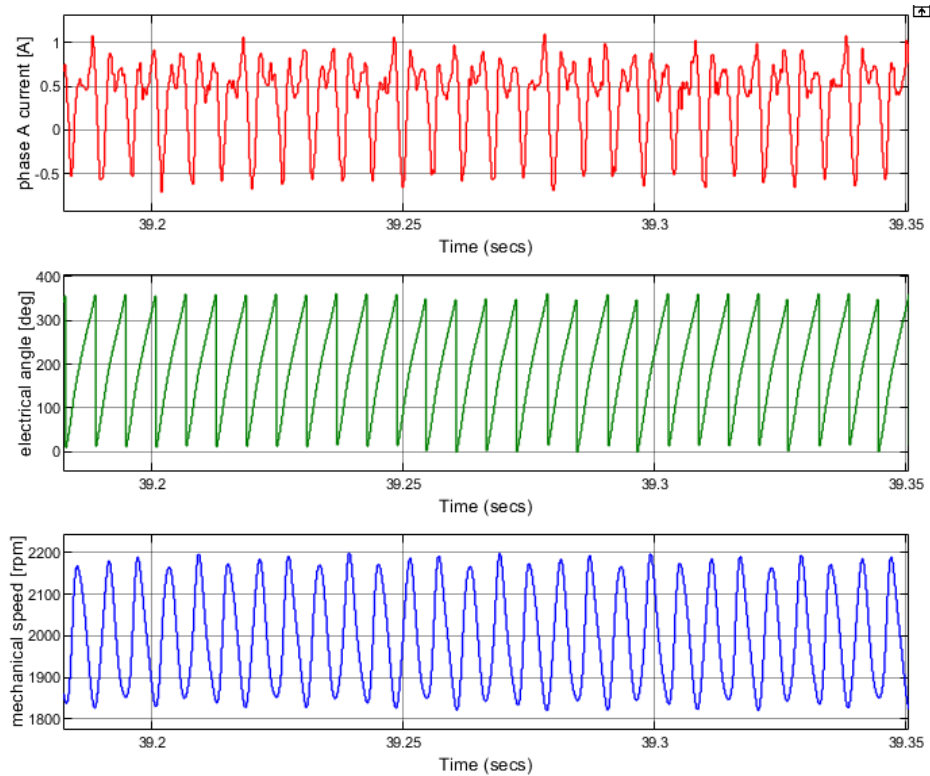
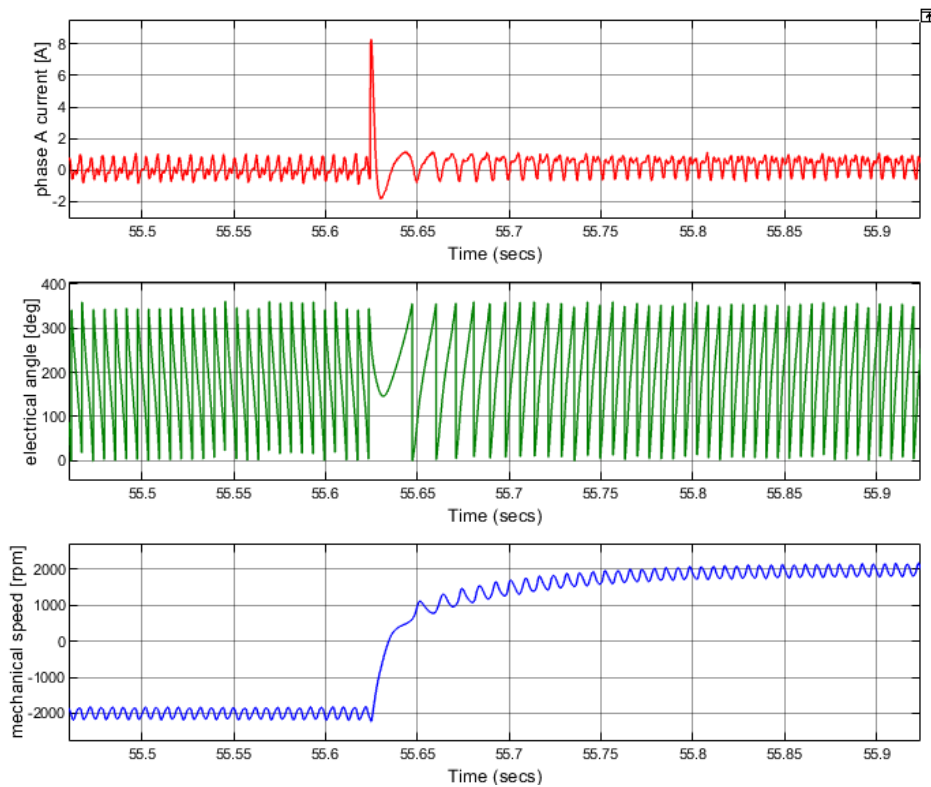


Figure 4. 50: Flux observer test, zoom

The angle estimation is quite good, although the current presents some noise and harmonics, thus, it is not perfectly sinusoidal. The speed measurement also oscillates but what is important is the mean value since these oscillations are mechanically filtered.



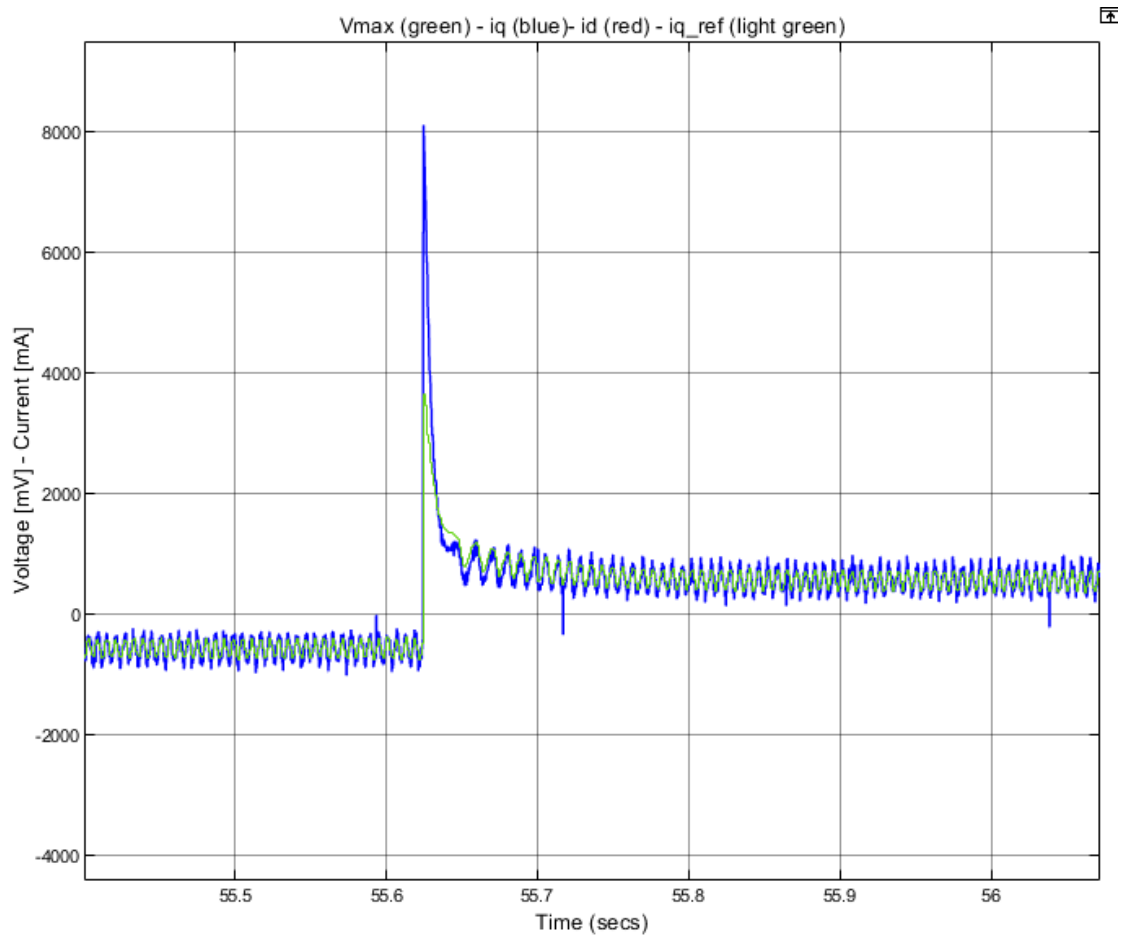


Figure 4. 51: Flux observer test, speed step change

The previous pictures presents a step change in the reference speed from negative to positive 2000 rpm to validate the speed loop response: this generates a reference i_q current properly imposed. In the next figure, the electrical variables values obtained during the test are illustrated. It is possible to see the negative d-axis current generated during the FWC operation, when the voltage is correctly limited to its maximum value.

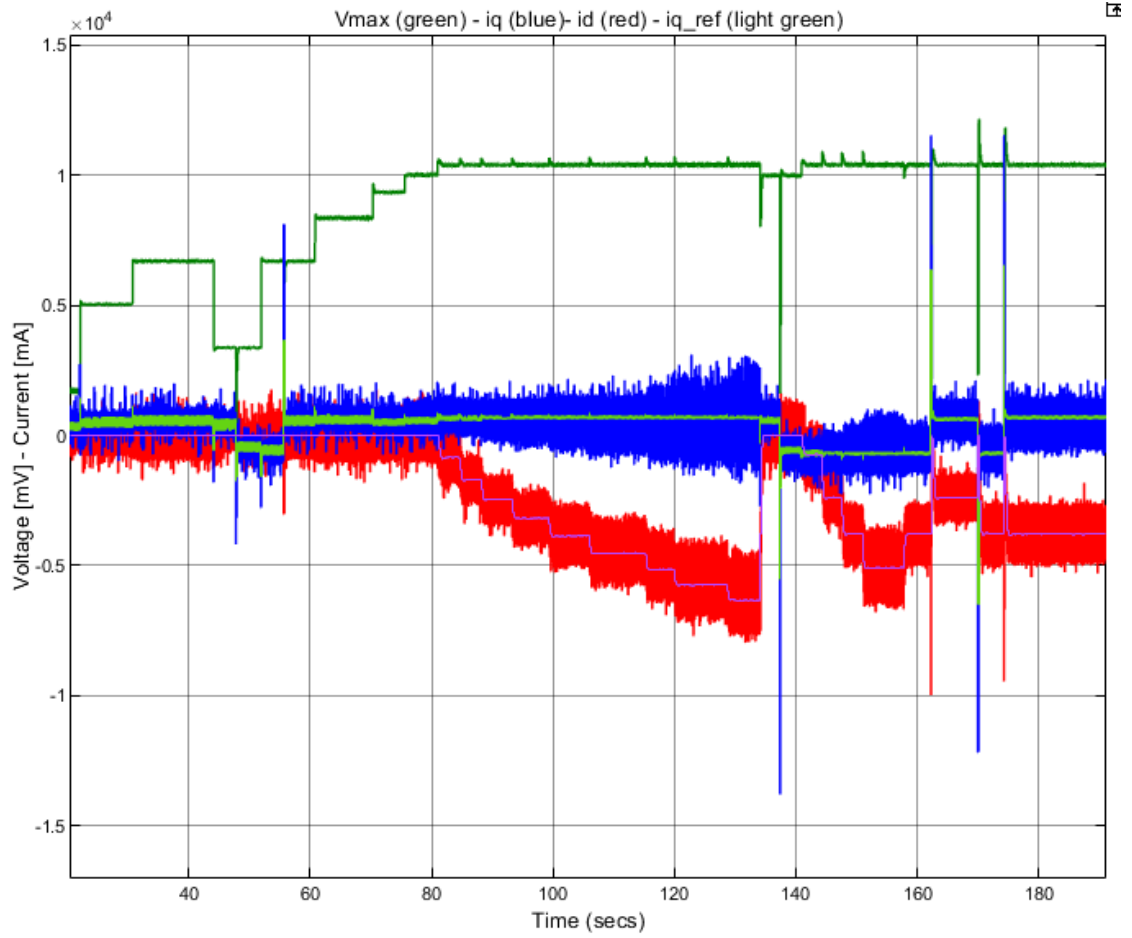


Figure 4. 52: Flux observer test, electrical variables

Following, the FWC behaviour during some positive incremental speeds is shown. It is possible to state that the field-weakening strategy maintains the control of the motor by properly rising the d-axis negative current as the speed increases.

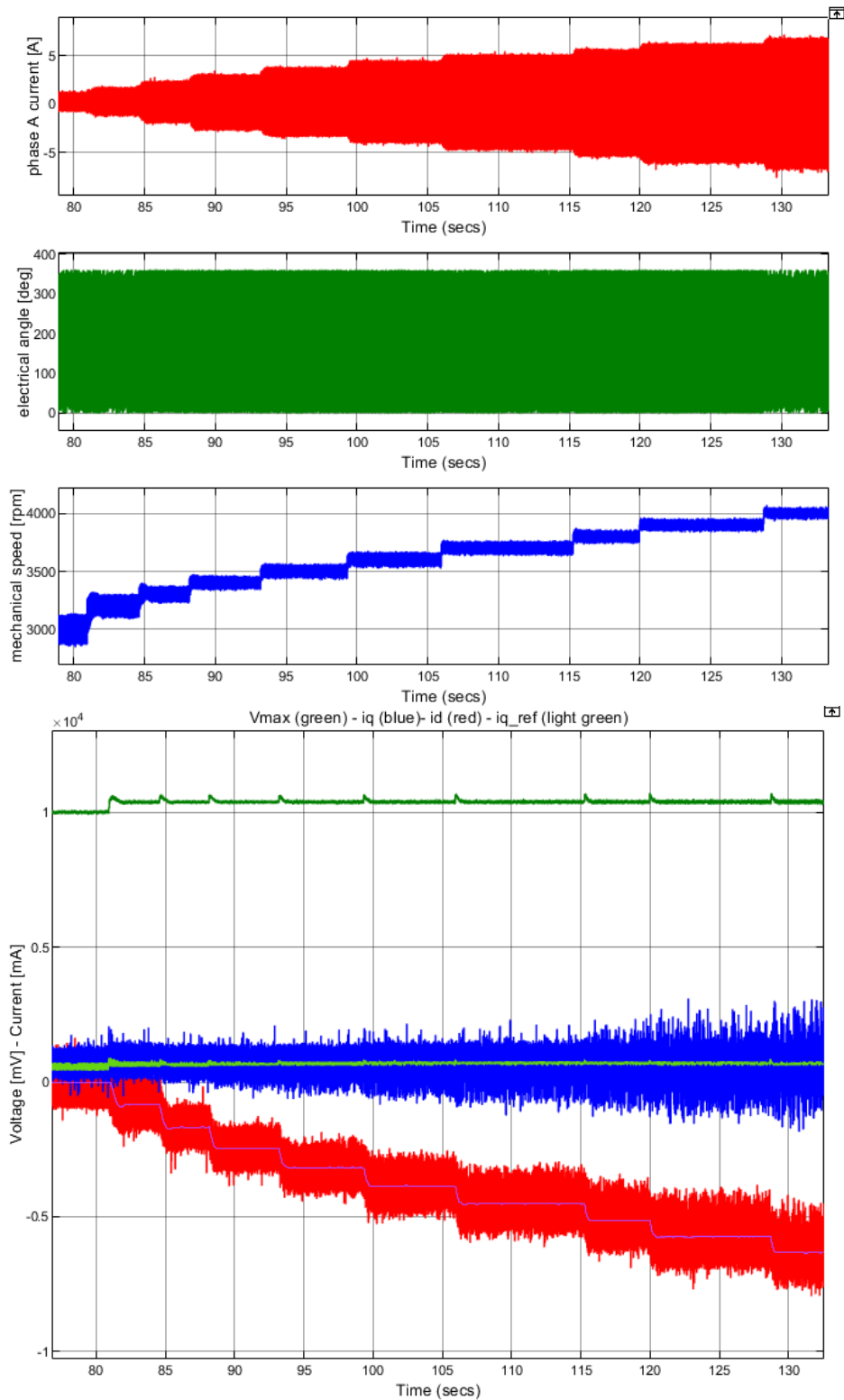


Figure 4. 53: Flux observer test, FWC positive change

In the next pictures, the same behaviour is presented for negative speed, validating the control also for the regenerative phase.

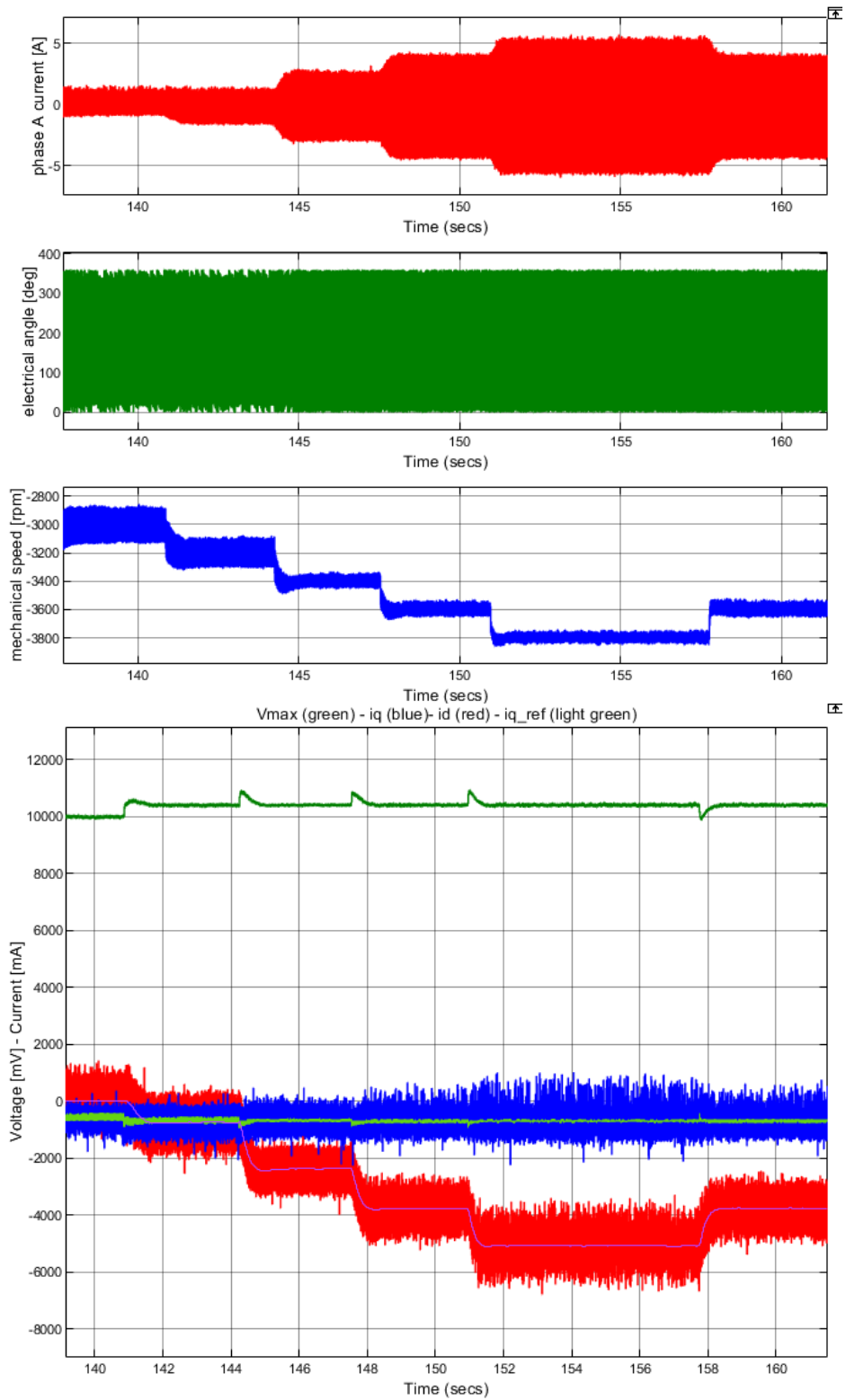


Figure 4. 54: Flux observer test, FWC negative change

Finally, the control system has been tested with a drastic change between -3500 rpm and 3500 rpm showing an accurate response i.e., small oscillations and rise time.

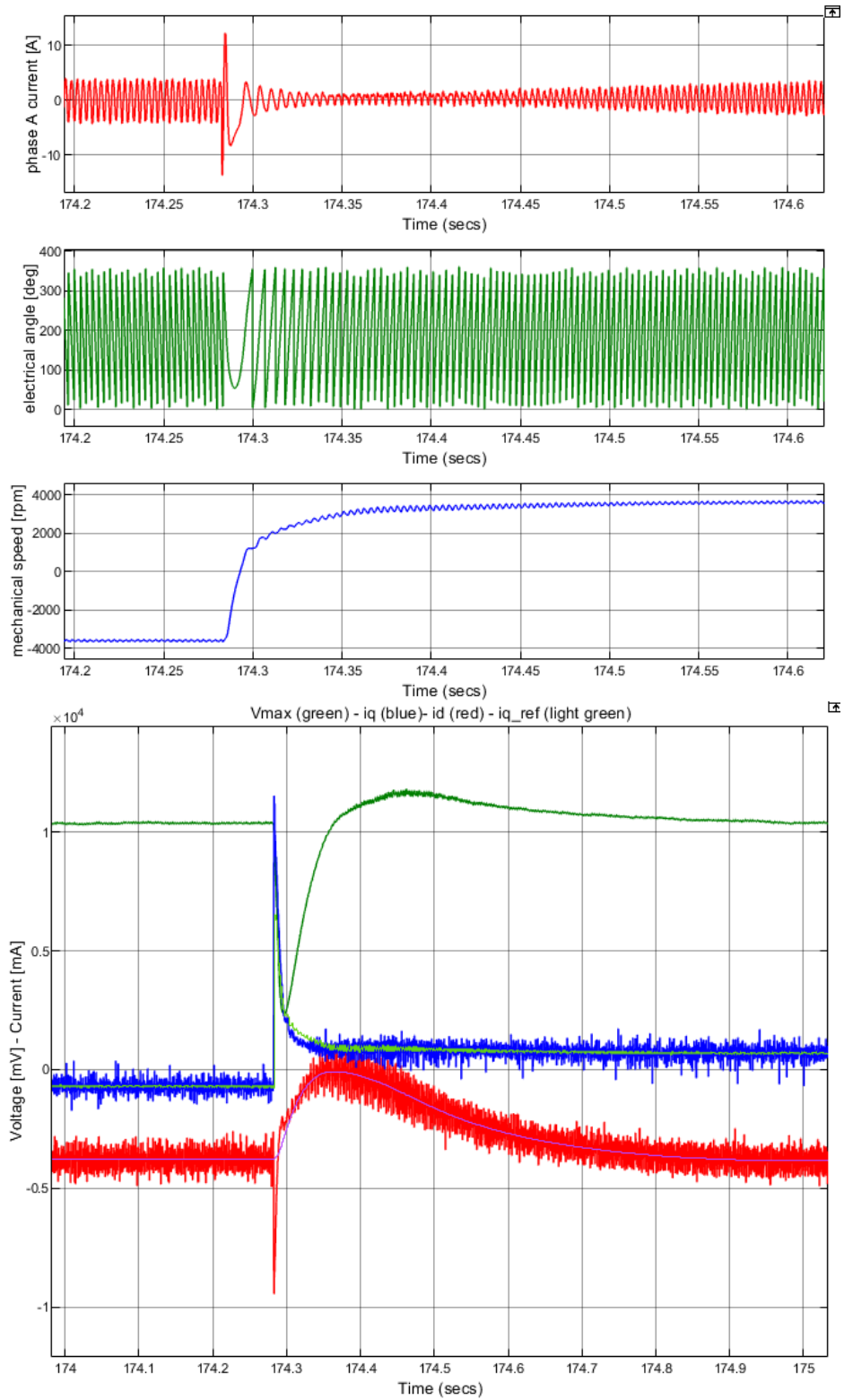


Figure 4. 55: Flux observer test, FWC negative to positive change

4.3.3. Sliding mode observer

The third test has been made to validate the control calibration using the sliding mode observer. Also in this case the control is perfectly maintained, with some oscillations during positive to negative transitions.

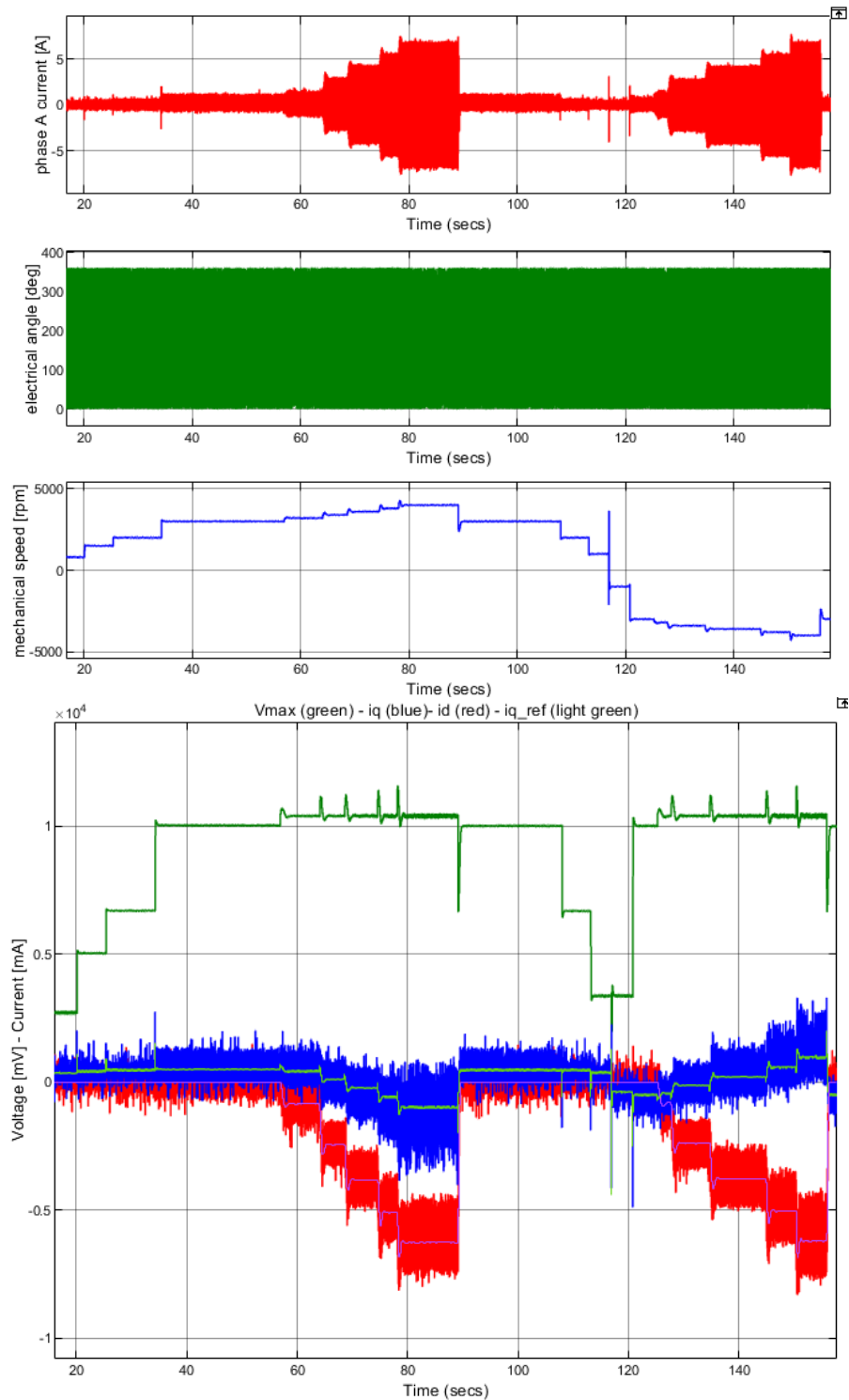


Figure 4. 56: SMO test

The angle estimation seems cleaner than the flux observer one, comporting a good sinusoidal current shape.

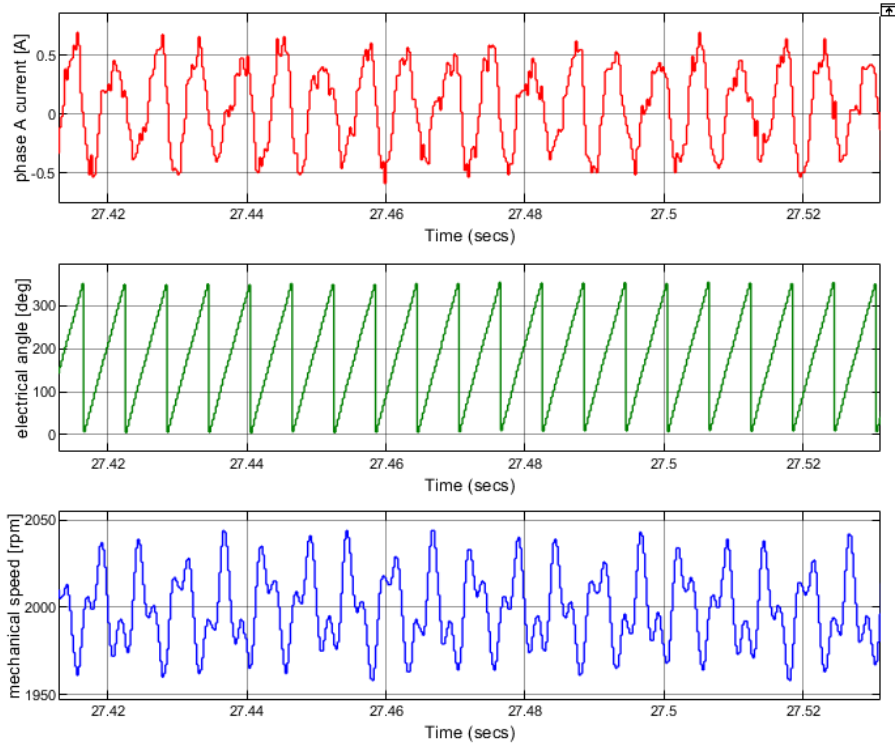
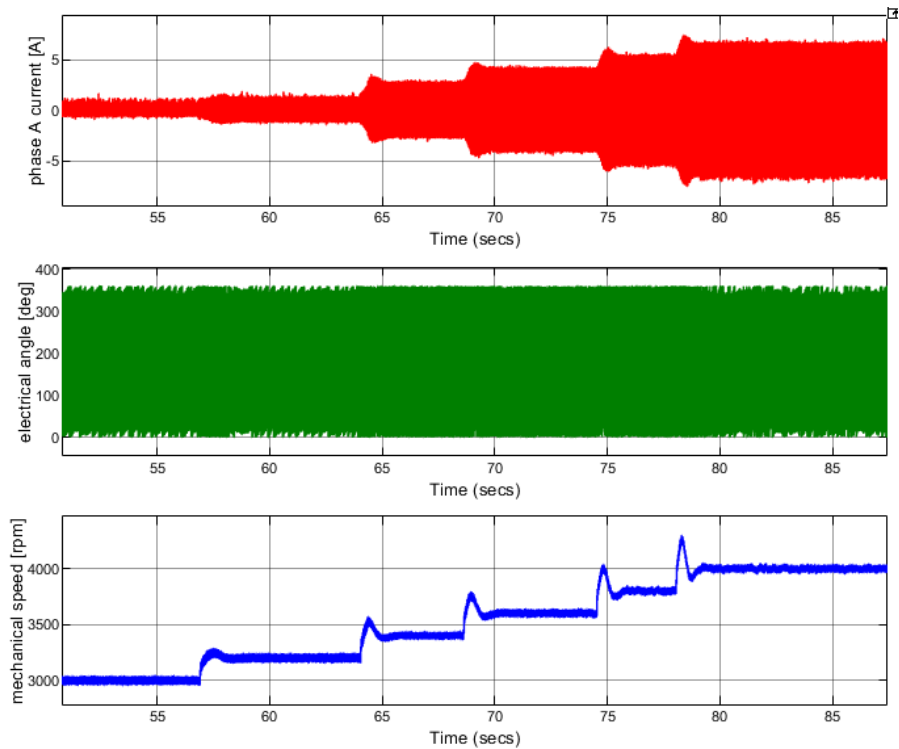


Figure 4. 57: SMO test, zoom

The FWC operations are presented below.



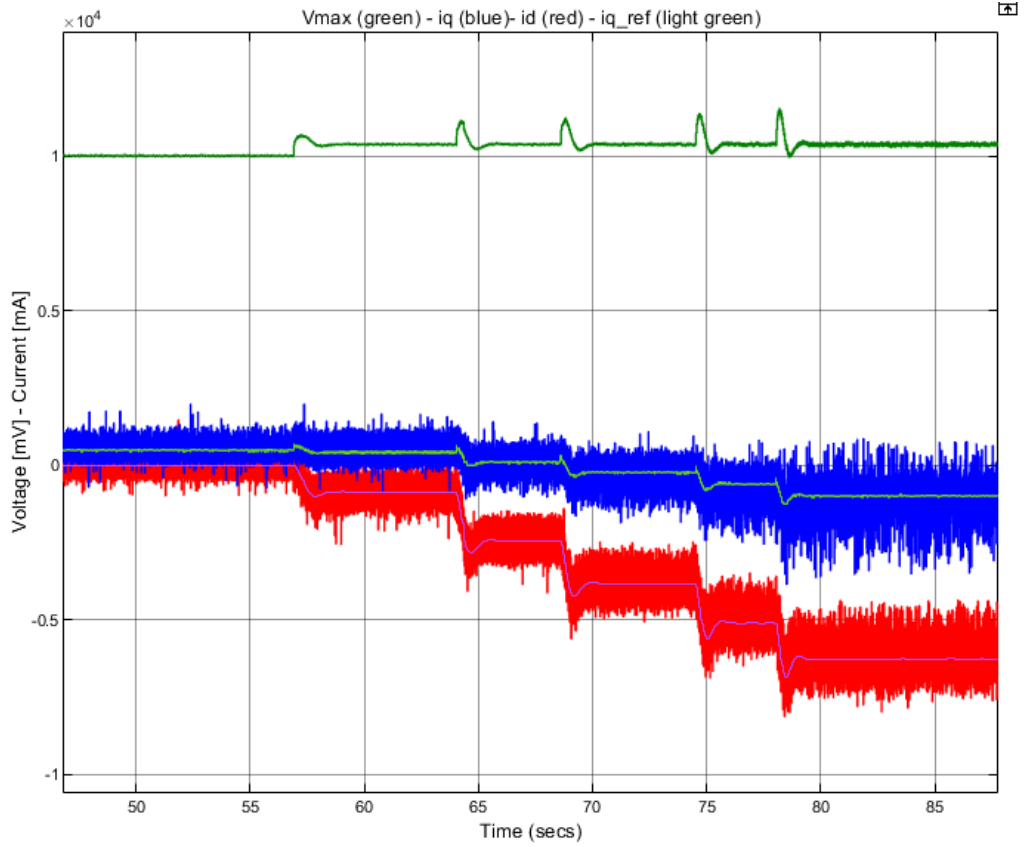
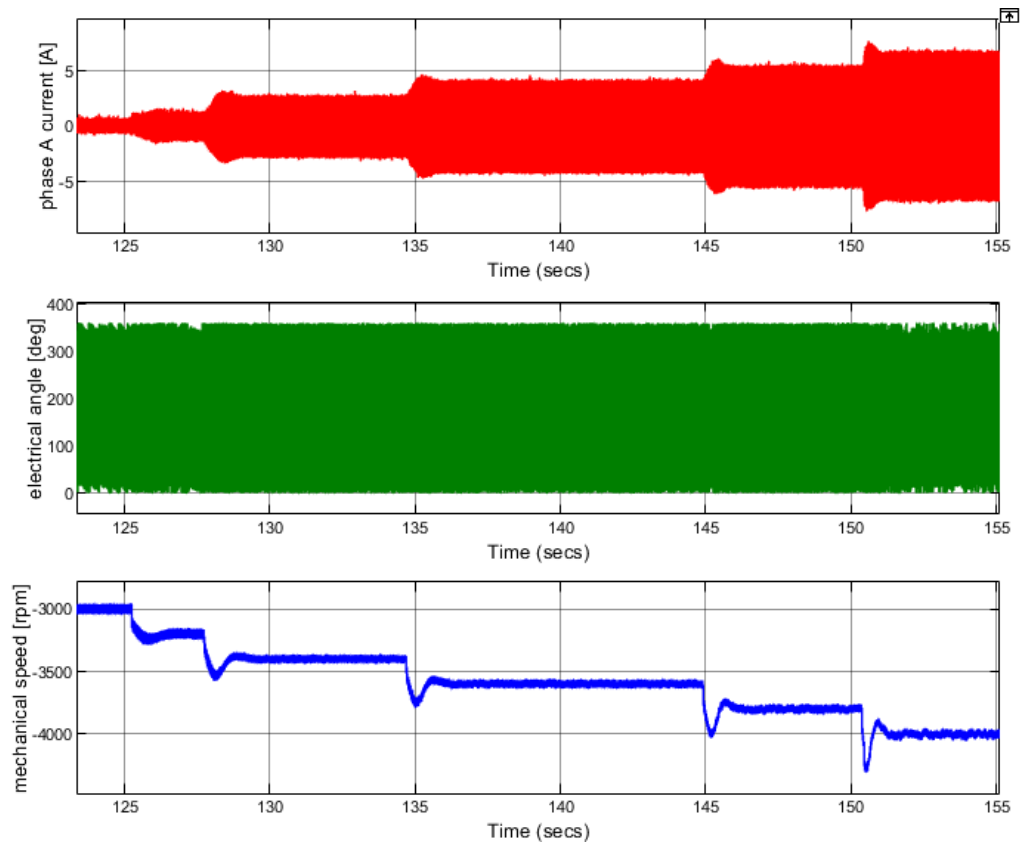


Figure 4.58: SMO test, FWC positive change



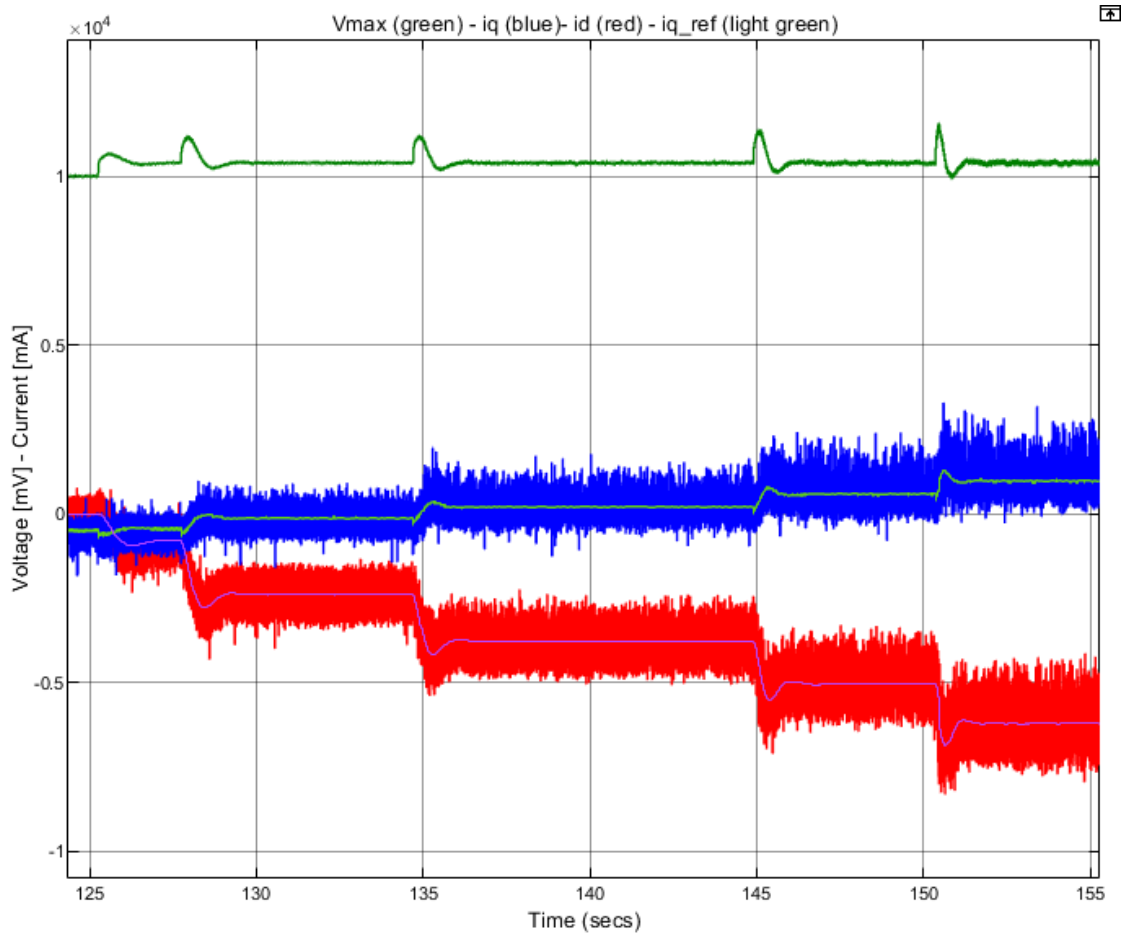
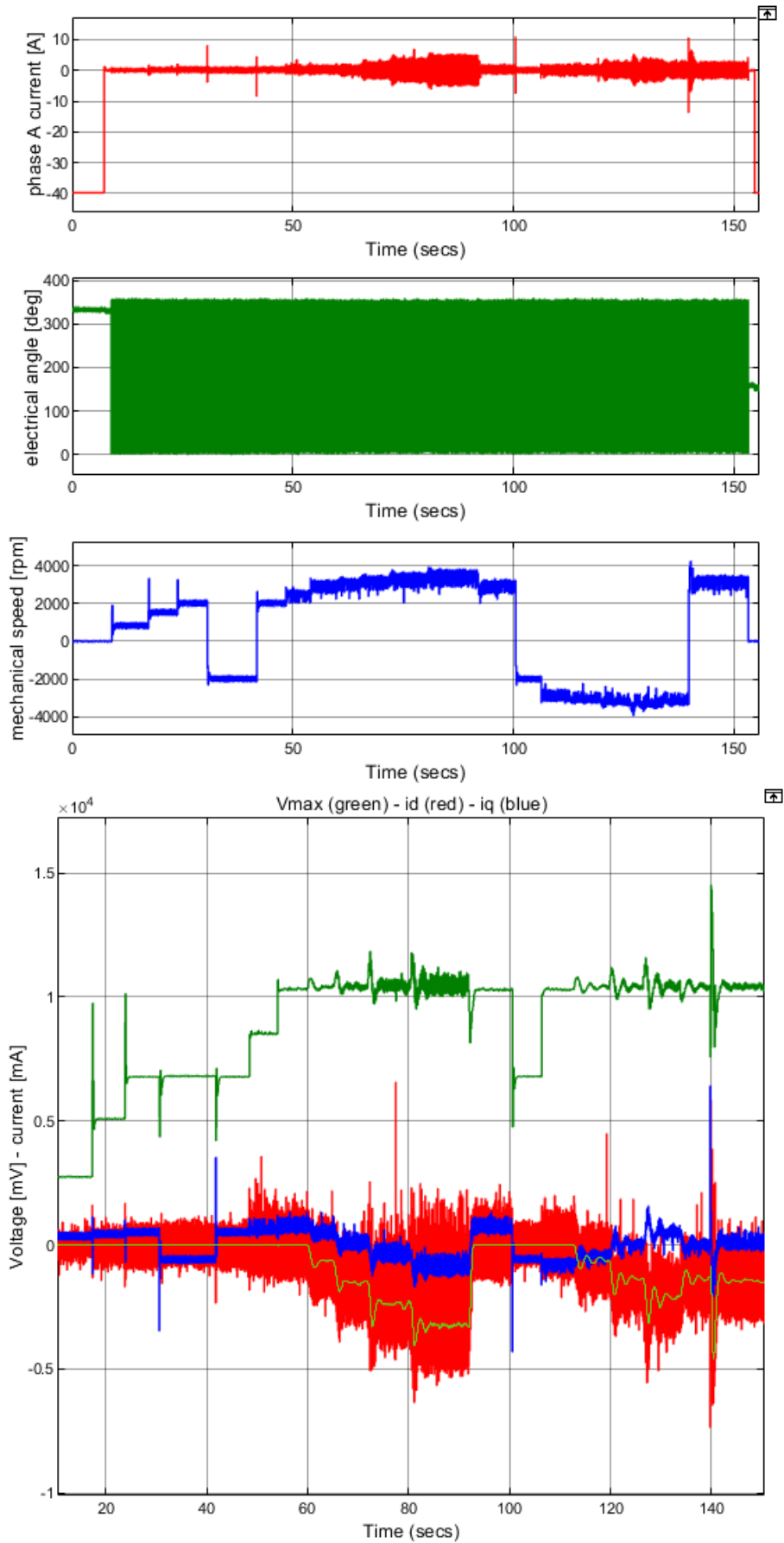


Figure 4. 59: SMO test, FWC negative change

4.3.4. Hall sensor

Finally, the control system has been validated using the linear Hall effect sensors. The motor results adequately controlled with improved response time due the faster sensor execution, whose estimation is correct. Despite this, more noise seems to be introduced in this case.



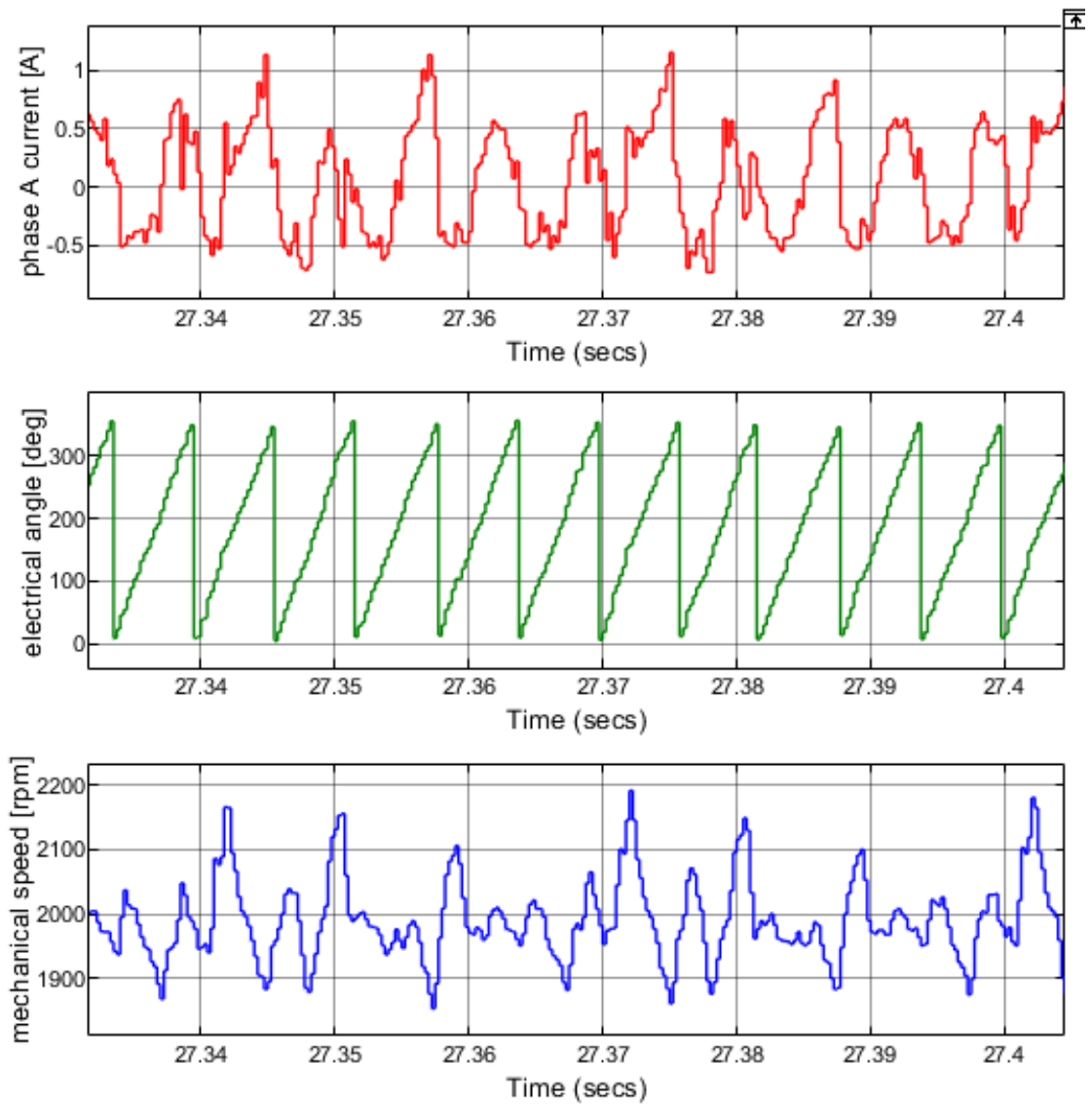


Figure 4. 60: Hall sensor test

The FWC operations are presented below.

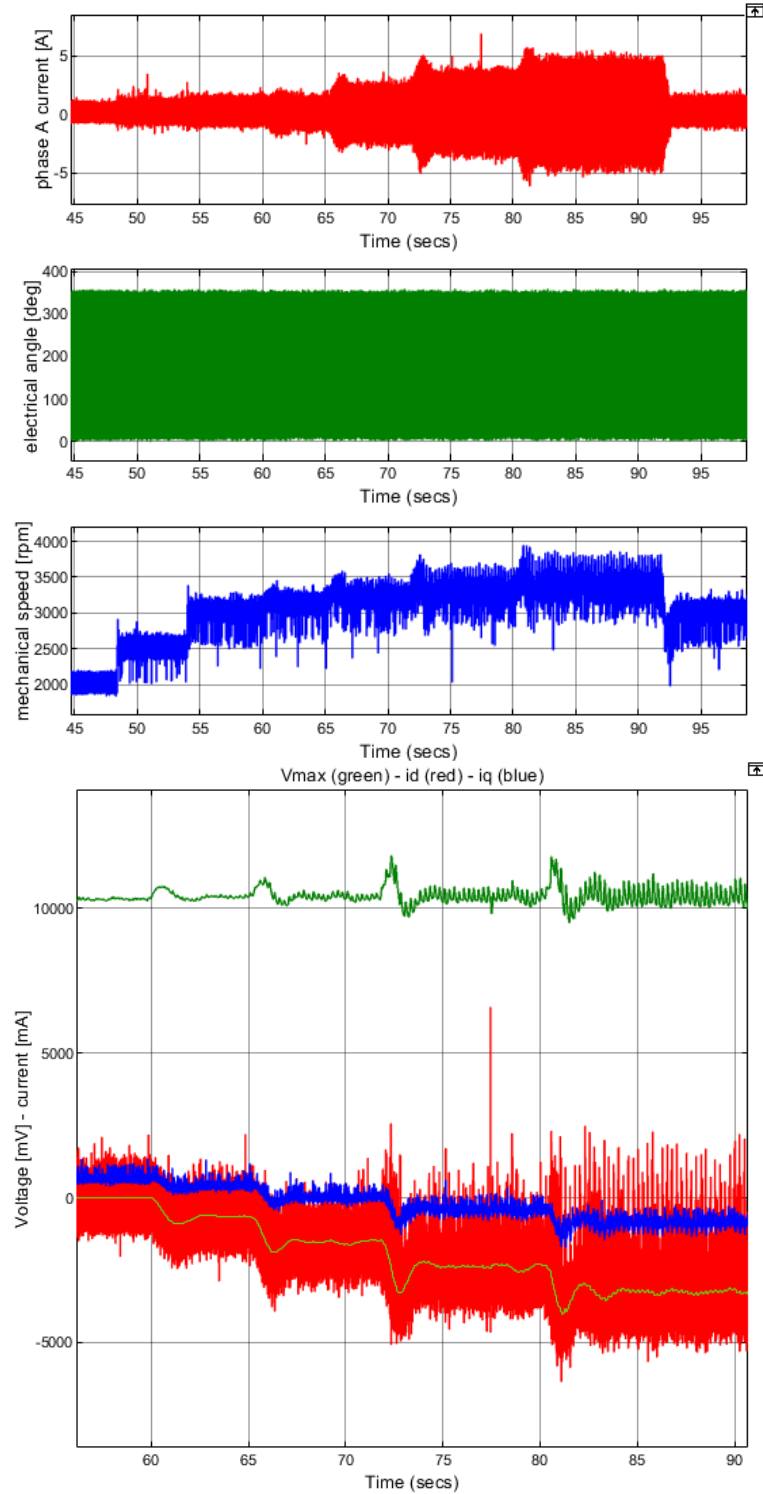


Figure 4. 61: Hall sensor test, FWC positive change

From the following figure it is possible to notice the dynamics introduced by a strong filtering action inserted in the input of the FWC: the response time is bigger and there are small oscillations, although the control stability is ensured.

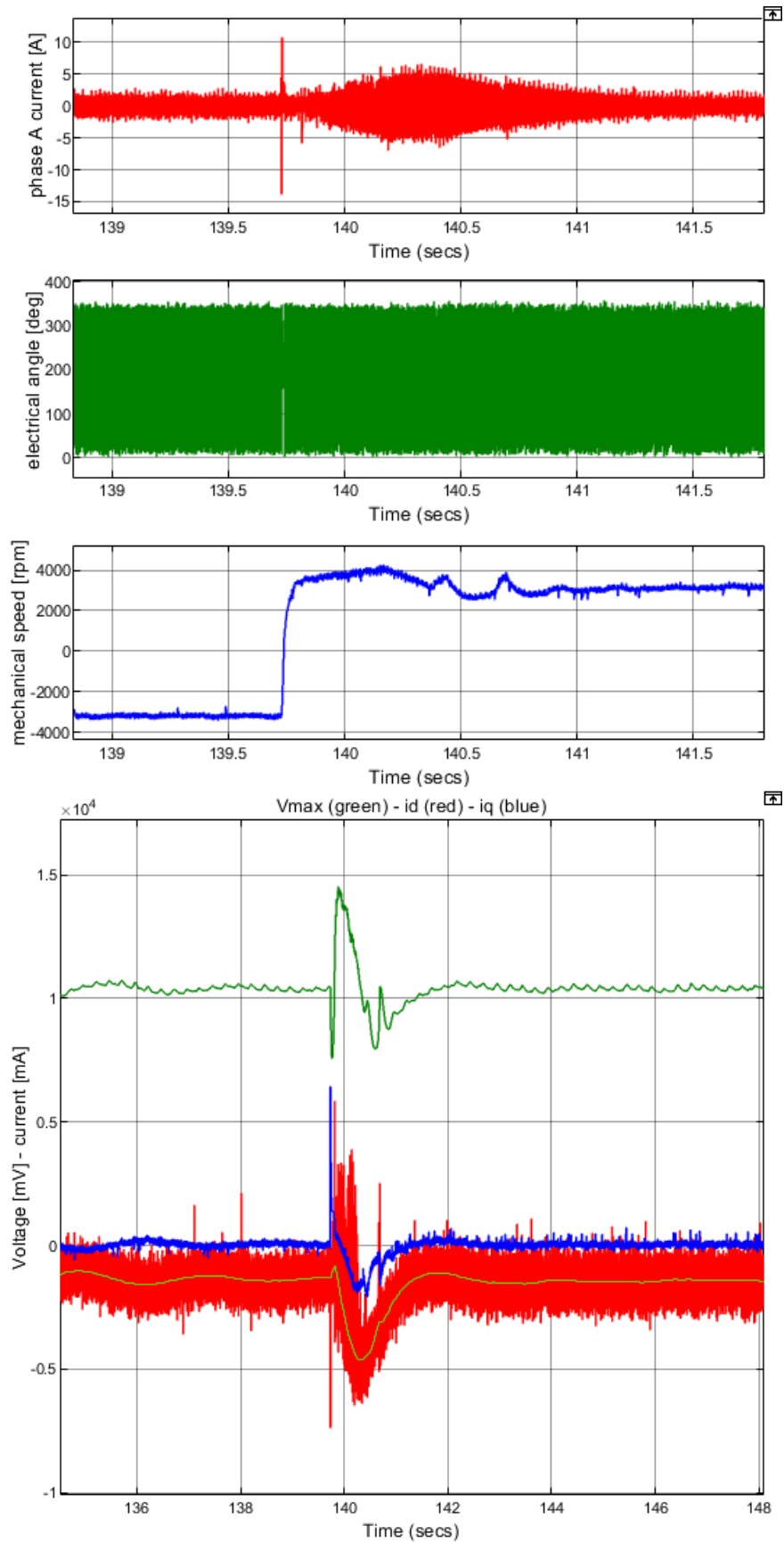


Figure 4. 62: SMO test, FWC negative to positive change

Conclusion

The intent of the thesis was the development of a motor control system and ECU programming. It is inserted in a long-term project at Politecnico di Torino whose aim is to design a regenerative shock absorber for automotive suspension. The main contribution of the thesis work has been the introduction of additional features to the already implemented standard FOC, in order to adequately drive the SPM motor integrated in the system. The key objectives are the flux-weakening controller, the proper regenerative phase management and the substitution of the previous hardware components with a new Texas Instruments development kit. The experimental method utilized during the study has been the V-shaped development flow: through an interactive way, the functionality analysis, the design, the simulation and the prototype testing phases have followed each other.

The chapter 2 presents a preliminary review of the current control method theory for brushless synchronous motor, highlighting the application to the drive of interest i.e., the SPM motor. In parallel, with the illustration of the main features also the design choices have been depicted. Firstly, the field-oriented control of 3-phase PMSM has been analysed, showing the differences coming from the operations in the constant torque or in the flux-weakening region. Additionally, it has been chosen as FWC an outer voltage control loop, composed by a PI regulator. Successively, the advantages of the space vector modulation technique have been introduced. This is the strategy selected to produce the pulse width modulated signals: it permits to obtain a better rated voltage output, extending the inverter linearity region. Then, three different rotor flux position estimation methods have been studied: the sliding mode observer and flux observer, for sensorless control, and the linear Hall effect sensors for sensed control. Theoretically, the latter solution yields better reliability, especially in the low-speed range and brings less stator current distortion.

The third chapter illustrates the design and simulation phases performed through the use of the Motor control blockset, in the MATLAB/Simulink environment. First of all, an accurate requirement and functionality analysis has been performed, based on the target motor parameters. Thus, the limitations and the main operating points have been defined. Successively, the steps taken to design the motor control algorithm have been presented, together with the calibration of all the components. During the simulation phase, only the sensorless controller has been developed. At the end, an accurate numerical validation has

been made in order to verify, through simulation, with a proper plant model, the functionality of the overall designed control structure and of every single module.

The last chapter, which regards the experimental campaign, presents the work done with the real components and prototypes. Firstly, the study has evolved into the settings and validation of the power stage components. Two different 3-phase inverters have been deeply described i.e., the TI DRV8353RS and DRV8323RS: they have been compared to select the most suitable one for the application and have been also modified to enhance their efficiency. After several tests and thermal considerations, the DRV8323RS has been chosen, since it has more safety stability, dissipates better the heat and is more compact. Additionally, its shunt resistor values have been lowered and some heat sinks have been mounted on the top of the board to increase the heat dissipation and the current level measurements. Successively, a benchmarking analysis on the possible battery packs solutions to integrate in the suspension power stage has been developed. Based on the desired parameters, a 48 V_{dc} , LiFePO_4 battery pack of the PowerBrick+ manufacturer has been selected, with a capacity of 25 Ah , which comports a good compromise in terms of weight, dimensions and price. In addition to that, the electronic control unit programming, together with its integration into the power stage has been illustrated. The TI development kit chosen is the LAUNCHXL F28379D thanks to its key features: fast serial connection, CAN-enabled communication and MATLAB/Simulink support for fast code generation. Then, the implementation of the control algorithm and the test bench preparation with the selected components has been done, permitting to validate the overall system solution, extrapolating proper results and monitoring different working points of the motor prototype. During this phase the host and target model have been designed, with a proper recalibration of the control algorithm based on the real plant. In particular, some additional features have been introduced to interface the target hardware with the driver; additionally, also the sensed control system is considered, with the linear Hall effect sensor, together with the observers. Finally, the interrupt service routine design of the microcontroller has been shown, together with a processor-in-the-loop testing to avoid overruns problems and be sure that every task of the algorithm is correctly executed. At the end, the results are presented for the three different angle estimator solutions: they show the correct functionality and robustness of the control system also with the real plant.

In conclusion, the thesis goals have been completely achieved. The result is the ECU provided with a working motor control algorithm, in an innovative TI development kit

interfaced with a stable 3-phase inverter: all the aforementioned structure is ready for the integration in the regenerative shock absorber automotive suspension. As regards as the control system response, it shows stability in all the required operating points of the motor. Thus, the thesis contributed to adding the FWC strategy and the proper regenerative phase management. In fact, the drive system is able to follow high alternate step change in the reference speed, which are proper of a motor integrated in a suspension, by adequately setting the torque response and weakening the flux machine if needed. Furthermore, during the transients, the resulting rise and settling times are really low, presenting a good control dynamic, and the oscillations are small, leading to an optimal control structure. These results are achieved with all the three estimator solutions, although, there are small operating differences. The SMO and the Hall sensors generate a faster response, thus their FWC bandwidths have been slightly lowered with respect to the flux observer one. Additionally, the Hall sensor results depict more noise during high speed operations, for this reason the FWC input voltage has been strongly filtered, generating more oscillations and a slower response with respect to the sensorless control solution, but still maintaining the stability.

At the end, the developed ECU is a flexible and working solution since with a rapid and fast recalibration could be applied to different PMSMs. In future works, the development of the project will include the comparison of the thesis FWC strategy with another method which aims at utilizing a static controller, through a MTPA and FWC current reference generator based on the flux maps of the motor. Successively, the control system and components will be finally validated with the integration in the regenerative shock absorber test bench.

A Numerical models

A.1. Clarke and Park transforms

The 3-phase voltages, currents and fluxes of the AC-motors can be valued in terms of complex space vectors. Considering the a, b and c-axes instantaneous currents in the stator phases (i_a , i_b and i_c), then the complex stator current vector is defined by:

$$\bar{i} = i_a + \alpha i_b + \alpha^2 i_c \quad (\text{A.1})$$

where $\alpha = e^{j\frac{2}{3}\pi}$ and $\alpha^2 = e^{j\frac{4}{3}\pi}$ represent the spatial operators [15]. The figure below shows the current space vector, in the (a,b,c) three phase system.

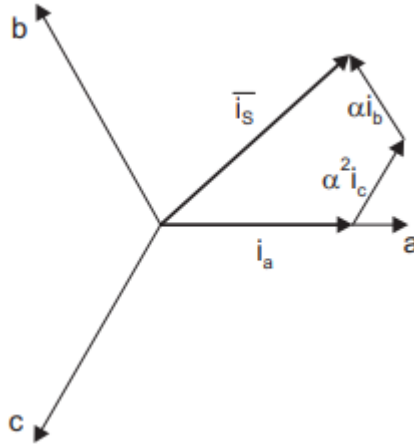


Figure A. 1: Stator current space vector [15]

The space vector can be reported in another reference frame with only two orthogonal axis named (α, β), with axis 'a' and ' α ' having the same direction.

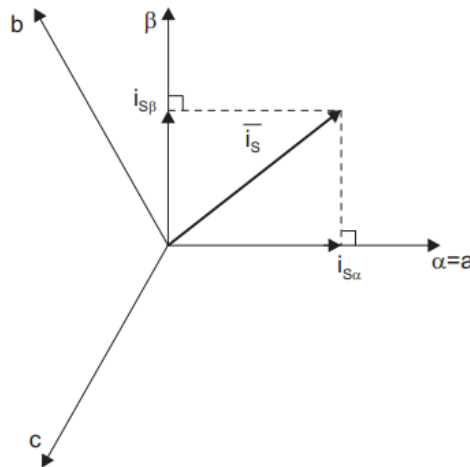


Figure A. 2: Stator current space vector in the stationary frame [15]

The Clarke transform computes the transformation of balanced 3-phase components in the (a,b,c) reference frame and outputs the balanced 2-phase orthogonal components in the stationary (α,β) reference frame through the following equation:

$$\begin{bmatrix} i_\alpha \\ i_\beta \\ i_0 \end{bmatrix} = \left(\frac{2}{3}\right) \times \begin{bmatrix} 1 & -\frac{1}{2} & -\frac{1}{2} \\ 0 & \frac{\sqrt{3}}{2} & -\frac{\sqrt{3}}{2} \\ \frac{1}{2} & \frac{1}{2} & \frac{1}{2} \end{bmatrix} \begin{bmatrix} i_a \\ i_b \\ i_c \end{bmatrix} \quad (\text{A.2})$$

The term i_0 is the zero component in the stationary (α,β) reference frame, which for balanced systems is always null since $i_a + i_b + i_c = 0$.

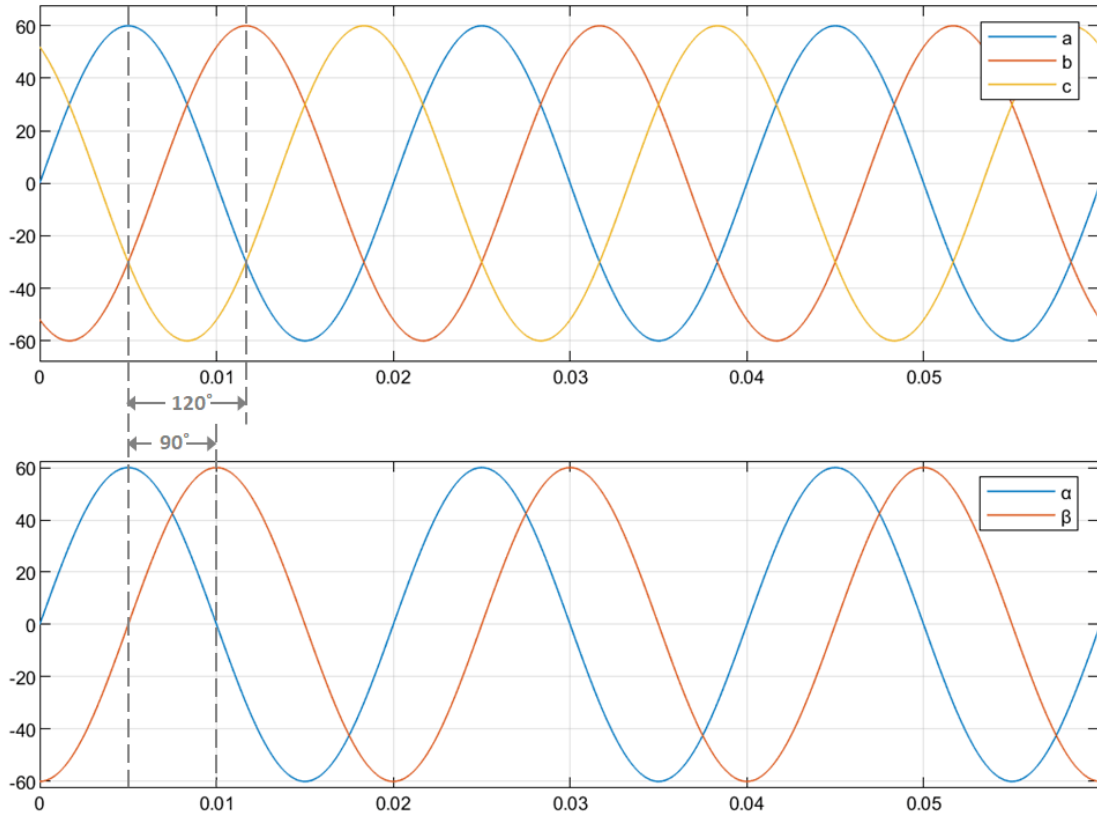


Figure A. 3: Time-response of the individual (a,b,c) and (α,β) components

The Park transform, instead, modifies a 2-phase orthogonal system (α,β) in the (d,q) rotating reference frame. The figure below shows the relationship from the two reference frames, considering the d-axis aligned with the rotor flux.

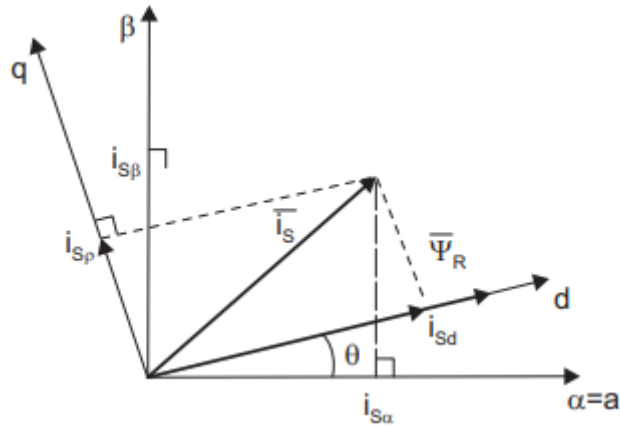


Figure A. 4: Stator current space vector in the (α, β) and (d, q) frames [15]

The term θ is the angle between the α and d -axis, it indicates the angular position of the rotating (d, q) reference frame with respect to the α -axis. The angle can be calculated also as $\theta = \omega t$, where ω is the rotational speed of the (d, q) system and t is the time, in seconds, from the initial alignment. The following equation describe how the Park transform is implemented:

$$\begin{bmatrix} i_d \\ i_q \end{bmatrix} = \begin{bmatrix} \cos \theta & \sin \theta \\ -\sin \theta & \cos \theta \end{bmatrix} \begin{bmatrix} i_\alpha \\ i_\beta \end{bmatrix} \quad (\text{A.3})$$

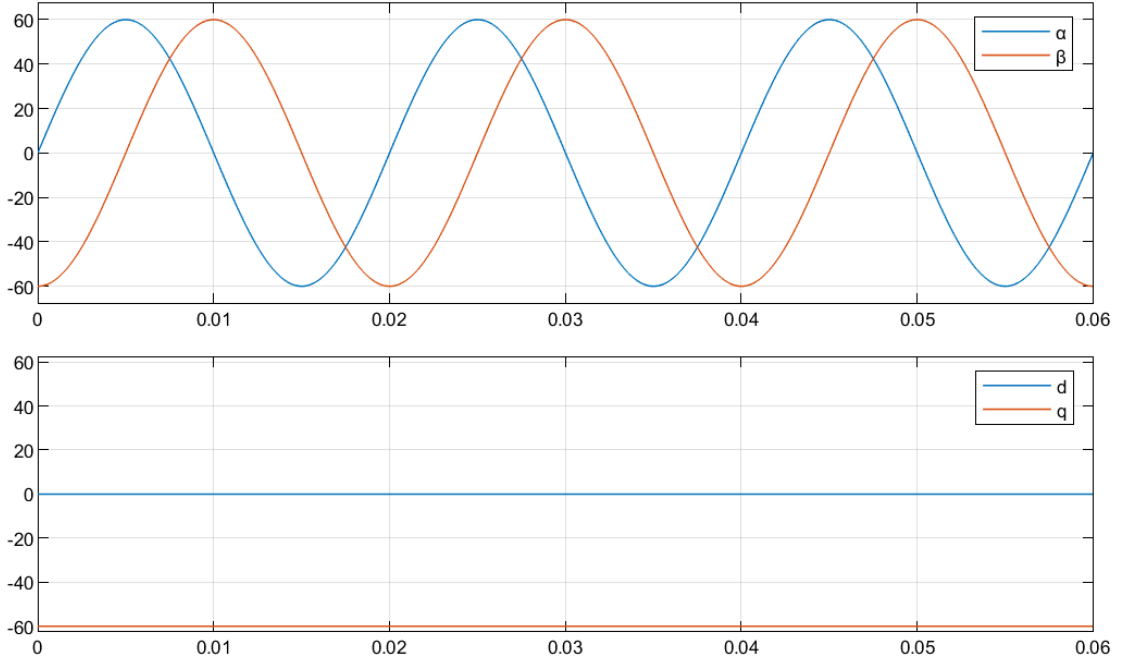


Figure A. 5: Time-response of the individual (d, q) and (α, β) components

Implementing the Clarke and Park transforms in a consecutive manner simplifies the computation since it converts AC waveforms into DC signals.

A.2. Dynamic modelling of AC synchronous machines

In the following section it is presented the dynamic modelling of the brushless PMSM, in particular of the SPM motor. Replacing the common rotor field windings and pole structure with PMs puts the motor into the category of brushless motors. The use of magnets enables an efficient use of the radial space and replaces the rotor windings, lowering the rotor copper losses. Additionally, advanced magnet materials leads to a considerable reduction in motor dimensions, maintaining a high power density [15]. On contrary, the stator windings are sets of insulated copper coils placed in slots. A 3-phase stator fed by balanced 3-phase currents generates a magnetic field and MMF rotating at the synchronous speed ω [16]. Furthermore, in the synchronous machines the rotor speed is rigidly related to the AC frequency imposed by the inverter. The following figure shows the SPM motor construction with a single pole pair on the motor. For the axes convention, the a-phase and PM fluxes are aligned when the motor angle is zero; in addition to that, the d-axis is the direction of PM magnetization.

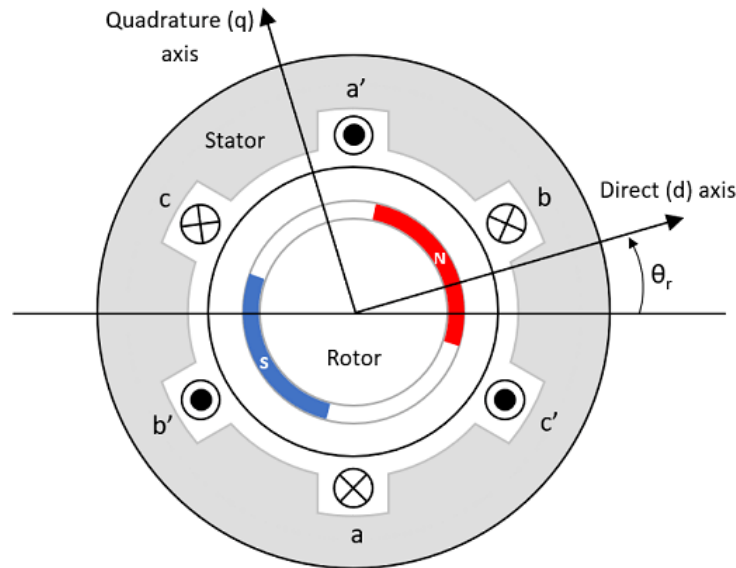


Figure A. 6: SPM motor construction

As regard as the machine model, in the phase coordinates (a,b,c) the voltage equations are:

$$\begin{cases} v_a = R_s \cdot i_a + \frac{d\lambda_a}{dt} \\ v_b = R_s \cdot i_b + \frac{d\lambda_b}{dt} \\ v_c = R_s \cdot i_c + \frac{d\lambda_c}{dt} \end{cases} \quad (\text{A.4})$$

Thus, the voltage is given by two contributions that are the voltage drop on the stator resistance, due to Joule losses, and the flux linkage variation i.e., induced electro-motive force [16]. Applying the Clarke and Park transforms it is possible to obtain the voltage d and q components:

$$\begin{cases} v_d = R_s \cdot i_d + \frac{d\lambda_d}{dt} - \omega \cdot \lambda_q \\ v_q = R_s \cdot i_q + \frac{d\lambda_q}{dt} - \omega \cdot \lambda_d \end{cases} \quad (\text{A.5})$$

where the last motional term depicts the speed dependence. The magnetic model is written in phase coordinates as:

$$\begin{bmatrix} \lambda_a \\ \lambda_b \\ \lambda_c \end{bmatrix} = L_{ls} \cdot \begin{bmatrix} i_a \\ i_b \\ i_c \end{bmatrix} + [M(2\theta)] \begin{bmatrix} i_a \\ i_b \\ i_c \end{bmatrix} + \lambda_m \cdot \begin{bmatrix} \cos(\theta) \\ \cos\left(\theta - \frac{2\pi}{3}\right) \\ \cos\left(\theta + \frac{2\pi}{3}\right) \end{bmatrix} \quad (\text{A.6})$$

where the first term is the leakage flux linkage, the second is the magnetizing flux linkage and the third is the magnets flux contribution. The magnetic model in the (d,q) reference frame is:

$$\begin{bmatrix} \lambda_d \\ \lambda_q \end{bmatrix} = \begin{bmatrix} L_s & 0 \\ 0 & L_s \end{bmatrix} \cdot \begin{bmatrix} i_d \\ i_q \end{bmatrix} + \begin{bmatrix} \lambda_m \\ 0 \end{bmatrix} \quad (\text{A.7})$$

Finally, combining the equations A.5 and A.7, the 3-phase sinusoidal model is composed by the following relationships, together with the torque equation:

$$\begin{cases} \frac{d}{dt} i_d = \frac{1}{L_s} v_d - \frac{R_s}{L_s} i_d + \omega \cdot i_q \\ \frac{d}{dt} i_q = \frac{1}{L_s} v_q - \frac{R_s}{L_s} i_q - \omega \cdot i_d - \frac{\lambda_m}{L_s} \end{cases} \quad (\text{A.8})$$

$$T = \frac{3}{2} \cdot p \cdot (\lambda_d \cdot i_q - \lambda_q \cdot i_d) \quad (\text{A.9})$$

Bibliography

- [1] R. Galluzzi , S. Circosta, N. Amati and A. Tonoli, “Rotary regenerative shock absorbers for automotive suspensions,” 2021.
- [2] R. Galluzzi, X. Yijun, N. Amati e A. Tonoli, «Optimized design and characterization of motor-pump unit for energy-regenerative shock absorbers,» 2018.
- [3] U. Kiencke e L. Nielsen, *Automotive control systems for engine, driveline and vehicle.*
- [4] L. Zuo e P. Zhang, «Energy harvesting, ride comfort, and road handling of regenerative vehicle suspensions,» 2013.
- [5] R. Galluzzi, A. Tonoli, N. Amati e G. Curcuruto, «Regenerative shock absorbers and the role of the motion rectifier,» 2016.
- [6] D. Karnopp, «Permanent magnet linear motors used as variable mechanical dampers for vehicle suspensions,» 1989.
- [7] B. Gysen, T. Van der sande, J. Paulides e E. Lomonova, «Efficiency of a regenerative direct-drive electromagnetic active suspension,» 2011.
- [8] N. Amati, A. Festini e A. Tonoli, «Design of electromagnetic shock absorbers for automotive suspensions,» 2011.
- [9] M. Willems, «Wheel suspension for a motor vehicle». 2013.
- [10] B. Turkus, «Autoblog,» 2016.
- [11] A. A.G., «Predictive active suspension in the A8 flaship model,» 2019.
- [12] A. Tonoli , A. Amati, J. Girardello Detoni, R. Galluzzi e E. Gasparin, «Modelling and validation of electromechanical shock absorbers».
- [13] T. Miller, *Brushless Permanent-Magnet and Reluctance Motor Drives*, 1989.
- [14] Zhang Y., H. Chen, K. Guo, X. Zhang e L. S. Eben, «Electro-hydraulic damper for energy harvesting suspension: modeling, prototyping and experimental validation,» 2017.
- [15] M. Bhardwaj, «Sensored field oriented control of 3-phase permanent magnet synchronous motors,» *Texas Instruments*, 2013.
- [16] S. Seung-Ki, *Control of electric machine drive systems*, 2011.
- [17] W. L. Soong e T. J. E. Miller, «Theoretical limitations to the field-weakening performance of the five classes of brushless synchronous AC motor drive».
- [18] M. Ulusoy, «Space vector modulation for motor control,».
- [19] D. O. Neacsu, «Space vector modulation-An introduction,» 2001.

- [20] J. G. Kassakian, M. F. Schlecht e G. C. Verghese, Principles of power electronics, 2010.
- [21] Y. Kung, N. V. Quynh, C. Huang e L. Huang, «Design and simulation of adaptive speed control for SMO-based sensorless PMSM drive,» 2012.
- [22] Y. Zhang e V. Utkin, «Sliding mode observers for electric machines-an overview,» 2002.
- [23] T. Bernardes, V. F. Montagner, H. A. Grundling e H. Pinheiro, «Discrete- time sliding mode observer for sensorless vector control of permanent magneti synchronous machine,» 2014.
- [24] Z. Guo e S. K. Panda, «Design of a sliding mode observer for sensorless control of SPMSM operating at medium and high speeds,» 2015.
- [25] O. Sandre-Hernandez, J. J. Rangel-Magdalenos e R. Morales-Caporal, «Simulink-HDL cosimulation of direct torque control of a PM synchronous machine based FPGA,» 2014.
- [26] Inoue Y., S. Morimoto e M. Sanada, «Control method suitable for direct torque control based motor drive system satisfying voltage and current limitations,» 2010.
- [27] Y. J. Sung e N. Kwanghee, «PMSM control based on edge-field hall sensor signals through ANF-PLL processing,» 2011.
- [28] Allegro, «Low noise, linear Hall effect sensor ICs with analog output».
- [29] Matlab, «Flux-weakening control,».
- [30] MATLAB, «Field oriented control,».
- [31] Texas Instruments, «DRV8353Rx-EVM User's Guide,» 2018.
- [32] Texas Instruments, «Utilizing the DRV835x split supply power topology for optimal system design».
- [33] Texas Instruments, «DRV835x 100-V Three-phase smart gate driver,» 2019.
- [34] Texas Instruments, «Boostxl-DRV8323RS EVM User's guide,» 2018.
- [35] Texas Instruments, «DRV832x 6 to 60-V Three-phase smart gate driver,» 2018.
- [36] PowerBrick+, «48V battery pack - Lithium iron-phosphate - 25Ah».
- [37] Texas Instruments, «Launchxl-F28379D Overview,» 2019.

Acknowledgments

The thesis work has been developed at the Laboratorio Interdisciplinare di Meccatronica (Politecnico di Torino).

First of all I would like to thank Prof. Amati, Prof. Galluzzi and Dr. Circosta for the opportunity they gave to me to contribute to their project. During the entire work they accurately followed me on my growth path, both as a student and as a person, with their precious advice. They always collaborated with me, accompanying me along the research; they introduced me to a new study approach and lots of new technologies. I really appreciated the organization and also the curiosity with which they pushed me to face new challenges.

Finally, a special thanks to my family and all my friends for supporting me along the way.